

AN INVESTIGATION OF THE SELF-GENERATED
MAGNETIC FIELDS ASSOCIATED WITH A LASER-
PRODUCED PLASMA

Leslie Lawrence McKee

Library
Naval Postgraduate School
Monterey, California 93940

NAVAL POSTGRADUATE SCHOOL

Monterey, California



THESIS

AN INVESTIGATION OF THE SELF-GENERATED
MAGNETIC FIELDS ASSOCIATED WITH A LASER-
PRODUCED PLASMA

by

Leslie Lawrence McKee, III

Thesis Advisor

F. Schwirzke

December 1972

T252093

Approved for public release; distribution unlimited.

An Investigation of the Self-Generated Magnetic Fields
Associated with a Laser-Produced Plasma

by

Leslie Lawrence McKee, III
Captain, United States Air Force
B.S., Colorado State University, 1969

Submitted in partial fulfillment of the
requirements for the degree of

DOCTOR OF PHILOSOPHY

from the
NAVAL POSTGRADUATE SCHOOL
December 1972

ABSTRACT

A plasma was produced by irradiating a 5 mil thick Mylar ($C_{10}H_8O_4$) foil with a 300 MW, 25 nsec Nd laser pulse. Magnetic fields were observed to spontaneously arise when the laser-produced plasma was formed.

The dependence of the self-generated magnetic fields on position, time, incident laser power, and ambient background pressure was investigated. The strength of the magnetic field, as well as its spatial and temporal dependences, was found to depend quite strongly on the background pressure of nitrogen. Most significantly, the strength of the field increased by a factor of six when the pressure of the nitrogen background was increased from 1 mTorr to 200 mTorr.

The results are analyzed by use of a theory in which the presence of a background gas influences the generating mechanism of the fields.

TABLE OF CONTENTS

I.	INTRODUCTION-----	13
II.	THEORY-----	16
A.	LASER-PRODUCED PLASMAS-----	16
B.	INTERACTIONS BETWEEN COUNTERSTREAMING PLASMAS-----	21
C.	SELF-GENERATED MAGNETIC FIELDS-----	22
III.	PREVIOUS EXPERIMENTAL WORK-----	30
A.	SELF-GENERATED MAGNETIC FIELDS-----	30
B.	INTERACTIONS BETWEEN COUNTERSTREAMING PLASMAS-----	30
IV.	STATEMENT OF THESIS PROBLEM-----	33
V.	EXPERIMENTAL ARRANGEMENT-----	35
A.	LASER-----	35
B.	LASER MONITORING TECHNIQUES-----	35
C.	VACUUM CHAMBER-----	36
D.	MAGNETIC PROBES-----	38
	1. Probe Construction and Calibration-----	38
	2. Probe Response-----	38
	3. Probe Signal Integration-----	39
	4. Probe Sensitivity-----	40
	5. Probe Reliability-----	40
	6. Probe Perturbations-----	41
	7. Probe Use-----	42

VI.	EXPERIMENTAL RESULTS-----	43
A.	FIELD ORIENTATION-----	43
B.	CHARACTERISTICS OF MAGNETIC PROBE SIGNALS---	43
C.	LASER POWER DEPENDENCE-----	44
D.	PRESSURE DEPENDENCE OF FIELDS-----	46
E.	SYMMETRY OF THE MAGNETIC FIELDS-----	47
F.	SPATIAL DEPENDENCE OF THE MAGNETIC FIELDS---	50
	1. Pressure Variation-----	50
	2. Two-Dimensional Mapping of the Fields---	52
	3. One-Dimensional Mapping of the Fields---	54
G.	TIME DEPENDENCE OF THE MAGNETIC FIELDS-----	56
	1. Time Decay of the Magnetic Fields-----	56
	2. Two-Dimensional Mapping-----	57
	3. One-Dimensional Mapping of the Magnetic Field-----	61
H.	SUMMARY OF EXPERIMENTAL RESULTS-----	62
VII.	CALCULATED EXPERIMENTAL PARAMETERS-----	65
A.	LASER PLASMA PARAMETERS-----	65
B.	PHOTOIONIZATION OF THE BACKGROUND-----	70
C.	CHARACTERISTICS OF THE SELF-GENERATED MAGNETIC FIELDS-----	75
	1. Current Density-----	75
	2. Magnetic Field Energy-----	76
	3. $\vec{J} \times \vec{B}$ Force Density-----	78
	4. Magnetic Field Diffusion Time-----	81
	5. Magnetic Reynolds Number-----	82

VIII.	THEORETICAL MODEL FOR THE PRESSURE DEPENDENCE	
	OF THE FIELDS-----	83
IX.	ANALYSIS OF EXPERIMENTAL RESULTS-----	86
A.	GENERAL-----	86
B.	ENHANCEMENT OF THE MAGNETIC FIELD WITH AMBIENT PRESSURE-----	86
C.	SPATIAL AND TEMPORAL BEHAVIOR OF THE FIELDS-----	90
	1. Low Ambient Pressures-----	90
	2. High Ambient Pressures-----	93
	3. Intermediate Ambient Pressures-----	98
X.	CONCLUSION-----	101
	APPENDIX A-----	103
	APPENDIX B-----	105
	FIGURES-----	107
	BIBLIOGRAPHY-----	171
	INITIAL DISTRIBUTION LIST-----	173
	FORM DD 1473-----	174

LIST OF TABLES

I. Results of Symmetry Mapping of Azimuthal Magnetic Field-----	49
--	----

LIST OF FIGURES

1.	Cylindrical polar coordinate system used-----	107
2.	Block diagram of experimental layout-----	108
3.	Top view of vacuum chamber-----	109
4.	Magnetic probe signal representing the azimuthal magnetic field detected at $z=r=4$ mm, $\theta=0^\circ$, for a nitrogen background gas pressure of 250 mTorr----	110
5.	Maximum azimuthal magnetic field at $z=4$ mm, $r=3$ mm, $\theta=0^\circ$, as a function of laser power incident on a .005 in. Mylar foil in a background gas pressure of 25 mTorr of nitrogen-----	111
6.	Maximum azimuthal magnetic field at $z=4$ mm, $r=3$ mm, $\theta=0^\circ$, as a function of nitrogen background pressure for an incident laser power of 300 MW-----	112
7.	Maximum azimuthal magnetic field at $z=4$ mm, $r=3$ mm, $\theta=0^\circ$, as a function of nitrogen background pressure for a given laser power incident on a .005 in. Mylar foil-----	113
8.	Nitrogen background gas pressure at which the azimuthal magnetic field at a fixed axial position attains its largest value as a function of the axial distance of that position along $r=3$ mm, $\theta=0^\circ$ -----	114
9.	Scale length for the exponential decrease of the maximum azimuthal magnetic field with increasing axial distance along $r=3$ mm, $\theta=0^\circ$, as a function of background pressure of nitrogen gas-----	115
10.	Magnetic field mapping grid in the $\theta=0^\circ$ plane-----	116
11.	Maximum B_θ for various pressures of nitrogen background gas-----	117
12.	Maximum azimuthal magnetic field as a function of axial distance along $r=4$ mm, $\theta=0^\circ$, for various pressures of nitrogen background gas-----	118
13.	Maximum azimuthal magnetic field along $r=4$ mm, $\theta=0^\circ$, as a function of time, for various pressures of nitrogen background gas-----	119

14. Maximum azimuthal magnetic field along $r=4$ mm, $\theta=0^\circ$, as a function of time, for 250 mTorr of nitrogen background gas-----	120
15. B_θ in Gauss at 0 nsec for various pressures of nitrogen background gas-----	121
16. B_θ in Gauss at 20 nsec for various pressures of nitrogen background gas-----	122
17. B_θ in Gauss at 40 nsec for various pressures of nitrogen background gas-----	123
18. B_θ in Gauss at 60 nsec for various pressures of nitrogen background gas-----	124
19. B_θ in Gauss at 80 nsec for various pressures of nitrogen background gas-----	125
20. B_θ in Gauss at 100 nsec for various pressures of nitrogen background gas-----	126
21. B_θ in Gauss at 120 nsec for various pressures of nitrogen background gas-----	127
22. B_θ in Gauss at 140 nsec for various pressures of nitrogen background gas-----	128
23. B_θ in Gauss at 160 nsec for various pressures of nitrogen background gas-----	129
24. B_θ in Gauss at 180 nsec for various pressures of nitrogen background gas-----	130
25. B_θ in Gauss at 200 nsec for various pressures of nitrogen background gas-----	131
26. B_θ in Gauss at 220 nsec for various pressures of nitrogen background gas-----	132
27. B_θ in Gauss at 240 nsec for various pressures of nitrogen background gas-----	133
28. B_θ in Gauss at 260 nsec for various pressures of nitrogen background gas-----	134
29. B_θ in Gauss at 280 nsec for various pressures of nitrogen background gas-----	135
30. B_θ in Gauss at 300 nsec for various pressures of nitrogen background gas-----	136

31.	B_0 in Gauss at 320 nsec for various pressures of nitrogen background gas-----	137
32.	B_0 in Gauss at 340 nsec for various pressures of nitrogen background gas-----	138
33.	B_0 in Gauss at 360 nsec for various pressures of nitrogen background gas-----	139
34.	B_0 in Gauss at 380 nsec for various pressures of nitrogen background gas-----	140
35.	B_0 in Gauss at 400 nsec for various pressures of nitrogen background gas-----	141
36.	B_0 in Gauss at 440 nsec for various pressures of nitrogen background gas-----	142
37.	B_0 in Gauss at 500 nsec for various pressures of nitrogen background gas-----	143
38.	B_0 in Gauss at 600 nsec for various pressures of nitrogen background gas-----	144
39.	B_0 in Gauss at 700 nsec for various pressures of nitrogen background gas-----	145
40.	B_0 in Gauss at 800 nsec for various pressures of nitrogen background gas-----	146
41.	B_0 in Gauss at 900 nsec for various pressures of nitrogen background gas-----	147
42.	B_0 in Gauss at 1000 nsec for various pressures of nitrogen background gas-----	148
43.	B_0 in Gauss at 1100 nsec for various pressures of nitrogen background gas-----	149
44.	B_0 in Gauss at 1200 nsec for various pressures of nitrogen background gas-----	150
45.	B_0 in Gauss at 1300 nsec for various pressures of nitrogen background gas-----	151
46.	B_0 in Gauss at 1400 nsec for various pressures of nitrogen background gas-----	152
47.	B_0 in Gauss at 1500 nsec for various pressures of nitrogen background gas-----	153

48. B_θ in Gauss at 1600 nsec for various pressures of nitrogen background gas-----	154
49. B_θ in Gauss at 1700 nsec for various pressures of nitrogen background gas-----	155
50. Axial variation of B_θ along $r=4$ mm, $\theta=0^\circ$ at (a) 0 nsec, (b) 20 nsec, (c) 40 nsec, (d) 60 nsec, for different pressures of nitrogen background gas-----	156
51. Axial variation of B_θ along $r=4$ mm, $\theta=0^\circ$ at (a) 80 nsec, (b) 100 nsec, (c) 120 nsec, (d) 140 nsec, for different pressures of nitrogen background gas-----	157
52. Axial variation of B_θ along $r=4$ mm, $\theta=0^\circ$ at (a) 160 nsec, (b) 180 nsec, (c) 200 nsec, (d) 220 nsec, for different pressures of nitrogen background gas-----	158
53. Axial variation of B_θ along $r=4$ mm, $\theta=0^\circ$ at (a) 240 nsec, (b) 260 nsec, (c) 280 nsec, (d) 300 nsec, for different pressures of nitrogen background gas-----	159
54. Axial variation of B_θ along $r=4$ mm, $\theta=0^\circ$ at (a) 320 nsec, (b) 340 nsec, (c) 360 nsec, (d) 380 nsec, for different pressures of nitrogen background gas-----	160
55. Axial variation of B_θ along $r=4$ mm, $\theta=0^\circ$ at (a) 400 nsec, (b) 440 nsec, (c) 500 nsec, (d) 600 nsec, for 5 mTorr of nitrogen background gas-----	161
56. Axial variation of B_θ along $r=4$ mm, $\theta=0^\circ$ at (a) 700 nsec, (b) 800 nsec, (c) 900 nsec, (d) 1000 nsec, for 5 mTorr of nitrogen background gas-----	162
57. Axial variation of B_θ along $r=4$ mm, $\theta=0^\circ$ at (a) 1100 nsec, (b) 1200 nsec, (c) 1300 nsec, (d) 1400 nsec, for 5 mTorr of nitrogen background gas-----	163
58. Axial variation of B_θ along $r=4$ mm, $\theta=0^\circ$ at (a) 1500 nsec, (b) 1600 nsec, (c) 1700 nsec, for 5 mTorr of nitrogen background gas-----	164

59. Calculated plasma time history, giving plasma front position, expansion velocity, and temperature as functions of time for a 300 MW Nd laser pulse incident on a .005 in. Mylar foil-----165
60. Percentage of single ionization caused by the photoionization of the ambient gas by the Bremsstrahlung radiation of the laser plasma as a function of distance from the laser plasma-----166
61. Current density at 120 nsec for 250 mTorr of nitrogen background gas-----167
62. Current density at 120 nsec for 5 mTorr of nitrogen background gas-----168
63. Total energy in the self-generated magnetic field versus time for various pressures of nitrogen background gas-----169
64. $\vec{J} \times \vec{B}$ force density at 120 nsec for 250 mTorr of nitrogen background gas-----170

ACKNOWLEDGEMENT

I would like to take this opportunity to acknowledge the valuable help of Mr. Hal Herreman. Without his advice and patient guidance, the experimental work described in this thesis would have been much more difficult to accomplish. I would also like to acknowledge the valuable working relationship that I established with Ron Bird, whose work has been very helpful in interpreting the experimental results described in this thesis. I would also like to thank Professor Schwirzke for his support throughout my thesis work.

My special thanks go to my wife, Shirley, for her patience and understanding when I had to work late at night and on weekends and also for her encouragement during difficult periods in this thesis work.

This research was sponsored by the Air Force Office of Scientific Research, United States Air Force, under AFOSR Grant No. MIPR-0004-69, and by the Office of Naval Research.

I. INTRODUCTION

If the beam of a giant-pulse laser is focused on a solid target, a dense, energetic plasma can be produced. Absorption of the laser radiation by the target results in vaporization of material from its surface. This vaporized material then continues to absorb laser radiation, and a hot, ionized plasma results.

Laser-produced plasmas (hereafter referred to as laser plasmas) have several desirable features, including their ease of production and their initially high temperatures and densities. These properties have made them particularly suited for plasma confinement studies related to controlled fusion research. In relation to that important problem, a complete understanding of laser plasmas is essential, and in recent years interest in them has increased dramatically [Ref. 1].

The influence of magnetic fields on laser plasmas is an important topic in controlled fusion research. The interaction of a plasma with a strong magnetic field is the only way in which a hot, dense plasma can be confined and prevented from expanding under the influence of its internal pressure. Magnetic fields can also have more subtle effects on a plasma such as by influencing electronic heat conduction and the generation of plasma instabilities.

In studying such topics, it has been generally assumed that the only magnetic field present was the externally applied field. Under this assumption, there has been difficulty in some notable cases in satisfactorily explaining the behavior of laser plasmas.

However, it was recently discovered that a magnetic field may spontaneously arise when a laser plasma is produced by the laser-induced breakdown of a gas [Ref. 2] or by the laser irradiation of a solid target [Ref. 3].

From these investigations, it appears that self-generated magnetic fields may arise under very general conditions during the production of a laser plasma. In fact, these fields may be an inherent property of laser plasmas. In that case, these fields must be included in a proper theoretical treatment of laser plasmas.

The previous studies of the self-generated magnetic fields involved little more than their discovery. The purpose of this thesis is to extend both the experimental and the theoretical knowledge of the origin of these fields and their influence on laser plasmas.

This thesis is divided into nine more sections. Section II presents the basic theory for laser plasmas, the interaction between a laser plasma and an ambient plasma, and the self-generated magnetic fields. Section III discusses the previous experimental work done in these areas. In Section IV the thesis problem is stated. Section V contains the details of the experimental arrangement, and

the experimental techniques are discussed. In Section VI the experimental results of this investigation are presented. These results include the nature and orientation of the self-generated magnetic fields, their dependence on the incident laser power, the strong influence of a background gas of nitrogen on the fields, and their spatial and temporal behavior. Estimates of the experimental parameters which could not be measured are given in Section VII. In Section VIII a theoretical model is proposed to explain the strong dependence of the fields on the ambient pressure of the nitrogen background gas. In Section IX the experimental results are analyzed in terms of the theory given in Sections II and VIII. Concluding remarks are contained in Section X.

II. THEORY

A. LASER-PRODUCED PLASMAS

The production and heating of a plasma by means of the interaction of a laser beam with a solid was first treated theoretically by Basov and Krokhin [Ref. 4] in 1963 and later by Dawson [Ref. 5]. The theory was later refined by Haught and Polk [Ref. 6]. The treatment presented here is essentially that of Haught and Polk.

In their treatment, the vaporization and ionization of the solid target by the laser was ignored, since they were interested only in the heating and dynamics of the resulting plasma. Instead, the target was assumed to initially be a cold, fully ionized plasma with the density of the solid. The laser radiation is then absorbed via the inverse Bremsstrahlung process by the plasma electrons. The electrons quickly lose their energy to the ions via collisions,¹ and the plasma is heated.

The heating process produces pressure gradients which cause the plasma to expand. Using a fluid model for the plasma, the expansion process is described (in the absence of any macroscopic electric or magnetic fields) by

1. The electron-ion thermalization time is typically of the order of 10^{-10} sec for a laser plasma [Ref. 1].

$$\rho \frac{\partial \vec{v}}{\partial t} = - \vec{\nabla} P \quad (1)$$

where ρ is the plasma mass density, \vec{v} is the expansion velocity, and P is the plasma pressure. If the ions and electrons are assumed to have a common temperature, then the plasma pressure is given by

$$P = (n_i + n_e) kT \quad (2)$$

where n_i and n_e are the ion and electron particle densities and kT is the plasma temperature.

If energy losses due to plasma radiation processes are neglected, then the plasma temperature is determined by equating the rate at which the plasma absorbs energy to the sum of the rate of change of the thermal energy in the plasma and the rate at which work is done by the plasma in its expansion:

$$W = 3/2 (n_e + n_i) \frac{d(kT)}{dt} - \vec{\nabla} P \cdot \vec{v} \quad (3)$$

where W is the rate at which energy is absorbed per unit volume from the laser beam. $-\vec{\nabla} P \cdot \vec{v}$ is always positive for the free expansion of a laser plasma. After the plasma ceases to absorb further laser radiation, W equals zero in Eqn. 3, and the plasma temperature must decrease as the expansion progresses. The laser plasma continues to expand under adiabatic conditions, and the thermal energy of the plasma is converted into kinetic energy via the pressure gradient force in Eqn. 3. The expansion velocity

of the laser plasma then approaches an asymptotic value as the absorbed laser energy is converted entirely into kinetic expansion energy.

The creation of a laser plasma from a plane target can be treated as a one-dimensional problem if the laser beam diameter is larger than the thickness of the plasma during its early formative stages. In this case, the plasma expands in one dimension away from the surface (at $x=0$).

For such a one-dimensional geometry, the power absorbed by the plasma is given by

$$W' = \Phi \Lambda (1 - e^{-\int_0^X K dx}) \quad (4)$$

where Φ is the power density (power per unit cross sectional area) of the incident laser beam, Λ is the area of the beam, K is the absorption coefficient, and X is the boundary position of the laser plasma. The absorption coefficient describing the inverse Bremsstrahlung absorption process is given by [Ref. 7]

$$K = \frac{8\pi z^2 n_e n_i e^6 \ln \Lambda}{3c v^2 (2\pi m_e kT)^{3/2} (1 - v_p^2/v^2)^{1/2}} \quad (5)$$

where z is the ionic charge, e is the electronic charge, $\ln \Lambda$ is the Coulomb logarithm [Ref. 8], c is the speed of light, v and v_p are the laser and plasma frequencies, and m_e is the mass of the electron. Equation 5 shows that the laser light can penetrate the plasma only if $v > v_p$ and that

strong absorption occurs only if v_p is not much less than v . Since $v_p \propto n_e^{1/2}$ and since the electron density decreases as the laser plasma expands, the plasma soon becomes transparent to the laser radiation, and absorption ceases as the expansion progresses.

Analytical solutions for the one-dimensional motion of the laser plasma boundary and for the plasma temperature can be obtained if some simplifying assumptions are made. The laser is assumed to heat the plasma uniformly so that the ions and electrons have a common, uniform temperature at all times.² Further, the electron and ion densities are assumed to have the time-independent form

$$n = n_0 \left(1 - \frac{x}{X}\right) \quad x \leq X \quad (6)$$

where n_0 is the density at the target's surface, and the velocity of the plasma expansion is assumed to have the time-independent form

$$V = V_0 \frac{x}{X} \quad x \leq X \quad (7)$$

where V_0 is the velocity of the plasma boundary. Equations 1 and 3 are then integrated over the cylindrical volume of the plasma. The results are [Ref. 9].

$$\frac{1}{3} (N_i m_i + N_e m_e) \frac{d^2 X}{dt^2} = \frac{2 (N_i + N_e) kT}{X} \quad (8)$$

where N_i and N_e are the total numbers of ions and electrons,

2. The validity of this and other assumptions made in this section is discussed by Haught and Polk [Ref. 6].

and

$$W' = 3/2 \frac{d}{dt} [(N_i + N_e) kT] + 1/6 \frac{d}{dt} [(N_i m_i + N_e m_e) (\frac{dX}{dt})^2]. \quad (9)$$

After laser shut-off when W' is zero, Eqns. 8 and 9 can be combined to give

$$\frac{2}{X} \frac{dX}{dt} + \frac{1}{T} \frac{dT}{dt} = 0 \quad (10)$$

This equation is solved by

$$TX^2 = \text{const.} \quad (11)$$

which is the relationship between the plasma temperature and volume (volume $\propto X$) for a one-dimensional adiabatic expansion. Hence, Eqn. 11 shows explicitly that the laser plasma expands adiabatically after laser shut-off. Also, Eqn. 11 can be used in Eqn. 8 to give for the acceleration of the plasma front

$$\frac{d^2X}{dt^2} \propto \frac{1}{X^3} \quad (12)$$

which shows that after the laser shut-off, the expansion velocity approaches an asymptotic value (i.e. the acceleration of the laser plasma front approaches zero as it expands). During this adiabatic expansion, the laser plasma's thermal energy is converted into kinetic expansion energy as Eqn. 9 shows.

B. INTERACTIONS BETWEEN COUNTERSTREAMING PLASMAS

Two counterstreaming plasmas can be produced by the laser irradiation of a solid target located in an ambient background of gas. The Bremsstrahlung radiation from the hot laser plasma during its early heating stage is absorbed by the neutral atoms of the background gas, and their photoionization results. The ambient background gas then becomes an ambient background plasma, and the laser plasma streams into it as it expands away from the target.

These two counterstreaming plasmas may interact with each other, with the result that an interaction region forms at the front of the expanding laser plasma. In this front region, the laser plasma transfers momentum to the ambient plasma. A strong coupling between the two plasmas will drastically alter the dynamics of the laser plasma, if the density of the ambient plasma is sufficiently high.

The mechanism of the interaction will be binary collisions between the counterstreaming ions if the ambient background gas pressure is high enough (≥ 200 mTorr) so that the collision mean free path for momentum transfer is smaller than the dimensions of the expanding laser plasma. At lower pressures, there can still be efficient coupling between the two plasmas if collective plasma (collisionless) mechanisms are operative. In collisionless interactions, momentum is exchanged between ions via

"effective collisions," in which ions are scattered by unstable plasma waves which may be generated when counter-streaming ions are present.

Of particular interest to this thesis is the theoretical treatment by Papadopoulos et al. [Ref. 10]. They found that the presence of a small magnetic field permits the ion-ion two-stream instability to grow at lower electron temperatures than would normally be required. Since self-generated magnetic fields are present in the laser plasma, this instability may be important, and may result in a very efficient coupling between the counter-streaming plasmas. If this mechanism is operative, then the interaction front thickness will be given by [Ref. 10]

$$\delta = \frac{1}{6} \frac{V}{\omega_{pi}} \frac{\omega_{pe}}{\omega_{ce}} \propto \frac{V}{B} \quad (13)$$

where v is the velocity of the front of the expanding laser plasma, ω_{pi} and ω_{pe} are the ion and electron plasma frequencies, ω_{ce} is the electron cyclotron frequency, and B is the strength of the magnetic field.

C. SELF-GENERATED MAGNETIC FIELDS

When electric and magnetic fields are present, the equation of motion for the electron component of the plasma is

$$\rho_e \frac{\partial \vec{v}_e}{\partial t} = -\vec{\nabla} P_e - en_e (\vec{E} + \vec{v}_e \times \vec{B}) + \frac{n_e e}{\sigma} \vec{j} \quad (14)$$

where the subscript e refers to the electron component of the quantity involved, \vec{E} is the electric field intensity, \vec{j} is the electron current density, and σ is the scalar electrical conductivity of the plasma. Equation 14 assumes a scalar electron pressure and that the rate of momentum exchange between the ions and the electrons is proportional to their relative velocity.

Since inertial forces can be neglected for the electrons when changes are sufficiently slow,³ the right hand side of Eqn. 14 can be set equal to zero and solved for \vec{E} . The result is

$$\vec{E} = \frac{\vec{j}}{\sigma} - \vec{V}_e \times \vec{B} - \frac{1}{n_e e} \vec{\nabla} P_e . \quad (15)$$

Equation 15 is substituted into Maxwell's equation

$$\frac{\partial \vec{B}}{\partial t} = - \vec{\nabla} \times \vec{E} \quad (16)$$

giving

$$\frac{\partial \vec{B}}{\partial t} = \vec{\nabla} \times (\vec{V}_e \times \vec{B}) - \frac{1}{\sigma} \vec{\nabla} \times \vec{j} + \vec{\nabla} \times \frac{1}{n_e e} \vec{\nabla} P_e . \quad (17)$$

-
3. The inertial term in Eqn. 14 becomes significant only when the changes in plasma parameters are so fast that the electrons cannot respond instantaneously to them. This corresponds to changes whose frequencies are at least of the order of the electron plasma frequency (typically 10^{12} sec⁻¹). However, here the parameters of interest change on a time₉ scale comparable with that of the laser pulse (10^{-9} sec). Hence, inertial effects can be neglected in Eqn. 14.

By using Maxwell's equation for the current density as it applies to a laser plasma, and using vector identities (see Appendix A), Eqn. 17 can be reduced to

$$\frac{\partial \vec{B}}{\partial t} = \vec{V} \times (\vec{V}_e \times \vec{B}) + \frac{1}{\mu_0 \sigma} \nabla^2 \vec{B} + \frac{k}{en_e} \vec{V}_T \times \vec{V}_e \quad (18)$$

The three terms in Eqn. 18 represent, respectively, the convection of the magnetic field, the diffusion of the magnetic field, and the generation of the magnetic field.

The convection term describes the transport of the field due to the flow of the plasma electrons. In the absence of the other two terms, Eqn. 18 becomes

$$\frac{\partial \vec{B}}{\partial t} = \vec{V} \times (\vec{V}_e \times \vec{B}) \quad (19)$$

Equation 19 can be shown to be the condition for the invariance of the magnetic flux through any closed contour, each element of which moves with the local electron fluid velocity \vec{V}_e [Ref. 8]. Further, when the magnetic flux through every contour is strictly constant during the motion, it can be shown that the magnetic lines of force can be regarded as moving entities, each element of which moves with the local velocity \vec{V}_e [Ref. 8]. In other words, Eqn. 19 states that the rate of change of the magnetic field at a position is the result of the flow of the magnetic field by that position at the velocity \vec{V}_e . When Eqn. 19 is true, the field is said to be "frozen" into the plasma.

The diffusion term describes the decay of the magnetic field due to Ohmic dissipation of the currents causing the field. In the absence of the other two terms, the magnetic field would be described by a diffusion equation,

$$\frac{\partial \vec{B}}{\partial t} = \frac{1}{\mu_0 \sigma} \nabla^2 \vec{B} \quad (20)$$

where the diffusion coefficient is $\frac{1}{\mu_0 \sigma}$. The characteristic time for the diffusion of the field can be determined from Eqn. 20 by dimensional analysis, and is

$$\tau_m = \mu_0 \sigma L^2 \quad (21)$$

where L is the characteristic length of the magnetic field. In the absence of Ohmic losses ($\sigma \rightarrow \infty$), the diffusion term vanishes.

Initially there is no magnetic field so that only the last term in Eqn. 18 is nonvanishing. For this reason it is called the source term for the creation of magnetic field. The source term predicts that a self-generated magnetic field will arise whenever the temperature and the density gradients are not in the same direction.

In order to gain some insight into the generation of the magnetic fields, Eqn. 15 is solved for \vec{j} before the magnetic field has become significant:

$$\vec{j} = \sigma \left(\vec{E} + \frac{1}{n_e e} \vec{\nabla} p_e \right). \quad (22)$$

Due to their higher thermal velocity, the electron pressure gradient will act to drive the electrons away from the ions. This charge separation causes electrostatic fields to arise which attract the electrons back to the ions. A balance results, in an equilibrium situation, between the pressure gradient driving the electrons away from the ions and the resulting space-charge fields pulling them back. In this electrostatic situation, the right hand side of Eqn. 22 vanishes, and no currents are driven. If there is a component of the density gradient, $\vec{\nabla}n$, normal to the pressure gradient, $\vec{\nabla}(nkT)$, this balance between the electric field and the pressure gradient is upset by the diffusion of electrons at right angles to the pressure gradient. In this case, the right hand side of Eqn. 22 does not vanish, and currents are driven which generate magnetic fields.

When a laser plasma is created, very large density gradients arise in the $-z$ -direction (see Fig. 1) as it expands away from the target. However, the source term of Eqn. 18 shows that no magnetic fields will be created unless temperature gradients exist in the radial direction. A radial temperature gradient can be produced by the direct action of the laser beam. This is because a physically realistic laser beam is nonuniform in cross section. Instead, the spatial distribution of the beam is Gaussian in cross section so that the power of the beam is greatest along its axis and falls off toward the lateral

extensions of the beam. Then the laser beam produces the strongest heating at the center of the irradiated target area and less heating near the boundary of this area. Hence, a temperature gradient will arise in the $-r$ -direction (see Fig. 1) as a direct consequence of the laser heating of the plasma.

If the laser plasma is axially symmetric, such density and temperature gradients result in a particularly simple field configuration. A laser plasma created by the irradiation of a plane target by a cylindrically symmetric laser beam will have axial symmetry. The axis of symmetry will be the target normal which passes through the center of the laser-irradiated target area (i.e. the z -axis in Fig. 1). Hence, because of symmetry, there can be no azimuthal temperature or density gradients about the symmetry axis. According to the source term of Eqn. 18, the magnetic field will be generated entirely in the azimuthal direction about the z -axis. Then, according to the source term, the radial temperature gradient and the axial density gradient will combine to produce an axisymmetric azimuthal magnetic field in the clockwise direction about the z -axis (see Fig. 1).

The length of time that field production remains significant depends on how long the density and the temperature gradients remain significant. If the laser plasma expands into a high vacuum, the density gradient will steadily decrease. The radial temperature gradient

will also decrease due to heat conduction. Hence, the field production in a laser plasma expanding into a high vacuum soon becomes negligible at a rate determined by the expansion velocity of the laser plasma and its thermal conductivity.

Finally, it should be noted that the strongest field production takes place where the source term of Eqn. 18 is largest. This will not be where either the temperature or the density of the plasma is largest, since $\vec{\nabla}T$ and $\vec{\nabla}n$ vanish at such positions. Instead, it will be near the front of the laser plasma. To illustrate this point, consider a laser plasma with a two-dimensional Gaussian temperature profile of the form

$$T(r, z) = T_0 e^{-r^2/2R^2} e^{-z^2/2X^2} \quad (23)$$

where T_0 is the temperature at the origin, and a Gaussian density profile of the form

$$n(r, z) = n_0(r) e^{-z^2/2X^2} \quad (24)$$

where $n_0(r)$ is the density at the target's surface. Then the source term of Eqn. 18 becomes

$$S = \frac{k}{e} \frac{Zr}{X^2 R^2} T_0 e^{-z^2/2X^2} e^{-r^2/2R^2} \quad (25)$$

The position where the source term given by Eqn. 25 is maximum can be determined by differentiating Eqn. 25 with respect to z and with respect to r and setting the results equal to zero. The result for differentiating by z is

$$1 - \frac{z^2}{x^2} = 0 \quad (26)$$

and for differentiating by r is

$$1 - \frac{r^2}{R^2} = 0 \quad (27)$$

Thus, Eqn. 25 is maximum where $z=X$ and $r=R$. Then for this example, field production occurs at the highest rate at the front and side of the laser plasma.

It must again be pointed out that these considerations strictly apply only to the case of the expansion of a laser plasma into a high vacuum. The effects of an ambient plasma on the field production remain to be investigated.

III. PREVIOUS EXPERIMENTAL WORK

A. SELF-GENERATED MAGNETIC FIELDS

The self-generated magnetic fields produced by irradiating a solid target with a laser were first detected by Stamper et al. [Ref. 3]. A neodymium-doped glass laser with an output of 60 J in 30 nsec was used to irradiate a Lucite ($C_5H_8O_2$) fiber 250 microns in diameter. The fiber target was located in a background gas of nitrogen.

The magnetic fields were detected by means of magnetic probes as pulses which propagated with the same velocity as the expanding laser plasma front. The direction of the fields was primarily azimuthal and in the clockwise direction in Figure 1. With a nitrogen background pressure of 200 mTorr, magnetic fields of up to 1 kG in magnitude were measured, and the magnitude of the spontaneous fields was found to be insensitive to background pressure in the range 50-200 mTorr.

B. INTERACTIONS BETWEEN COUNTERSTREAMING PLASMAS

The interaction between two counterstreaming plasmas produced by the laser irradiation of a solid target located in an ambient background gas has been investigated by Dean [Ref. 11]. His experimental situation was essentially that of Stamper et al. [Ref. 3.] Briefly, he found that:

- (1) A well-defined expanding interaction front existed.
- (2) This front consisted of a shell of increased density.
- (3) The dynamics of the front were strongly dependent on the pressure of the ambient background gas.
- (4) The density gradients in the shell depended on the ambient density.
- (5) The front thickness was of the order of 1-2 mm, which was small compared to estimates of collisional momentum transfer mean free paths.
- (6) The dynamics of the laser plasma are in good agreement with a strong momentum-coupling model.
- (7) A possible mechanism for the collisionless interaction is the ion-ion two-stream instability in the presence of a magnetic field, since the observed front widths were in agreement with Eqn. 13 and since self-generated magnetic fields of the order of 1 kG had been detected in the laser plasma.

Other evidence for collisionless momentum coupling between counterstreaming plasmas was obtained in an experiment in which a coaxial plasma gun accelerated an aluminum plasma into a low-pressure background gas which had been preionized by ultraviolet radiation from the gun [Ref. 12]. No coupling was found unless a weak (≤ 200 G) magnetic field was applied. A field of this magnitude could not directly influence the dynamics of the aluminum

plasma. This work also supports a collisionless momentum coupling which is operative only in the presence of a magnetic field.

IV. STATEMENT OF THESIS PROBLEM

The previous experimental work by Stamper et al. [Ref. 3] involved only a cursory, initial investigation of the general features of the self-generated magnetic fields. A more extensive study is needed before their generation and subsequent behavior can be thoroughly understood.

This thesis reports the results of such an investigation. In particular, the dependence of the magnitude of the fields on the power of the incident laser beam and on the ambient pressure of a background gas is studied. Also a more detailed spatial mapping is undertaken than was done previously in order to obtain a knowledge of the symmetry and of the spatial and temporal behavior of the fields. The experimental results are then analyzed in terms of Eqn. 18.

Of particular interest in this investigation is the influence of the background gas in the generation of the self-generated magnetic fields. Due to the technical difficulties involved and the lack of adequate time, the interaction between the laser plasma and the ambient plasma was not investigated in this work. Instead, this experiment was done under conditions very similar to those of Dean's investigation [Ref. 11], and the results of that work are assumed to be applicable here. Any

consequences of the coupling between the two plasmas which influence the magnetic fields will be analyzed in terms of Dean's results.

V. EXPERIMENTAL ARRANGEMENT

A. LASER

The laser used in this investigation was a Korad K-1500 Q-switched neodymium-doped glass laser system. The system consisted of an oscillator laser which initiated the Q-switched beam and an amplifier laser which increased the energy of the beam. The output beam from the .5 in.-diameter oscillator rod was coupled into the .75 in.-diameter amplifier rod by beam expansion optics. The Q-switching was performed by a Pockels Cell. This laser system is described in more detail in the MS thesis by Davis [Ref. 13].

The output of the laser system contained energies in the range of 3.5 to 12 J. The duration of the laser pulse was nominally 25 nsec, giving laser output powers in the range of 150 to 450 MW.

B. LASER MONITORING TECHNIQUES

The laser beam was diagnosed by the use of a Korad K-D1 photodiode. This photodiode provides a signal proportional to the laser power and also integrates this output to give another signal which is proportional to the laser energy.

In order to diagnose the laser beam, about 1% of the beam was reflected by a beam splitter (glass slide) to a

MgO diffusing block (see Figure 2). The photodiode then detected the radiation scattered by the diffusing block. The power signal was displayed on a Tektronix 7704 oscilloscope which had a maximum sweep rate of 20 nsec per division, and the energy signal was displayed on a Tektronix 564B storage oscilloscope.

The photodiode energy signal was calibrated by using a Westinghouse RN-1 Laser Radiometer. The radiometer was placed to intercept that portion of the laser beam passing through the beam splitter. The radiometer provided an absolute measure of the energy of the laser beam against which the voltage reading on the storage oscilloscope could be calibrated. A further description of the photodiode and radiometer is contained in the MS thesis by Kunihiro [Ref. 14].

The laser output power signal was used to determine the half width duration of the laser pulse. The peak laser output power was then determined by dividing the laser energy by the pulse width.

The energy output of the laser was reproducible only to within $\pm 15\%$ and had to be monitored on every shot. The pulse width was much more reliable (within 1 nsec) and was checked only once every 20 or so shots.

C. VACUUM CHAMBER

The target was located in a vacuum chamber which was specially constructed to facilitate the diagnosis of the

laser plasma by use of probes and by optical means (see Figure 3). The inside volume of the chamber was cylindrical with a diameter of 10 in. and a height of 6 in. All ports shown in Figure 3 are circular.

The laser beam entered the chamber after passing through a 28 cm focal length lens. The beam then struck the target at an angle of 30° to the flat target's normal. Bringing the laser beam in at this angle, rather than normal to the target's surface, does not affect the direction of the laser plasma expansion. A laser plasma always expands in a direction normal to a flat target's surface, regardless of the angle of incidence of the laser beam [Ref. 9]. By bringing in the laser beam at 30° , it was possible to probe the plasma along the z-axis (at axial distances greater than 5 mm) without having the laser beam strike the probes. Hence, a more complete mapping of the self-generated magnetic field could be performed.

The target was a circular foil of Mylar ($C_{10}H_8O_4$) .005 in. thick and about 5 cm in diameter. The laser beam struck the target 1.5 cm above its axis of rotation and burned a 2 mm-diameter hole in the foil during each shot. The foil could be externally rotated to allow as many as 24 shots to be made without having to change the foil.

The chamber was pumped to a vacuum of about 5×10^{-5} Torr of air by an oil diffusion pump. Nitrogen gas could then be admitted to the chamber to provide an ambient

background for the laser plasma. The ambient pressures of nitrogen used were .1 to 1000 mTorr.

Vacuum pressures lower than one mTorr were measured by means of an ionization gauge. Higher pressures had to be monitored on a thermocouple gauge. In order to insure consistency, the thermocouple gauge was always calibrated to the ionization gauge when the transition was made.

D. MAGNETIC PROBES

1. Probe Construction and Calibration

Diagnosis of the self-generated magnetic fields was performed with small glass-enclosed inductive magnetic probes. The probe coil was ~ 1 mm in diameter, and the outside diameter of the glass tubing enclosing the probe was ~ 2 mm.

These probes were calibrated by insertion into carefully wound Helmholtz coils. The details of the construction and calibration of these probes are contained in the MS thesis by McLaughlin [Ref. 15].

2. Probe Response

The response, or induced voltage ϵ , of an inductive magnetic probe is given by

$$\epsilon = nA \frac{dB_{\perp}}{dt} \quad (28)$$

where nA is the effective area of the probe coil, and dB_{\perp}/dt is the time rate of change of the component of the magnetic field normal to the plane of the coil.

In order that magnetic probes be practical in measuring the magnitude of magnetic fields, the probe response must be linear. In other words, nA in Eqn. 28 must be independent of frequency in the range of interest. The probes used were found to have resonant frequencies of about 45 MHz. At lower frequencies, nA was approximately constant. The self-generated magnetic field signals were found to have significant frequency components up to about 10 MHz. Hence, the response of the probes was acceptable for the signals detected.

3. Probe Signal Integration

As Eqn. 28 shows, the response of the magnetic probes is proportional to dB/dt . In order to obtain signals proportional to the magnetic field itself, the output of the probes was integrated by means of a passive RC integrator. The output voltage of the RC integrator is

$$V_{out} = \frac{nA}{RC} B \quad . \quad (29)$$

where RC is the time constant of the integrator. Equation 29 is valid only for frequencies f such that $2\pi fRC \gg 10$ (see Appendix B).

The time constant of the integrator was checked by integrating sinusoidal signals of frequencies comparable to those of the self-generated magnetic fields (1-10 MHz). The time constant is then given by

$$RC = \frac{1}{2\pi f} \frac{V_{in}}{V_{out}} \quad (30)$$

from Eqn. 29b in Appendix B. This procedure also allowed the frequency dependence of RC to be checked. RC, as determined from Eqn. 30, was found to be constant in the range of 1-15 MHz. Thus, the response of the integrator was linear for the frequencies of interest.

4. Probe Sensitivity

For the probe used, the effective area was $nA = 5.88 \times 10^{-6} \text{ m}^2$ and the integrator time constant was $RC = 3.7 \times 10^{-6} \text{ sec}$. Since the magnetic fields were observed for as long as 2 μsec , their lowest fundamental frequency was $f_0 = 5 \times 10^5 \text{ sec}^{-1}$. Then $2\pi f_0 RC = 11.6$, and the time constant was acceptable.

The conversion factor between the magnetic field and the output of the RC integrator becomes (Eqn. 29)

$$B = 6.29 V_{out} \quad (31)$$

where B is in Gauss and V is in millivolts. The magnetic field signals were recorded on a Tektronix 7704 oscilloscope which has a maximum vertical sensitivity of 1 mV/division. Since .2 division (1 mm) can be easily resolved on the oscilloscope trace, magnetic fields as low as 1 Gauss in magnitude could be resolved.

5. Probe Reliability

Several steps were taken to insure that the magnetic probe data were meaningful. The probe cable was

carefully shielded by covering it with metallic braid to reduce electrostatic noise pickup. In order to check the effectiveness of the shielding, the probe signals were monitored when the laser beam was blocked from entering the vacuum chamber so that no magnetic field was produced to verify that a null signal was obtained. Also, the probe coil orientation was rotated by 180° , and the probe signals were checked to make sure that they reversed in polarity. This test verifies that the probe signals represent inductive signals and not electrostatic pickup [Ref. 16]. Further, the integrated signals were carefully checked to insure that they accurately represented the integrated dB/dt signals. This was done by recording the probe signals with and without the RC integrator. The dB/dt signals were integrated by a simple computer program, and the computer results were compared with the RC integrated signals.

6. Probe Perturbations

In order to measure the magnetic field in a plasma with a probe, it is necessary to insert the probe into the plasma. Unfortunately, the presence of the probe will perturb the plasma to some extent and may cause serious distortion of the magnetic field.

The flow of the expanding laser plasma will be strongly affected by the presence of a probe since the plasma must flow around it. Also, since the glass enclosing the probe is an insulator, the current distribution which

produces the field will also be perturbed. The volume over which the probe effectively perturbs the current distribution is generally larger than the volume of the probe. This is because the probe acts to cool the plasma in its vicinity, lowering the electrical conductivity.

In this experiment, the plasma flow was strongest along the z-axis. Consequently probe-induced perturbations become more significant as the probe is moved in a radial direction toward the axis. This fact must be kept in mind when the probe data taken near the axis is considered.

7. Probe Use

The magnetic probe could be brought into the vacuum chamber via either of the two side ports or the front port (see Figure 3). However, usually the probe was brought in via a probe port directly above the target not shown in Figure 3. The probe ports provided vacuum seals around the glass enclosing the probes.

The probe signal was conducted by 50 ohm cable to the oscilloscope input where it was properly terminated. The oscilloscope display of the magnetic probe signals was externally triggered by the power signal output of the photodiode. This allowed the start of the laser pulse to provide a reliable reference time for the magnetic field signals.

VI. EXPERIMENTAL RESULTS

A. FIELD ORIENTATION

The self-generated magnetic fields were found to be mainly in the azimuthal direction with reference to the z-axis and pointed in the clockwise direction in Figure 1.

Both a radial and an axial component of the magnetic field were also detected. However, these were of significantly lower magnitudes in comparison with the azimuthal component. The radial and axial components were believed to be mainly due to the perturbation of the basically azimuthal field pattern caused by the presence of the glass-enclosed magnetic probes. This belief was later confirmed in a test performed by Ronald Bird in which an open magnetic probe (i.e. not glass-enclosed) was used which had much smaller outside dimensions. This probe detected much lower radial and axial magnetic fields than the glass-enclosed probe did, but the magnitude of the azimuthal field was about the same for the two probes.

B. CHARACTERISTICS OF MAGNETIC PROBE SIGNALS

A typical magnetic probe signal is shown in Figure 4. The magnetic field signals detected at fixed positions were basically pulse-shaped with a relatively fast rise and a relatively slow decay. The magnetic probe signals were delayed further in time as the magnetic probe was

moved to positions of larger axial distance. In addition, the duration of the probe signals increased with axial distance. Thus, the magnetic field detected at fixed positions can be characterized as a pulse which propagates out from the target and broadens as it travels.

The propagation velocity of the magnetic field pulses was of the order of 10^6 - 10^7 cm/sec. This is the same order of magnitude as the expansion velocity of a laser plasma. Also, the duration of the magnetic field signal is considerably longer than the laser pulse in Figure 4. This indicates that the self-generated magnetic fields were not the magnetic components of the laser beam or of electromagnetic waves generated by the interaction of the laser beam with the target. Instead, the self-generated magnetic fields were produced by conduction currents associated with the laser plasma and were convected with it as it expanded.

C. LASER POWER DEPENDENCE

The dependence of the self-generated magnetic fields on the incident laser power density (power per unit target area) was investigated. This was done by varying the peak laser power incident on the target. It was then assumed that the cross sectional area of the beam did not vary with laser power. Then the incident laser power density is directly proportional to the laser power itself.

The results of monitoring the maximum azimuthal magnetic field at a fixed position (i.e. the peak field in the probe signal of Figure 4) versus the incident laser power are shown in Figure 5. For this particular background pressure of nitrogen, the magnetic field increases sharply with incident laser power for powers in the range of 150 MW to 250 MW. For higher laser powers, the magnetic field increases at a slower rate.

The dependence of the maximum azimuthal magnetic field on incident laser power was investigated at other ambient pressures of nitrogen gas in the range of 1 mTorr to 200 mTorr. In each case the magnetic field increased monotonically with incident laser power. However, the specific dependence of the field on the laser power was different for each pressure of nitrogen.

The investigation of the dependence of the magnetic field on the other parameters was done at a fixed incident laser power of 300 MW. This power was chosen because it lies between the range of powers for which the field increases sharply with laser power and the range of powers for which there is a large scatter of the field data (see Figure 5).

Because the laser output was reproducible only to within $\pm 15\%$, a series of three field measurements was needed at each probe position and ambient pressure to determine the value of the field at 300 MW of laser power.

The field values from the three measurements were graphed on a B versus laser power plot (like Figure 5), and the best straight line was drawn through the three points. The value of B corresponding to 300 MW along this line was taken for the value of the magnetic field at that probe position and ambient pressure.

The degree of uncertainty involved in measuring the magnetic fields can be estimated from the B versus power plots. In Figure 5 the average percentage of deviation of the measured field values from the curve drawn through them is 5%, and the largest deviation is 16%. Hence, the measured field values may be considered to be correct to within about 10%.

D. PRESSURE DEPENDENCE OF FIELDS

The most striking result of this investigation was the strong dependence of the self-generated magnetic fields on the ambient pressure of the nitrogen background gas. Figure 6 shows the variation of the maximum azimuthal magnetic field at a fixed position with the pressure of the nitrogen background gas.

There are three regions evident in Figure 6. For pressures lower than 1 mTorr, the magnitude of the magnetic field does not depend on the nitrogen gas pressure. For pressures in the range of 1-200 mTorr, the magnitude of the field rises very sharply with increasing pressure. At pressures higher than 200 mTorr, the magnitude of the

field rapidly decreases with increasing pressure. This curve exhibits an amplification of the field by a factor of 6 when the background gas pressure is increased from 1 to 200 mTorr.

The dependences of the self-generated magnetic fields on background gas pressure and on incident laser power are combined in Figure 7. This figure shows that the specific dependence of the magnetic field on the incident laser power varies with ambient pressure. The dependence of the field on ambient pressure, however, is essentially the same for each laser power. Thus, the laser power serves to merely scale the magnetic fields, while the ambient pressure affects the basic nature of them. For this reason the influence of the incident laser power on the self-generated magnetic fields was not investigated further.

E. SYMMETRY OF THE MAGNETIC FIELDS

The symmetry of the azimuthal magnetic fields about the z-axis as predicted by Eqn. 18 was tested.

In order to prevent probe perturbation effects, it was necessary to bring the magnetic probe into the vacuum chamber via the forward probe port in Figure 3. In this configuration, the glass tubing containing the probe was parallel to the plasma flow direction. To test the symmetry, the probe coil was moved to different positions along a circle of fixed radius centered on, and normal to,

the z-axis. At each position, the probe tubing exposes the same cross sectional area to the impinging plasma flow. Since the plasma flow is symmetric, any error in measuring the field which is a result of probe-induced perturbations will be the same at each angular position of the probe. Hence, the magnetic fields measured along the circle should display any symmetry of the field, even if perturbations are significant.

The results of measuring the azimuthal magnetic field around three different circles are presented in Table I. The fields were measured in a nitrogen background gas pressure of 250 mTorr and for an incident laser power of 300 MW. The results indicate that the self-generated magnetic fields were axisymmetric, within experimental error.

The necessity of taking these precautions regarding probe perturbation effects was demonstrated in the following test. The probe was brought into the vacuum chamber via the top probe port, and the field was measured at a certain radial distance directly above the z-axis ($\theta=0^\circ$). Next, the probe was pushed straight down through the z-axis so that the coil was located at the same radial distance below the z-axis ($\theta=180^\circ$). At this position, the probe tubing exposed more cross sectional area to the plasma flow and should have perturbed the flow more strongly. Not only was the magnitude of the field found not to be the same below the axis, the direction of the field signal

TABLE I

RESULTS OF SYMMETRY MAPPING OF AZIMUTHAL MAGNETIC FIELD

Circle Center Location	Circle Radius	Probe Angular Position	Maximum Magnetic Field (B)	Standard Deviation σ	$\frac{\sigma}{B_{\text{average}}}$
z=4 mm	r=12 mm	$\theta=0^\circ$	10 G	1.1 G	8.9%
		$\theta=45^\circ$	14 G		
		$\theta=90^\circ$	13 G		
		$\theta=135^\circ$	13 G		
		$\theta=180^\circ$	12 G		
		$\theta=225^\circ$	12 G		
		$\theta=315^\circ$	13 G		
z=4 mm	r=5 mm	$\theta=45^\circ$	83 G	6.4 G	7.3%
		$\theta=135^\circ$	99 G		
		$\theta=225^\circ$	84 G		
		$\theta=315^\circ$	86 G		
z=10 mm	r=5 mm	$\theta=0^\circ$	32 G	3.8 G	11%
		$\theta=45^\circ$	41 G		
		$\theta=135^\circ$	35 G		
		$\theta=225^\circ$	32 G		
		$\theta=315^\circ$	30 G		

did not reverse.⁴ Also, the azimuthal field did not vanish along the z-axis ($r=0$) as it should for an axisymmetric field.

The conclusion is that the probe seriously perturbed the plasma flow at positions near the z-axis. The minimum radius at which probe-measured values of the field could be considered meaningful was arbitrarily taken to be the same as the radius of the hole burned in the Mylar foil target, 1 mm. This is the initial radius of the laser plasma.

F. SPATIAL DEPENDENCE OF THE MAGNETIC FIELDS

1. Pressure Variation

The pressure variation of the maximum azimuthal magnetic field was checked at several positions along the $r=3$ mm line in the $\theta=0^\circ$ plane. Data was taken at $z=4$ mm, $z=8$ mm, and $z=1.4$ cm. The data taken at $z=4$ mm has already been presented (Figure 6).

At both $z=8$ mm and $z=1.4$ cm, the dependence of the field on background pressure resulted in curves which had the same basic shape as Figure 6. At each position there was a pressure-independent region, a field amplification region, and a field damping region. There were, however, two basic differences:

-
4. The symmetric azimuthal field is everywhere clockwise about the z-axis, as the properly performed symmetry test verified. Hence, the fields at symmetric positions about the axis are in opposite directions.

- (1) The magnitude of the field at each pressure was lower at increasingly larger axial distances. In other words, for a given pressure, $B(z=4 \text{ mm}) > B(z=8 \text{ mm}) > B(z=1.4 \text{ cm})$.
- (2) As the axial distance increased the largest magnetic field measured at that position occurred at a lower pressure. In other words, the transition pressure from the field amplification region to the field damping region was lower at a larger axial distance. This is displayed graphically in Figure 8.

These two results are not unrelated. The magnitude of the field for a fixed background pressure was found to decrease approximately exponentially with axial distance for background pressures higher than 50 mTorr. Further, the scale length for this exponential decay (e-folding length) was found to decrease with increasing pressure. As Figure 9 shows, in the range of 50-1000 mTorr, the scale length varied as

$$\lambda \propto P_b^{-.31} \quad (32)$$

where P_b is the background gas pressure. Hence, although the field at $z=4 \text{ mm}$ was larger for 100 mTorr than for 50 mTorr, at $z=1.4 \text{ cm}$ the reverse is true because the field decreases at a higher rate with distance in a background gas pressure of 100 mTorr.

2. Two-Dimensional Mapping of the Fields

The azimuthal magnetic fields were mapped extensively in the $\theta=0^\circ$ plane for three ambient pressures of nitrogen. These pressures were .1, 5, and 250 mTorr. They represent, respectively, pressures corresponding to the pressure-independent region, the onset of the field amplification region, and the field damping region (see Figure 6).

Figure 10 illustrates the probe location grid used in the mapping. Magnetic probe measurements were taken at each intersection point of the grid lines. At distances close to the target, the field's spatial structure was relatively fine, and a small grid spacing was used. At farther distances, the field's spatial structure was broader, and the grid spacing was increased in order to keep the number of mapping measurements down to a reasonable number. The minimum axial grid spacing was taken as 2 mm since this is the outside diameter of the glass tubing enclosing the probe and represents the order of the spatial resolution expected from the probes.

The field could not be measured in the rectangle in the lower left hand corner of the grid (see Figure 10). This is the region where the laser beam intersects the mapping grid as it comes in at 30° to it. A probe placed in this area would be struck and damaged by the laser beam. Unfortunately, this is where the early field formation is

occurring and represents a very interesting region. In the two-dimensional mapping results presented, this area will be left blank.

The results of the two-dimensional mapping will be presented as contour plots of the magnitude of the magnetic field. The contours are the loci of the points where the field has a common value. The direction of the field is perpendicular to the plane of the contour plot (i.e. perpendicular to the mapping plane). A positive field value corresponds to a clockwise orientation of the field about the z-axis in Figure 1 and a negative value to a counterclockwise orientation. Because of the symmetry of the azimuthal fields, these contour plots give full three-dimensional representations of the field when they are rotated about the z-axis.

In order to determine the contour levels, the probe data taken at each grid position was used as the input data of a computer program. The program first interpolated between data points to fill in any missing values of the field on a grid with a 1 mm spacing. Next, the program smoothed the field values by using the computer library subroutine SE13 which performs least-squares smoothing. Then the computer library subroutine CONTUR was used to compute the loci of the contour levels and plot them on the computer center's Calcomp plotter.

The results of the two-dimensional mapping of the maximum magnetic field values measured for any time at

each position are presented in Figure 11 for the three background gas pressures.

In preparing the contour plots, the magnetic field along the z-axis was taken to be zero. As mentioned previously, the magnetic field as measured by the probes along the z-axis did not vanish. However, this was believed to be due to serious probe-induced perturbations of the field. The field was determined to be symmetric about the z-axis and should, therefore, vanish along it.

The important features of the maximum magnetic field contours in Figure 11 are:

- (1) The field in the 250 mTorr case decreased more sharply with distance than did the field for the other two pressures.
- (2) The field contours in the 250 mTorr case are all of a similar oval shape, unlike the other two pressure cases.
- (3) The field in the .1 mTorr case is confined nearer to the z-axis than in the other two pressure cases.
- (4) The largest value of the magnetic field occurs at a larger distance from the target in the 250 mTorr case than in the other two pressure cases.

3. One-Dimensional Mapping of the Fields

The field measurements along the $r=4$ mm line were extended to a larger axial distance (to $z=6$ cm) than were

the measurements in the two-dimensional mapping grid. This allowed the fields to be followed in their propagation direction for greater distances than could be economically accommodated in a two-dimensional grid.

The maximum magnetic fields measured along that line are displayed in Figure 12 for the three pressure cases. This figure allows a more direct comparison of the rates of spatial variation of the fields than does the two-dimensional contour plot.

As Figures 11 and 12 show, the fields for 250 mTorr were characterized by a very sharp decrease with distance relative to the fields for the lower pressures. Figure 12 shows that although the largest field was twice as large in the 250 mTorr case as in the 5 mTorr case, the spatial extent of the field in the 5 mTorr case was more than twice that in the 250 mTorr case.

The rates of decrease of the maximum magnetic field with axial distance for .1 mTorr and for 5 mTorr were approximately the same, although the fields decay slightly faster with distance in the .1 mTorr case.

Figure 12 shows that along $r=4$ mm, the magnetic fields reached their largest values at distance out in front of the target rather than at its surface. This result is partly due to the convection of the fields to the $r=4$ mm line. Since the laser plasma which carried the fields moved mainly in the z -direction as it expanded

radially, the largest field intercepted the $r=4$ mm line at a larger axial distance than where it actually originated.

G. TIME DEPENDENCE OF THE MAGNETIC FIELDS

1. Time Decay of the Magnetic Fields

The manner in which the magnetic fields decay with time is shown in Figure 13.⁵ This figure gives the maximum magnetic field detected at any axial position along $r=4$ mm versus time.

The field in the 250 mTorr case decayed exponentially with time from 60 nsec until 320 nsec, as shown in Figure 14. The time constant of the decay was 92 nsec, so that

$$B = B_0 e^{-(t-60)/92} \quad 60\text{ns} \leq t \leq 320\text{ns} \quad (33)$$

where B_0 is the value of the field at 60 nsec and t is in nsec.

The maximum fields in the other two background pressure cases decayed at slower nonexponential rates. However, the fields in the .1 mTorr case decayed slightly faster and became negligible at about 360 nsec, while the fields for a background pressure of 5 mTorr remained significant for more than 1.6 μ sec.

5. The reference time ($t=0$) for all time studies was the time at which the laser power attains its maximum value.

2. Two-Dimensional Mapping

The results of the two-dimensional mapping of the magnetic fields were time resolved so that both the temporal and the spatial behavior of the fields in the $\theta=0^\circ$ plane could be studied. The results are presented in Figures 15 - 49.

The important features of the .1 mTorr case are:

- (1) The probe signal which appears initially at distances far from the target (i.e. in the region $z \geq 9$ mm in Figure 15) is in reality electrostatic pickup from the laser plasma. The precautions taken insure that the electrostatic signals were not generated externally to the vacuum chamber. These pickup signals had a maximum strength of .3 mV (which would represent 2 Gauss if they had been magnetic in origin) in Figure 15 and preceeded the beginning of the magnetic field signal at each position, as inspection of Figures 15 - 26 reveals. The electrostatic signals appear to cease once the magnetic field arrives at the probe position so that they do not interfere with the magnetic field signals. Hence, the magnetic field contours are easily distinguished from the electrostatic signal contours in Figures 15 - 26 except near their

common boundary. The electrostatic signal contours are labeled with their magnetic field strength equivalents so that the seriousness of the pickup can be evaluated.

This same electrostatic pickup was also present on the magnetic probe signals for the other two ambient pressures of nitrogen at distances greater than about 1 cm. In those cases, however, the strengths of the pickup signals were significantly lower than the strengths of the field signals, due to the stronger fields detected for the higher ambient pressures. This allowed the pickup signals to be eliminated from the probe data before the data were used in the computer program to generate the contour plots. For that reason, the contours of the electrostatic signals do not appear for 5 and 250 mTorr in Figures 15 - 49.

- (2) The flow of the magnetic field is almost exclusively in the z-direction. The field is more confined to the region near the z-axis than are the fields for the other two pressures.
- (3) There is a core of the highest magnetic field which does not propagate out beyond about 6 mm at 160 nsec.

- (4) A faster component of magnetic field causes the contour lines to be distorted in the z-direction starting at about 80 nsec. At 140 nsec this faster component has separated from the core of high field.
- (5) The core of high field quickly decays after 140 nsec and is no longer evident by 200 nsec.
- (6) The faster component of the field can be described as a shell of field after about 180 nsec.
- (7) After this field shell has left the mapping region, the fields begin to reverse their direction near the target (340 nsec). This field reversal continues until almost all of the field in the mapping region has been reversed.
- (8) After 800 nsec the magnitude of the fields becomes insignificant.

The important features of the 5 mTorr case are:

- (1) As in the .1 mTorr case, there is a core of highest field which does not propagate out beyond about 5 mm at 220 nsec.
- (2) Also like the .1 mTorr case, this core of high field decays quickly and is no longer evident by 240 nsec.

- (3) Again like the .1 mTorr case, there is a faster component of the field which distorts the field contours in the z-direction near the z-axis ($r \leq 6$ mm).
- (4) This faster component can also be described as a shell from 180 nsec until 280 nsec. During this time, this shell is located at the same positions as the shell for .1 mTorr at each instant.
- (5) There is an additional distortion of the field contours at larger radial distances ($r \geq 6$ mm) which starts at 60 nsec and lasts until about 200 nsec.
- (6) During this time, there are field contours outside of the distorted region. These contours extend far beyond the field contours in the .1 mTorr case.
- (7) The field contours form into a shell starting at about 300 nsec.
- (8) After the field shell leaves the mapping region, the field begins to reverse its direction (1.4 μ sec) near the target.

The important features of the 250 mTorr case are:

- (1) The oval-shaped field contours propagate without distortion until about 180 nsec.
- (2) The core of highest field propagates with the other contours. This core stays ahead of the

cores in the lower pressure cases. However, when the fast shells emerge in the lower pressure cases at 180 nsec, they are ahead of the core in the 250 mTorr case.

- (3) Serious distortions of the field contours begin at 220 nsec. These distortions are of a different character than those in the two lower pressure cases. Two islands of depressed field begin to form at 260 nsec at $z=1.5$ cm, $r=6$ mm and at $z=6$ mm, $r=7$ mm. The fields become further depressed in these regions and finally reverse their direction at 300 nsec. At 360 nsec the two islands join.
- (4) The fields increase in magnitude in the reverse direction. By 500 nsec, the field is reversed everywhere in the mapping plane. The fields reach a maximum strength of 10 Gauss in the reverse direction at 600 nsec.

3. One-Dimensional Mapping of the Magnetic Field

The magnetic fields measured along the $r=4$ mm line were also time resolved to determine how the spatial variation of the fields changed with time in one dimension. The results are presented in Figures 50 - 58. These figures allow direct comparisons of the three pressure cases.

Many of the features pointed out in the two-dimensional contour plots (Figures 15 - 49) are evident in the one-dimensional field profiles.

Figures 50 - 58 illustrate the general propagation and spatial broadening of the fields. The propagation velocities reach maximum values at about 100 nsec and then decrease with time. For .1 mTorr, the position of highest field propagated at a maximum velocity of 9×10^6 cm/sec. For 5 mTorr, the maximum velocity was 10^7 cm/sec. For 250 mTorr, the field maximum travelled at a highest velocity of 6.5×10^6 cm/sec.

The broader spatial extent of the field profiles for 5 mTorr is one of the most striking features of Figures 50 - 58. By 120 nsec, the field for 5 mTorr extends nearly 5 mm beyond the fields for the other two pressures. At later times the differences in spatial extents become even larger.

Figures 50 - 58 also illustrate the formation of the field profiles into shells. The shell structure of the field becomes evident at 280 nsec for .1 mTorr, but not until 440 nsec for 5 mTorr.

H. SUMMARY OF EXPERIMENTAL RESULTS

The most important results of this investigation were:

- (1) The self-generated magnetic fields were produced by conduction currents associated with an expanding laser plasma and were not the magnetic components of an electromagnetic wave.

- (2) The direction of the fields was primarily azimuthal about the z-axis, and the fields were initially in the clockwise direction about that axis in Figure 1.
- (3) The fields were symmetric in magnitude about the z-axis.
- (4) The magnitude of the fields increased with incident laser power.
- (5) The magnitude of the fields was strongly dependent on the ambient pressure of nitrogen gas at pressures above 1 mTorr.
- (6) The presence of the background gas can result in amplification of the magnitudes of the fields above their high-vacuum values.
- (7) Both the spatial and the temporal behavior of the fields were governed by the ambient pressure of the gas.
- (8) Differences between the fields for different pressures of gas were detected even at $t=0$.
- (9) Of the three background gas pressures used extensively, the fields were the strongest for 250 mTorr but also decayed the fastest both spatially and temporally for that pressure.
- (10) The fields for 5 mTorr of nitrogen had a broader spatial extent at each instant of time than did those for .1 mTorr.

(11) The direction of the magnetic fields reversed at late times for all three pressures. The field reversal for 250 mTorr occurred noticeably earlier than for the other two pressures.

VII. CALCULATED EXPERIMENTAL PARAMETERS

A. LASER PLASMA PARAMETERS

In order to obtain some estimates on the laser plasma parameters for an expansion into a high vacuum, Eqns. 8 and 9 were programed for computer analysis.

Use of these equations requires knowledge of the total mass of the laser plasma, the charge state of each ion, and the fraction of absorbed laser energy which appears as the thermal and kinetic energy of the plasma. Unfortunately, there was no direct knowledge of any of these parameters.

The total mass of the target which was burned off by the laser could be determined simply by weighing the target before and after laser irradiation. This is not the total mass of the plasma unless it has been completely ionized, i.e. some of the blow-off may remain neutral. The spectroscopic measurements needed to determine the degree of ionization and charge state of the ions were unavailable in this study.

The fraction of the incident laser beam energy which was absorbed by the target in this experiment has been measured to be about 90% [Ref. 14]. However, some of this energy must be used to dissociate and ionize the target. This fraction is not available as thermal or kinetic energy for the plasma. The theory in Section IIA assumes

that the target is initially a cold, fully ionized plasma. Hence, the dissociation and ionization energies must be subtracted from the incident laser beam energy before it can be used as input data in the computer simulation. However, these parameters were not determined experimentally in this investigation.

An appeal can be made to data published for similar experimental circumstances in order to get some rough ideas of these parameters. Mylar ($C_{10}H_8O_4$) is mostly carbon, and Ready [Ref. 9] has published data on the parameters of a laser-produced carbon plasma. The data show that for the peak laser irradiance of this experiment (10^{10} W/cm²), the peak temperature of the plasma was 10 eV and the asymptotic expansion velocity of the front was 10^7 cm/sec. Also, using a polyethylene film (C_2H_4) and similar laser parameters, Boland [Ref. 17] found an average charge state of 2.3 electrons per ion, that only 4% of the blow-off material had been ionized, and that 75% of the laser energy had appeared as thermal and kinetic energy in the plasma (although 90% of the incident laser energy had been absorbed).

In the computer program, a charge state of 2.3 was assumed, and 25% of the laser energy was assumed either not to be absorbed or used to dissociate and ionize the target. The total mass of the laser plasma was then adjusted until the computer results indicated a peak plasma

temperature of 10 eV and an asymptotic expansion velocity of the front of 10^7 cm/sec.

The mass required to attain these results (10 eV, 10^7 cm/sec) was 6.53×10^{-6} g corresponding to 4.5×10^{17} particles. The mass of the target vaporized by the laser was 5.2×10^{-4} g. Hence, only about 1% of the target material vaporized by the laser was contained in the expanding laser plasma. The remaining mass of neutral target material consisted partly of neutral atoms ejected near the end of the laser pulse after the strong plasma heating was over. Large pieces of the Mylar target material were also ejected. The ejected neutrals have much smaller kinetic energies than do the ionized components of the laser plasma. Hence, the neutrals will not expand with the laser plasma, and the laser plasma can be considered to be fully ionized.

The results of the computer simulation are given in Figure 59. This figure gives the time behavior of the plasma temperature, front position, and front velocity. In Figure 59 the laser pulse begins at 0 nsec, reaches its peak at 25 nsec, and becomes negligible by 50 nsec.

These results are based on the one-dimensional model discussed in Section IIA. Although the laser plasma actually undergoes a radial as well as an axial expansion, Figure 59 can be used for a crude estimate of the laser plasma parameters.

The laser plasma electrical conductivity at the time of highest temperature can now be estimated. The dc conductivity is given by

$$\sigma = \frac{n_e e^2}{m_e v_e} \quad (34)$$

where v_e is the electron collision frequency. For electron-ion collisions [Ref. 18]

$$v_{ei} = 3.62 \times 10^{-6} n_i T_e^{-3/2} \ln \Lambda \quad \text{sec}^{-1} \quad (35)$$

where T_e is in $^{\circ}\text{K}$ and n_i in m^{-3} . For the laser plasma at the time of its peak temperature, n_i was $6 \times 10^{19} \text{ cm}^{-3}$ so that v_{ei} was $6.9 \times 10^{13} \text{ sec}^{-1}$. Hence, the conductivity was $5.7 \times 10^4 \text{ mho/m}$ at that time.

The electron-ion thermalization time is of interest because it must be sufficiently short if a common ion and electron temperature in the laser plasma can be assumed. The electron-ion thermalization time is given by [Ref. 1]

$$t_{ei} = \frac{1.05 \times 10^{13} A T_e^{3/2}}{n_e Z \ln \Lambda} \quad (36)$$

where A is the atomic weight of the ions, n_e is in cm^{-3} , and T_e is in keV. For Mylar the average atomic weight is about 9, and at the time of the peak temperature of the laser plasma n_e was $1.4 \times 10^{20} \text{ cm}^{-3}$. Then t_{ei} was about $2.9 \times 10^{-11} \text{ sec}$. Hence, on the time scale of the laser heating (10^{-9} sec) a common ion-electron temperature can be assumed, and the use of a common temperature in the laser plasma theory (see Section IIA) is justified.

Also of interest is the Debye length since it is the distance over which thermal forces can cause significant charge separation. The importance of this process in connection with the generation of the self-generated magnetic fields was discussed in Section IIC. The Debye length is given by [Ref. 18]

$$\lambda_D = 6.9 \times 10^3 \left(\frac{T_e}{n_e} \right)^{1/2} \text{ cm} \quad (37)$$

where T_e is in $^{\circ}\text{K}$ and n_e in m^{-3} . For the laser plasma at its peak temperature, n_e was $1.4 \times 10^{20} \text{ cm}^{-3}$ so that λ_D was $1.8 \times 10^{-7} \text{ cm}$.

The electron plasma frequency is given by [Ref. 18]

$$\nu_{ep} = 8.99 n_e^{1/2} \text{ sec}^{-1} \quad (38)$$

where n_e is in m^{-3} . For the laser plasma at the time of its peak temperature, ν_{ep} was $1.1 \times 10^{14} \text{ sec}^{-1}$ showing that neglect of the inertia term in Eqn. 14 was justified.

Finally, the time constant for heat conduction is [Ref. 5]

$$\tau_h = \frac{z(n_e + n_i) \ell^2}{2.93 \times 10^{27} T_e^{5/2}} \quad (39)$$

where ℓ is the characteristic length for the laser plasma temperature in cm, n_e and n_i are in cm^{-3} , and T_e is in keV. For the laser plasma at the time of its peak temperature, ℓ was about 1 mm, the initial radius of the laser plasma, so that τ_h was about $1.5 \times 10^{-4} \text{ sec}$. For an

expansion into a vacuum, the plasma temperature decreases adiabatically after laser shut-off. In that case, the temperature decreases as

$$T \propto V^{-2/3} \quad (40)$$

where V is the laser plasma volume. Since

$$n \propto V^{-1} \quad (41)$$

then Eqn. 39 shows that τ_h varies as

$$\tau_h \propto V^{2/3} \ell^2 \quad (42)$$

so that τ_h increases as the laser plasma expands adiabatically. Thus, for the parameters considered here, the time constant for heat conduction remains longer than the times of experimental interest, under adiabatic conditions. This means that the radial temperature gradient of the laser plasma which resulted as a consequence of the heating by the Gaussian laser beam (as discussed in Section IIC) will remain throughout the expansion of the laser plasma, for the case of low ambient pressures (i.e. .1 mTorr).

B. PHOTOIONIZATION OF THE BACKGROUND

The ambient gas is ionized primarily by the Bremsstrahlung from the laser plasma. The equation governing this process is [Ref. 19]

$$\frac{\partial n_e(\vec{r}, t)}{\partial t} = \frac{1}{4\pi r^2} \int_{v_0}^{\infty} \frac{\sigma(v) n_n(\vec{r}, t) P(v, t) e^{-\sigma n_n r}}{h\nu} dv \quad (43)$$

where n_e and n_n are the electron and the neutral densities in the background, r now refers to the radial distance from the origin, v is the photon frequency, $h\nu_0$ is the ionization potential of the background atoms, σ is the photoionization cross section, and $P(v, t)$ is the spectrum of the Bremsstrahlung power.

This equation can be simplified by assuming that all of the Bremsstrahlung power for $v > v_0$ is concentrated at v_0 . In other words, the photons have a highest frequency of v_0 . This assumption will lead to a higher photoionization than Eqn. 43 predicts, but this equation only considers single ionization by Bremsstrahlung. Then the actual ionization would be greater than Eqn. 43 predicts, and the assumption partially compensates for this.

Under the assumption, Eqn. 43 can be written

$$\frac{\partial n_e(\vec{r}, t)}{\partial t} = \frac{\sigma(v_0) n_n(\vec{r}, t) e^{-\sigma n_n r}}{4\pi r^2 h\nu_0} \int_{v_0}^{\infty} P(v) dv \quad (44)$$

The integral in this equation is the total Bremsstrahlung power at frequencies such that $v \geq v_0$. The power spectrum is given by [Ref. 8]

$$P(v) = K e^{-h\nu/kT} \quad (45)$$

where K is a constant. If Eqn. 45 is integrated over all frequencies, the result is the total emitted Bremsstrahlung power. The constant K can then be expressed in terms of the total power, and Eqn. 45 becomes

$$P(\nu) = \frac{h}{kT} P_T e^{-h\nu/kT} \quad (46)$$

where P_T is the total Bremsstrahlung power given by

$$P_T = 1.52 \times 10^{-32} z^3 (kT)^{1/2} \int n_i^2 dV \quad \text{Watts} \quad (47)$$

where kT is in eV and n_i^2 in $(\text{cm}^{-3})^2$ is integrated over the laser plasma volume.⁶

Then Eqn. 44 becomes

$$\frac{\partial n_e(\vec{r}, t)}{\partial t} = \frac{\sigma(\nu_0) n_n(\vec{r}, t) e^{-\sigma n_n r}}{4\pi r^2 h\nu_0} P_T e^{-h\nu_0/kT} \quad (48)$$

If $\sigma n_n r \ll 1$, the background gas is "optically thin," and Eqn. 48 predicts that the degree of ionization $n_e(\vec{r}, t) / n_n(\vec{r}, 0)$ will be independent of background pressure. For nitrogen, $\sigma(\nu_0)$ is $9 \times 10^{-18} \text{ cm}^2$. The highest background pressure used in the mapping was 250 mTorr, so that n_n .

6. Energy losses from the plasma by radiation were neglected in deriving the energy balance equation for the laser plasma (Eqn. 3). According to Eqn. 47, the power radiated by the plasma when it is hottest is 16 MW. At that time, the incident laser power is 300 MW, justifying the neglect of the radiated power loss in Eqn. 3.

was initially $8.05 \times 10^{15} \text{ cm}^{-3}$. Then for 250 mTorr, σn_n was initially $7.25 \times 10^{-2} \text{ cm}^{-1}$, giving a photon mean free path of about 14 cm. Hence, the background gas was "optically thin" for the pressures and observation distances used, and the degree of ionization of the background was independent of pressure.

For nitrogen, $h\nu_0$ is 14.55 eV. The peak plasma temperature was 10 eV. Then Eqn. 48 predicts low levels of ionization in the background except very near the laser plasma.

Equation 48 was run in a computer program in which the plasma densities and temperatures calculated from Eqns. 8 and 9 were used as input data. The results are given in Figure 60. This figure shows that the degree of ionization became negligible beyond 2 cm.

Near the laser plasma during its peak temperature, the background gas is fully ionized, and the nitrogen ions are more likely doubly ionized. If the electron temperature of the ambient plasma is estimated to be 1 eV, and double ionization is assumed, then the dc conductivity is independent of the ambient plasma density and from Eqns. 34 and 35 was $1.6 \times 10^3 \text{ mho/m}$. This is about 3% of the estimated conductivity of the laser plasma. The conductivity of the background plasma decreased with distance because the density of the neutral particles increased causing an increase in the electron-neutral collision

frequency. The conductivity of the ambient plasma remained independent of density at large distances, however, because the degree of ionization was pressure-independent.

The Debye length of the ambient plasma does depend on density. Near the laser plasma where the ambient plasma was fully ionized, the Debye length was 3.8×10^{-4} cm for .1 mTorr, 5.4×10^{-5} cm for 5 mTorr, and 7.8×10^{-6} cm for 250 mTorr.

The electron-ion thermalization time for the fully ionized ambient plasma near the laser plasma can be estimated by assuming T_e is about 1 eV in Eqn. 36. Then t_{ei} becomes 3.6×10^{-5} sec for .1 mTorr, 7.0×10^{-7} sec for 5 mTorr, and 1.5×10^{-8} sec for 250 mTorr.

The time constant for heat conduction in the fully ionized region of the ambient plasma can also be evaluated by assuming l is about 1 cm in Eqn. 39. Then τ_h becomes 2×10^{-8} sec for .1 mTorr, 10^{-6} sec for 5 mTorr, and 5×10^{-5} sec for 250 mTorr.

In the interaction region between the laser plasma and the ambient plasma, the ambient plasma will be heated as it is swept into a density shell at the front of the laser plasma. The density of the ambient plasma will be enhanced in the density shell. Assuming that it is enhanced by a factor of ten in the density shell, the electron-ion thermalization time and the time constant for heat conduction for the heating process in the density shell can be estimated. Equations 36 and 39 show that t_{ei} decreases by

an order of magnitude for each ambient pressure in the density shell and τ_h increases in each case by an order of magnitude. Then for 5 mTorr and 250 mTorr, t_{ei} is short and τ_h is long in the density shell compared to the time scale of the interaction between the laser plasma and the ambient plasma ($\sim 10^{-7}$ sec). Thus, temperature gradients can exist in the density shell for the times of interest. The conductivity in the density shell does not vary with density.

C. CHARACTERISTICS OF THE SELF-GENERATED MAGNETIC FIELDS

1. Current Density

The current density distributions which produce the self-generated magnetic fields are determined by applying

$$\vec{\nabla} \times \vec{B} = \mu_0 \vec{J} \quad (49)$$

to the magnetic field data.

The typical current density pattern for 250 mTorr is displayed in Figure 61. The largest current density in this pattern is 6.12×10^2 amp/cm². The current flow was toroidal in three dimensions, and there was no current in the azimuthal direction. The current density was strongest along the z-axis and reached its largest observed values as soon as the magnetic field contours began to emerge from the inaccessible area in the mapping plane (see Figure 10). The peak current densities observed

were 3.60×10^2 amp/cm² for .1 mTorr, 5.57×10^2 amp/cm² for 5 mTorr, and 1.53×10^3 amp/cm² for 250 mTorr.

The current density configurations became more complicated when the magnetic field contours were distorted from an oval shape. Figure 62 shows the current density distribution for 5 mTorr at 120 nsec, a time at which some of the magnetic field contours have been seriously distorted (see Figure 21). When Figure 62 is referred to Figure 21, it is noted that the current density is circulating about the area of the distortion in the 20 Gauss contour line ($z \approx 9$ mm, $r \approx 1.1$ cm).

2. Magnetic Field Energy

The total energy residing in the magnetic field can be computed from the field data by using

$$E_B = \int \frac{B^2}{2\mu_0} dV \quad (50)$$

where the integration is over the region of observation. For this experiment, the fields had cylindrical symmetry, and Eqn. 50 becomes

$$E_B = 2\pi \int \frac{B^2(r, z)}{2\mu_0} r dr dz \quad (51)$$

This integral is evaluated in the mapping plane for the fields.

The results for the three different background pressures are given in Figure 63. The initial increases in the field energy were due to the emergence of the

field contours out of the region of the mapping plane.

The important features of Figure 63 are:

- (1) The magnetic field energy for 5 mTorr and 250 mTorr is initially two orders of magnitude larger than that for .1 mTorr.
- (2) The field energy for .1 mTorr stays nearly constant at about 3 ergs after the field contours emerge. The onset of the decrease in the field energy at 280 nsec corresponds to the time at which the largest-valued field contours leave the observation region (see Figure 29).
- (3) From 80 nsec until 180 nsec, no significant field has entered or left the mapping region (see Figures 19 - 24) in the case of 250 mTorr. However, Figure 63 shows a sharp decrease in the magnetic field energy during this time. The field energy begins a sharper decrease at 180 nsec as the field flows out of the observation region. At 360 nsec the field energy stops decreasing and begins to increase again. Figure 33 shows that at this time there is strong field reversal for 250 mTorr. The field energy remains nearly constant over a long period of time although the field is flowing out of the observation region at these late times (see Figure 38).

- (4) The magnetic field energy for 5 mTorr continues to increase after 100 nsec even though the field contours have emerged considerably from the inaccessible mapping region (see Figure 20). From 100 nsec until 260 nsec the energy of the magnetic field increases by a factor of two, although the field contours show that very little field is emerging from the inaccessible region (see Figures 20 - 28). The field energy remains about constant from 260 nsec until 400 nsec. At late times the energy decreases due to the flow of the field out of the observation region.
- (5) It is interesting to note that the largest observed field energy (336 ergs) represents less than .001% of the absorbed laser energy.

3. $\vec{J} \times \vec{B}$ Force Density

The self-generated magnetic fields can influence the dynamics of the laser plasma expansion via the $\vec{J} \times \vec{B}$ force.

The typical $\vec{J} \times \vec{B}$ force density pattern for 250 mTorr is displayed in Figure 64. The largest force density in this pattern is 1.4×10^4 nt/m³. Since the current density was strongest near the z-axis where it was primarily in the -z-direction (see Figure 61), the strongest $\vec{J} \times \vec{B}$ force density was in the -r-direction (see Figure 64) and acted to "pinch" the laser plasma.

The radial pressure gradient of the laser plasma opposes this pinching force. In order to compare the relative strengths of the $\vec{j} \times \vec{B}$ force and the radial pressure gradient, an order of magnitude evaluation can be made on the laser plasma parameters. The laser plasma dimensions can be estimated from its expansion velocity. For 250 mTorr the expansion velocity was 6.5×10^6 cm/sec in the axial direction and about half of that value in the radial direction. Then at 120 nsec, the dimensions of the laser plasma in this case was about $z=8$ mm, $r=4$ mm (note that this is the position of the highest field for 250 mTorr in Figure 21). If a plasma temperature of 1 eV is assumed, then the radial pressure gradient of the laser plasma is about 1.5×10^8 nt/m³ at this time. Hence, for 250 mTorr at 120 nsec, the ratio of the $\vec{j} \times \vec{B}$ force density to the radial pressure gradient of the laser plasma is of the order of 10^{-4} . Thus, at this time the effect of the magnetic field on the dynamics of the laser plasma can be neglected.

This situation also holds initially. (i.e. at the peak of the laser pulse) This can be shown to be the case by evaluating $\vec{j} \times \vec{B}$ by the use of Maxwell's equation and vector identities. From Eqn. 49

$$\vec{j} \times \vec{B} = \frac{1}{\mu_0} (\vec{\nabla} \times \vec{B}) \times \vec{B} \quad . \quad (52)$$

By vector identities, this reduces to

$$\vec{j} \times \vec{B} = -\frac{1}{2\mu_0} \vec{\nabla} B^2 + (\vec{B} \cdot \vec{\nabla}) \vec{B} \quad . \quad (53)$$

But the second term vanishes due to the axisymmetric nature of the fields. Hence,

$$\vec{j} \times \vec{B} = -\frac{1}{2\mu_0} \vec{\nabla} B^2 \quad . \quad (54)$$

This equation shows that the ratio of the $\vec{j} \times \vec{B}$ force density to the radial pressure gradient reduces approximately to the ratio of the magnetic field energy density to the thermal energy density of the laser plasma. Initially, the thermal energy of the laser plasma was of the order of 1 J, the absorbed laser energy. On the other hand, Figure 63 seems to indicate that for 250 mTorr the field energy was initially of the order of 10^3 ergs or 10^{-4} J. At lower ambient pressures, both the magnetic fields and the current densities are smaller than those used in this analysis while the laser plasma pressure gradient is essentially the same. Hence, the $\vec{j} \times \vec{B}$ force density can be neglected initially in comparison with the laser plasma pressure gradient.

This analysis indicates that an azimuthal magnetic field of at least 100 times the magnitude of the field present in this experiment for 250 mTorr of nitrogen is needed if it is to affect the dynamics of the laser plasma. This would be a field of about 10-50 kGauss.

4. Magnetic Field Diffusion Time

The magnetic field diffusion time is given by
Eqn. 21

$$\tau_m = \mu_o \sigma L^2 \quad . \quad (21)$$

The characteristic lengths of the magnetic fields can be estimated by examining the contour plots of the fields. At the earliest times L is of the order of 1 mm. Then using the estimated laser plasma conductivity, initially τ_m is 72 nsec in the laser plasma. Since the conductivity of the ambient plasma was estimated to be an order of magnitude lower than that of the laser plasma, initially τ_m is about 2 nsec in the ambient plasma.

Figure 14 shows that the diffusion time for 250 mTorr was 92 nsec from 60 nsec until 320 nsec. Using this value in Eqn. 21 together with Eqn. 34 for the conductivity allows the electron temperature of the plasma to be estimated. The values of the scale lengths for the magnetic field in the case of 250 mTorr are obtained from the contour plots (Figures 15 - 49). The results are that the estimated electron temperature decreased from 1.4 eV at 60 nsec to .6 eV at 220 nsec. Hence, the electron temperature of the plasma is about 1 eV at these times.

If the temperatures estimated for the 250 mTorr case are used, the diffusion times for the other two

pressure cases can be estimated. At 60 nsec Figure 18 shows that the scale length for the field in the .1 mTorr case is 5 mm, the same as for the 250 mTorr case. Then τ_m will be about 92 nsec for .1 mTorr at 60 nsec if the electron temperature determined from the data for 250 mTorr is used. For 5 mTorr Figure 18 shows that L is about 1 cm at 60 nsec, so that τ_m will be 370 nsec for this ambient pressure.

5. Magnetic Reynolds Number

The ratio of the convection term to the diffusion term in Eqn. 18 is called the magnetic Reynolds number and is given by

$$R = Lv\mu_O\sigma = \frac{v\tau_m}{L} \quad (55)$$

Initially v is 10^7 cm/sec so that R is about 7. This indicates that initially the convection of the field dominates over diffusion.

At 60 nsec, R has decreased to about 1 for 250 mTorr, so that diffusion and convection of the field are comparable. Using the diffusion times determined above, R has become about 2 for .1 mTorr and about 4 for 5 mTorr.

VIII. THEORETICAL MODEL FOR THE PRESSURE DEPENDENCE OF THE FIELDS

The theory developed from the source term of Eqn. 18 seems to adequately explain the gross features of the magnetic fields. However, the theory in Section IIC was not developed sufficiently to account for the strong pressure dependence of the fields. That will be done in this section.

If an ambient plasma is present, the expanding laser plasma will couple to it. If the density of the ambient plasma is high enough so that the mean free path for binary collisions between the laser plasma ions and the ambient plasma ions is smaller than the dimension of the laser plasma, the coupling will be collisional in nature. At lower ambient pressures, collisionless coupling will arise because the presence of the self-generated magnetic field at the front of the laser plasma will lead to coupling via the ion-ion two-stream instability in the presence of a magnetic field.

As a result of the coupling, ambient plasma will be swept up at the front of the expanding laser plasma, and a density shell will form. The shell will contain a density gradient in the $-z$ -direction. Then field generation can occur in the density shell if a radial temperature gradient arises. The interaction between the laser

plasma and the ambient plasma will cause the swept up background to be heated in the density shell. This heating will be greatest where the relative velocity between the two plasmas is greatest: along the z -axis. Hence, a temperature gradient arises in the density shell in the $-r$ -direction. Then the density and the temperature gradients are in the same directions in the density shell as they are in the front of the laser plasma. These gradients will also be axisymmetric due to the symmetry of the expanding laser plasma. Hence, magnetic fields are generated in the density shell formed at the front of the expanding laser plasma, and these fields have the same symmetry and direction as those produced in the front of the laser plasma.

As a result of the interaction between the laser plasma and the ambient plasma, the magnetic field initially generated in the front of the laser plasma will be enhanced. The amount of enhancement will depend on the magnitude of the density and the temperature gradients in the density shell and the length of time they can be maintained. As long as there is an interaction between the laser plasma and the ambient plasma, these gradients can be maintained. Thus, unlike the field production in the front of the laser plasma, the field production in the density shell can continue long after laser shut-off. Field production will finally become negligible as the laser plasma decelerates

due to the interaction with the ambient plasma and as diffusion of the density shell into the laser plasma lowers the density gradient.

IX. ANALYSIS OF EXPERIMENTAL RESULTS

A. GENERAL

The fields were found to have the orientation and symmetry predicted by the source term of Eqn. 18. Also, the fields were convected at velocities of about 10^7 cm/sec. Since this is the expected front velocity of the laser plasma, this appears to verify that the highest fields were at the front of the laser plasma.

Figure 63 shows that the three ambient pressure cases can be conveniently classified. For .1 mTorr, the field energy remains about constant after laser shut-off. For this pressure, no significant additional magnetic field is produced by an interaction with the background plasma, and diffusion of the field is not serious. For 5 mTorr, field generation in the density shell continues long after laser shut-off, and field generation dominates over diffusion. For 250 mTorr, diffusion of the field quickly dominates over generation, and this case is characterized by strong dissipation of the field.

B. ENHANCEMENT OF THE MAGNETIC FIELD WITH AMBIENT PRESSURE

The enhancement of the magnetic field with ambient pressure (see Figure 6) was a result of the extra field generated as a result of the interaction between the ambient plasma and the laser plasma.

Figure 63 shows that the field energy for 250 mTorr was two orders of magnitude larger than that for .1 mTorr. This fact could only be true if more field were generated for an ambient pressure of 250 mTorr.

Further, the extra field was produced primarily in the density shell which formed at the front of the laser plasma as it swept up the ambient plasma. If the axial density gradient of the shell is approximated by n_e/δ where δ is the width of the density shell, then the addition to the source term becomes

$$S' = \frac{k}{en_e} |\vec{\nabla} T_e \times \vec{\nabla} n_e| \approx \frac{k \nabla_r T_e}{e \delta} \quad (56)$$

where $\nabla_r T_e$ is the radial temperature gradient of the density shell. During the initial generation of the field which occurs during the strong laser heating, $\nabla_r T_e$ in the density shell should be about the same as in the laser plasma and can be regarded as approximately independent of ambient pressure. Hence, the additional field produced in the density shell should scale roughly as

$$\Delta B \propto \frac{1}{\delta} \quad (57)$$

Under experimental conditions similar to those of this investigation, Dean [Ref. 11] has measured the width of the density shell swept up at the front of an expanding laser plasma. He found that for a background of nitrogen δ decreased with ambient pressure. Further, he found that

when the ambient pressure was increased from 25 mTorr to 200 mTorr, δ decreased by a factor of two. Reference to Figure 6 shows that the additional field above the pressure-independent value is 99 Gauss for 25 mTorr and 192 Gauss for 200 mTorr. Thus, the additional field increased by the same factor that δ decreased by. Hence, the scaling of the additional field in this pressure range agrees with Eqn. 57.

Dimensional analysis can be used to check the ability of Eqn. 56 to account for the magnitude of the extra field. If δ is obtained from Dean's data [Ref. 11] for 200 mTorr (1.2 mm), then Eqn. 56 predicts that the extra field of 200 Gauss could be generated in 10 nsec if the temperature in the density shell varied by 2 eV in about 1 mm. This is quite possible, although no temperature measurements were available to verify it.

The pressure-independent region of Figure 6 is due to the negligible interaction between the laser plasma and the ambient plasma for low ambient pressures. Probably, the heating of the ambient plasma swept up at the front of the laser plasma is not sufficient to cause significant field production in the density shell. Then for .1 mTorr, the field detected was presumably all generated in the front of the laser plasma. An estimate of the strength of this field during the early laser heating can be obtained by extrapolating the magnetic field energy curve

for .1 mTorr in Figure 63. For this pressure, the field energy is decreasing slowly and appears to have been about 5 ergs at $t=0$. At that time the dimensions of the laser plasma were about $z=1$ mm and $r=1$ mm. Then the average field in this volume which would give a total energy of 5 ergs would be 200 Gauss. Assuming the temperature varies by no more than 2 eV in about 1 mm and $\delta \approx z=1$ mm, the approximated source term, Eqn. 56, predicts that this field could be generated in 10 nsec (i.e. within the laser pulse width). Hence, the source term can also account for the field generated in the laser plasma.

The three ambient pressures of nitrogen used for the mapping studies can be characterized by the magnitudes of the additional field initially generated in the density shell. For .1 mTorr, the extra field was negligible compared to the field generated in the front of the laser plasma. For 5 mTorr, it was comparable. For 250 mTorr, the extra field generated in the density shell is much larger than the field generated in the laser plasma.

The field enhancement with higher pressures cannot be due to any enhanced absorption of the laser energy caused by the presence of the background gas. This conclusion follows from Figure 7 which shows that doubling the incident laser power had less influence on the magnitude of the fields than increasing the ambient pressure from 1 mTorr to 200 mTorr. Since 90% of the laser power

was absorbed anyway, the absorption could not be enhanced by more than 10%.

C. SPATIAL AND TEMPORAL BEHAVIOR OF THE FIELDS

1. Low Ambient Pressures

For ambient pressures in the pressure-independent region of Figure 6 (pressures lower than 1 mTorr), the ambient plasma plays an insignificant role in the generation of the magnetic field. In this case, the spatial and temporal behavior of the field is governed primarily by the motion of the laser plasma. Thus, the two-dimensional contours for .1 mTorr of nitrogen can be analyzed by considering the motion of the laser plasma.

The field contours for .1 mTorr (see Figures 15 - 49) are more confined to the region near the z-axis than are those for the other pressures because the laser plasma expands primarily along the z-axis.

A possible explanation of the slow core of high field which does not propagate past 6 mm and the faster component of field which eventually distorts the contours can be obtained from laser plasma studies. It has been observed [Refs. 20 and 21] that when a laser plasma expands into a high vacuum, the plasma density profile has two components. These are a rapidly moving shell which does not recombine and a slowly moving core which recombines rapidly and never expands beyond about 1 cm. This two-component behavior of the laser plasma density seems to

agree with the two-component behavior of the field for .1 mTorr. Thus, the distortion of the field and the eventual formation of a field shell seem to be due to the convection of the field by the fast density shell of the laser plasma.

The field reversal detected at late times for .1 mTorr could only be the result of field generation. Examination of Eqn. 18 shows that axisymmetric field reversal can only occur if the source term is nonvanishing. The convection and the diffusion terms are both proportional to B . Since B must decrease through a magnitude of zero if it is to reverse direction, these terms would both vanish as the field decreased in magnitude to zero. The source term is needed to drive the fields in the reverse direction.

Since the fast density component of the laser plasma forms into a shell at late times, the density gradient behind the front will be in the $+z$ -direction. Since the temperature gradient is still in the $-r$ -direction, the source term of Eqn. 18 predicts that the field will be generated in the counterclockwise direction about the z -axis in Figure 1. This is opposite to its previous direction.

Because of the low ambient density in this case, the negligible interaction between the laser plasma and the ambient plasma cannot produce much heating. However, because of the low thermal conductivity of the laser

plasma, the radial temperature gradient produced during the laser heating will remain for a very long time; the relaxation time for temperature gradients was estimated to be about 10^{-4} sec for the laser plasma. Hence, field generation will be taking place at late times (600 nsec).

Besides the late-time field reversal, the observed decay time of the magnitude of the field also supports generation of magnetic field in the fast density shell. The diffusion time for the field for .1 mTorr was estimated to be the same as for 250 mTorr, 92 nsec. Figure 13 shows that between 40 nsec and 130 nsec, the magnitude of the field did decrease by $1/e$ (where e is the base for natural logarithms). Then during this period the field decreased with a characteristic time of 90 nsec for .1 mTorr. At times later than 140 nsec, Figure 13 shows that the magnitude of the field decreased with a longer characteristic time, and Figure 63 shows that the field energy remained about constant at these times for .1 mTorr. The conclusion appears to be that field generation was balancing field dissipation by diffusion at times later than about 140 nsec. Because of the low magnitude of the field for .1 mTorr, only about 4 Gauss would need to be generated in 100 nsec to account for the difference between the observed decay time of the field and the estimated field diffusion time of 92 nsec.

If the dimensions of the field shell are assumed to correspond to the fast density shell, the field contours can be used to allow an order of magnitude estimate of the source term to be made at these times. Figure 24 shows that at 180 nsec the dimensions of the field shell are about 8 mm in the z-direction and about 5 mm in the r-direction. Then the scale length for the axial density gradient of the shell (under the above assumption) would be about 4 mm and the scale length for the radial temperature gradient would be about 3 mm. Then the source term of 18 predicts that the required field of 4 Gauss in 100 nsec would be generated if the temperature of the density shell varied by only .04 eV in the radial direction, which seems quite reasonable. This field production which compensates for the field dissipation by diffusion is occurring in the front of the density shell (where the density gradient is in the -z-direction) while the reversed field is generated behind the density shell.

2. High Ambient Pressures

For high ambient pressures (>50 mTorr), the magnetic fields are initially larger than those for lower pressures but subsequently damp strongly with time and with distance. The fields decay at approximately exponential rates both in space (see Figure 9) and time (see Figure 14). The spatial decay rate increases with ambient pressure (see Figure 9).

The exponential decay with time indicates strong dissipation of the fields as they are convected by the expanding laser plasma. If the field is convected at a constant velocity, then the diffusion of the field can be studied most conveniently in the moving frame of the field. If diffusion dominates over field generation, then in the moving frame of the field, Eqn. 18 becomes

$$\frac{\partial \vec{B}}{\partial t} = \frac{1}{\mu_0 \sigma} \nabla^2 \vec{B} \quad . \quad (20)$$

The field initially has a roughly Gaussian spatial profile as Figure 50 shows for 250 mTorr. Equation 20 can then be used to describe the decay of the maximum of the field profile as it is convected. At the position of the maximum of a Gaussian profile, Eqn. 20 becomes

$$\frac{\partial B}{\partial t} = - \frac{1}{\mu_0 \sigma L^2} B \quad . \quad (58)$$

Both σ and L are functions of time; σ decreases, and L increases. Figure 14 shows that they change in such a way that the diffusion time

$$\tau_m = \mu_0 \sigma L^2 \quad (21)$$

remains constant for 250 mTorr from about 60 nsec until 300 nsec. Then the maximum field in the moving frame varies as

$$B(t) = B_0 e^{-t/\tau_m} \quad . \quad (59)$$

This behavior of the field for 250 mTorr is displayed in Figure 14 which also indicates that τ_m is 92 nsec.

Diffusion of the field dominates over field generation because for high ambient pressures τ_m is much shorter than the characteristic time for field generation. This is because the strongest fields were produced in the density shell at the front of the expanding laser plasma for pressures higher than 50 mTorr. The characteristic lengths for these fields were the widths of the density shells which were much smaller than the dimension of the laser plasma. Since σ is independent of density, then the diffusion time as given by Eqn. 21 is much shorter for fields produced primarily in the density shell.

The exponential decay of the fields with time in the moving frame of the field will result in an exponential decrease in space in the lab reference frame. If the field is being convected at a constant velocity, then at the time t , the field maximum is at the position $z=vt$. Then Eqn. 59 becomes

$$B(z) = B_0 e^{-z/v\tau_m} . \quad (60)$$

The reason that the fields decay faster spatially for higher ambient pressures (see Figure 9) is partly due to the fact that for such high pressures, the laser plasma expansion velocity decreases with ambient pressure. This results because the mass of the density shell formed

at the front of the laser plasma is large enough to affect the dynamics of the laser plasma. Dean [Ref. 11] found that at early times

$$V \propto P^{-1/3} \quad (61)$$

where P is the ambient pressure, for pressures above about 25 mTorr. Then the scale length for the decay of the fields scales as

$$\lambda \propto P^{-1/3} \tau_m \quad (62)$$

Figure 9 shows that

$$\lambda \propto P^{-.31} \quad (32)$$

Apparently τ_m is independent of ambient pressure for this range of pressures.

The reason that the maximum field for 250 mTorr is initially ahead of the maximum fields for the lower pressures (see Figures 17 - 22) is that the field for 250 mTorr was generated primarily in the density shell at the front of the laser plasma while the fields for the lower pressures were generated further back in the laser plasma front. The laser plasma was expanding at a lower velocity for 250 mTorr (6.5×10^6 cm/sec versus 10^7 cm/sec) so that eventually the field maxima for the lower pressures overtook that for 250 mTorr (see Figure 24).

The rapid diffusion of the fields for 250 mTorr gave them a broader extent in the radial direction than the fields for .1 mTorr have (see Figure 22). The faster expansion velocity of the laser plasma for .1 mTorr compensates for the faster diffusion for 250 mTorr in the z-direction (see Figure 22).

The serious field distortions which become apparent by 260 nsec for 250 mTorr (see Figure 28) may be the result of a collisional interaction between the laser plasma and the ambient plasma. This was the interpretation given to similar distortions in the interaction front which were observed by Dean [Ref. 11] for high ambient pressures. A collisional interaction cannot take place until the laser plasma dimension has become larger than the mean free path for binary collisions (~ 1 cm). When the laser plasma has expanded to that extent, the collisional interaction becomes important and causes heating in the front of the laser plasma. Thus, radial temperature gradients arise, and field production again becomes strong.

The heating takes place within the density shell, including the region behind the shell where the density gradient is in the +z-direction. Hence, as discussed previously, the fields which are generated will be in the reverse direction from the fields generated initially.

The fact that the appearance of reversed fields indicates that field production is occurring is clearly

backed by Figure 63. During the period from 360 nsec until about 600 nsec, the field energy for 250 mTorr increased by an order of magnitude. During this same period, the reversed fields have increased in magnitude to about 10 Gauss (see Figures 33 - 38).

3. Intermediate Ambient Pressures

The magnetic fields for an ambient pressure of 5 mTorr display many of the characteristics of the fields for .1 mTorr. As in the .1 mTorr case, there was a core of high field which did not propagate out beyond about 5 mm and a fast shell of field which separated from the core of high field. The field contours for 5 mTorr have shapes near the z-axis which are similar to those for .1 mTorr (see Figures 19 - 25). The field generated inside the laser plasma for 5 mTorr remained distinct from the field generated in the density shell because of the relatively long diffusion time for the field in the laser plasma. Finally, at about 260 nsec, the fields in the two regions diffuse into each other, and the field in the laser plasma near the z-axis no longer resembled that for .1 mTorr (see Figure 28).

The field generated in the density shell rapidly diffused into the ambient plasma due to the shorter diffusion time for the ambient plasma. This diffusion gave the field for 5 mTorr a broader spatial extent than the fields for .1 mTorr had. Because the laser plasma expanded

at a higher velocity for 5 mTorr than for 250 mTorr, the fields for 5 mTorr had a broader extent in the ambient plasma at each instant of time.

Strong field production continued after laser shut-off in the 5 mTorr case, as Figure 63 shows. The location of the field generation appears to be in the region of the distortion of the 20 Gauss contour which was located at $z=1$ cm, $r=6$ mm at 60 nsec (see Figure 18). Comparison of the contours for .1 mTorr and for 5 mTorr indicates that the field distortion was at the laser plasma front where the density shell would be. The field contours at larger distances were not distorted because they were in the ambient plasma and not near the region where field generation was occurring in the density shell.

Field generation does not occur uniformly throughout the density shell. It occurred at the highest rate where the radial temperature gradient was largest, near the sides of the laser plasma as was illustrated in the example in Section IIC. This resulted in the distortion of the field. At later times, diffusion of the field caused the distortion to relax.

As the laser plasma expanded, its density steadily dropped until at late times only the density shell at the front was left. The observed shell of field seems to be associated with this density shell. The shell structure of the field became apparent at about 340 nsec (see Figure

32). The density gradient behind the density shell is in the $+z$ -direction so that at late times, the field reverses near the target (see Figure 46).

X. CONCLUSION

This thesis has presented a sizable body of data concerning the self-generated magnetic fields. Some of the parameters which govern the fields have been investigated as well as the spatial and temporal behavior of the fields.

The experimental results have been analyzed by applying Eqn. 18 in a more or less qualitative fashion. This approach has succeeded in showing that the theory presented here is a plausible explanation of the fields. However, the theory was not made quantitative enough for a thorough comparison with experimental results.

Also, much of the analysis of these results depended on utilizing data published in other studies. In particular, there was heavy reliance on Dean's results [Ref. 11] for the interaction between two counterstreaming plasmas. This approach was necessitated by the lack of time and means to perform the needed measurements in this experiment. Such heavy reliance on the results of other studies is certainly not desirable.

Thus, in order to further develop the knowledge of the self-generated magnetic field, work must be done in two areas. First, the theory must be developed further in order that it can make quantitative predictions of the

fields. Because of the complexity of the situation, this will undoubtedly require a computer simulation of the problem. Secondly, the other parameters of this experiment need to be measured. Most importantly, the relationship of the magnetic field to the laser plasma density and to the ambient plasma density must be thoroughly studied. Only when more progress has been made in these two areas can the fields be thoroughly understood.

APPENDIX A

Equation 17 is

$$\frac{\partial \vec{B}}{\partial t} = \vec{V}_x (\vec{V}_e \times \vec{B}) - \frac{1}{\sigma} \vec{V}_x j + \vec{V}_x \frac{1}{n_e e} \vec{V}_P. \quad (17a)$$

The importance of the displacement current in Maxwell's equation

$$\vec{V}_x \vec{B} = \mu_0 \vec{j} + \frac{1}{c^2} \frac{\partial \vec{E}}{\partial t} \quad (17b)$$

can be evaluated by dimensional analysis. The ratio of the two terms on the right hand side of Eqn. 17b becomes

$$\frac{\frac{1}{c^2} \frac{\partial \vec{E}}{\partial t}}{\mu_0 \vec{j}} \approx \frac{\frac{1}{c^2} \frac{E}{\tau}}{\mu_0 \sigma E} = \frac{\epsilon_0}{\sigma \tau} \quad (17c)$$

where τ is some characteristic time for the plasma. Now for all situations of interest $\sigma > 1$, so that Eqn. 17c becomes

$$\frac{\epsilon_0}{\sigma \tau} < \frac{\epsilon_0}{\tau} < \frac{10^{-11}}{\tau} \quad (17d)$$

The duration of the laser pulse provides a reasonable measure for the smallest characteristic time for the laser plasma and is of the order of 10^{-8} sec. Then Eqn. 17d shows that

$$\frac{\frac{1}{c^2} \frac{\partial \vec{E}}{\partial t}}{\mu_0 \vec{j}} \ll 1 \quad (17e)$$

for this problem. Then Eqn. 17b becomes

$$\vec{\nabla} \times \vec{B} = \mu_0 \vec{J} \quad (17f)$$

Using Eqn. 17f the second term in Eqn. 17a becomes

$$\begin{aligned} -\frac{1}{\sigma} \vec{\nabla} \times \vec{J} &= -\frac{1}{\mu_0 \sigma} \vec{\nabla} \times (\vec{\nabla} \times \vec{B}) \\ &= -\frac{1}{\mu_0 \sigma} [\vec{\nabla} (\vec{\nabla} \cdot \vec{B}) - \nabla^2 \vec{B}] \\ &= \frac{1}{\mu_0 \sigma} \nabla^2 \vec{B} \end{aligned} \quad (17g)$$

The third term in Eqn. 17a becomes

$$\begin{aligned} \vec{\nabla} \times \frac{1}{n_e e} \vec{\nabla} P_e &= \vec{\nabla} \times \frac{kT_e}{eP_e} \vec{\nabla} P_e \\ &= \vec{\nabla} \left(\frac{kT_e}{eP_e} \right) \times \vec{\nabla} P_e \end{aligned}$$

since $\vec{\nabla} \times \vec{\nabla} P_e = 0$

Then

$$\vec{\nabla} \times \frac{1}{n_e e} \vec{\nabla} P_e = \frac{k}{eP_e} \vec{\nabla} T_e \times \vec{\nabla} P_e \quad (17h)$$

since $\vec{\nabla} \left(\frac{1}{P_e} \right) \times \vec{\nabla} P_e = 0$.

Equation 17h can also be written

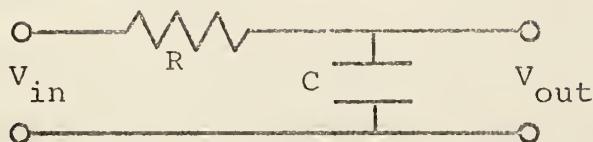
$$\begin{aligned} \vec{\nabla} \times \frac{1}{n_e e} \vec{\nabla} P_e &= \frac{k}{en_e kT_e} \vec{\nabla} T_e \times \vec{\nabla} (n_e kT_e) \\ &= \frac{k}{en_e} \vec{\nabla} T_e \times \vec{\nabla} n_e \end{aligned} \quad (17i)$$

Hence, Eqn. 17a becomes

$$\frac{\partial \vec{B}}{\partial t} = \vec{\nabla} \times (\vec{\nabla} \times \vec{B}) + \frac{1}{\mu_0 \sigma} \nabla^2 \vec{B} + \frac{k}{en_e} \vec{\nabla} T_e \times \vec{\nabla} n_e \quad (17j)$$

APPENDIX B

The circuit for an RC integrator is:



By simple circuit analysis,

$$V_{out} = \frac{V_{in}}{2\pi fRC + 1} \quad (29a)$$

If $2\pi fRC \gg 1$, then Eqn. 29a becomes

$$V_{out} = \frac{1}{2\pi fRC} V_{in} \quad (29b)$$

Now the input signal is

$$V_{in} = \tilde{V}_{in} e^{i2\pi ft} \quad (29c)$$

so that

$$|\int V_{in} dt| = \frac{V_{in}}{2\pi f} \quad (29d)$$

Thus, Eqn. 29b can be rewritten

$$V_{out} = \frac{1}{RC} \int V_{in} dt \quad (29e)$$

Here the input signal is from a magnetic probe, so that from Eqn. 28

$$\int V_{in} dt = nAB \quad (29f)$$

Then, Eqn. 29e becomes

$$V_{\text{out}} = \frac{nA}{RC}B \quad (29g)$$

if $2\pi fRC \gg 1$.

The lowest frequency f_0 for which Eqn. 29g is generally considered valid is such that $2\pi f_0 RC = 10$. Then Eqn. 29g can be applied to any signal whose Fourier composition contains a fundamental frequency no lower than f_0 defined above.

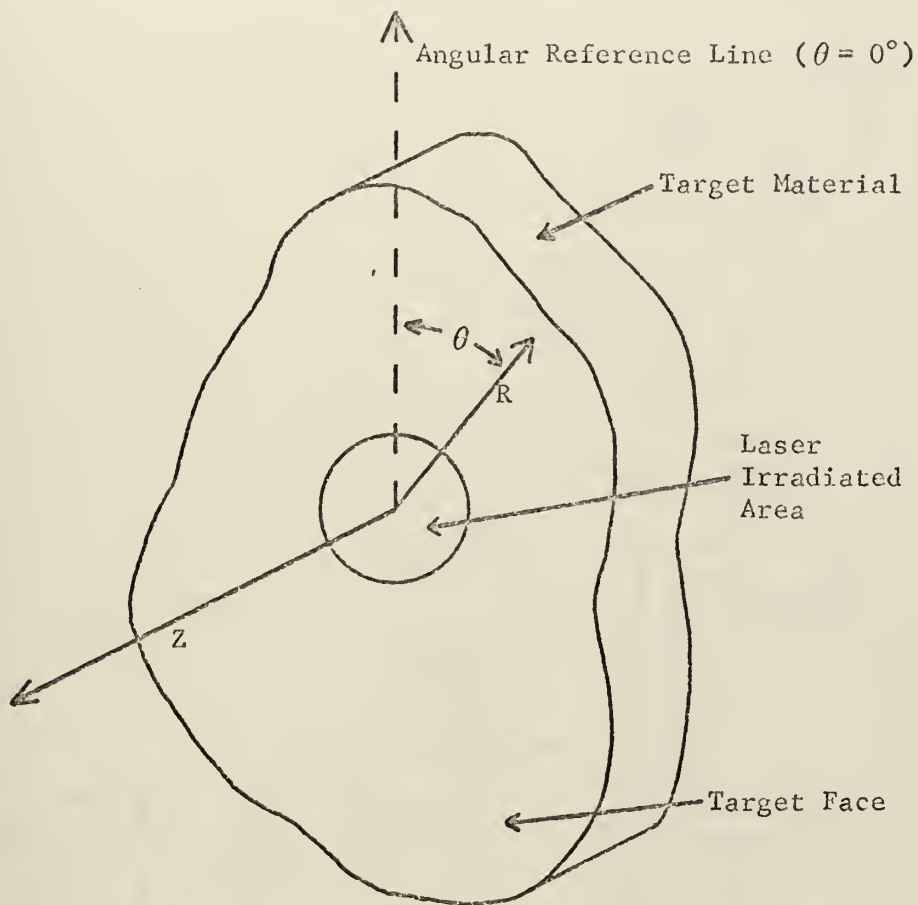


Figure 1. Cylindrical polar coordinate system used.

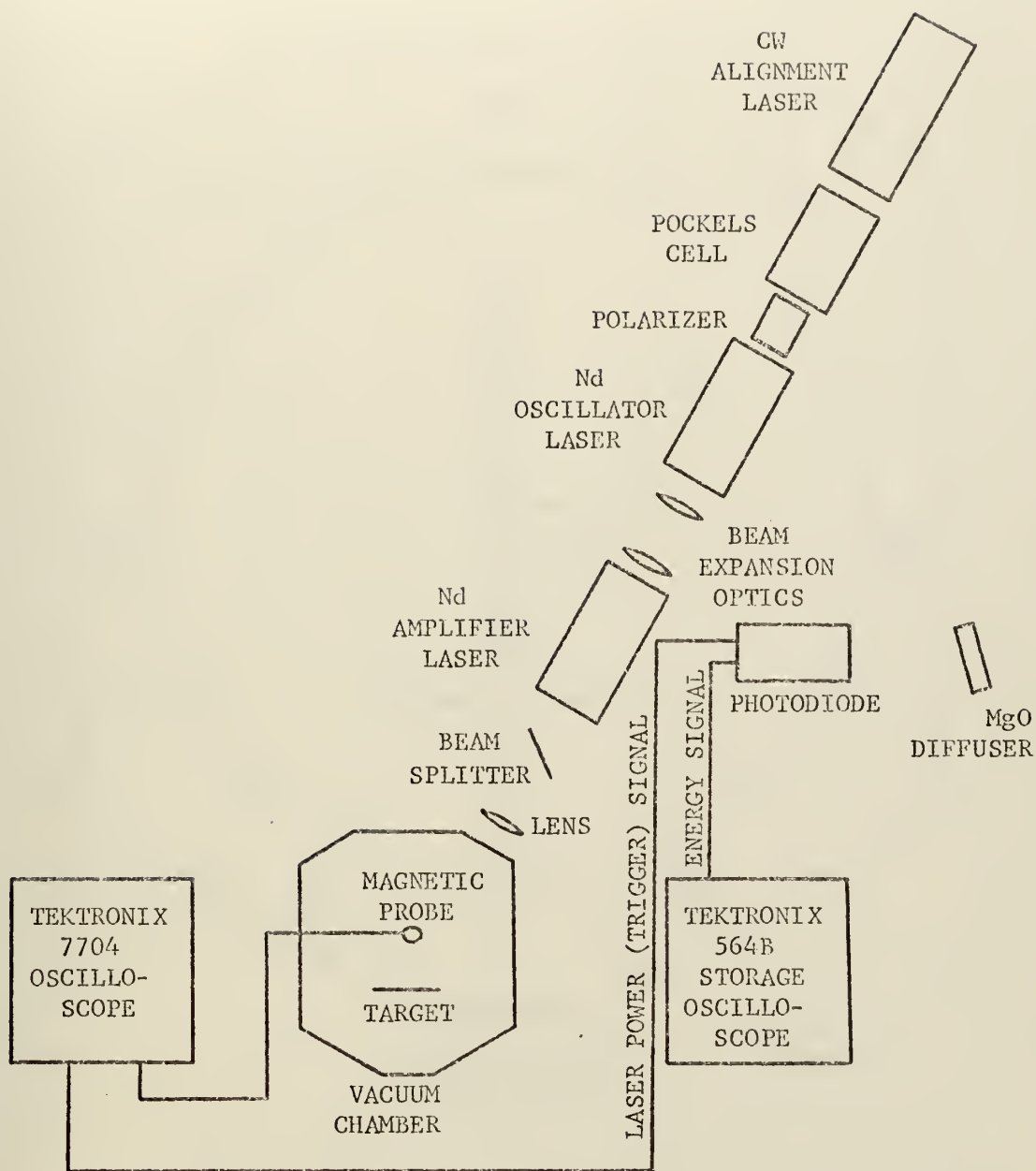


Figure 2. Block diagram of experimental layout.

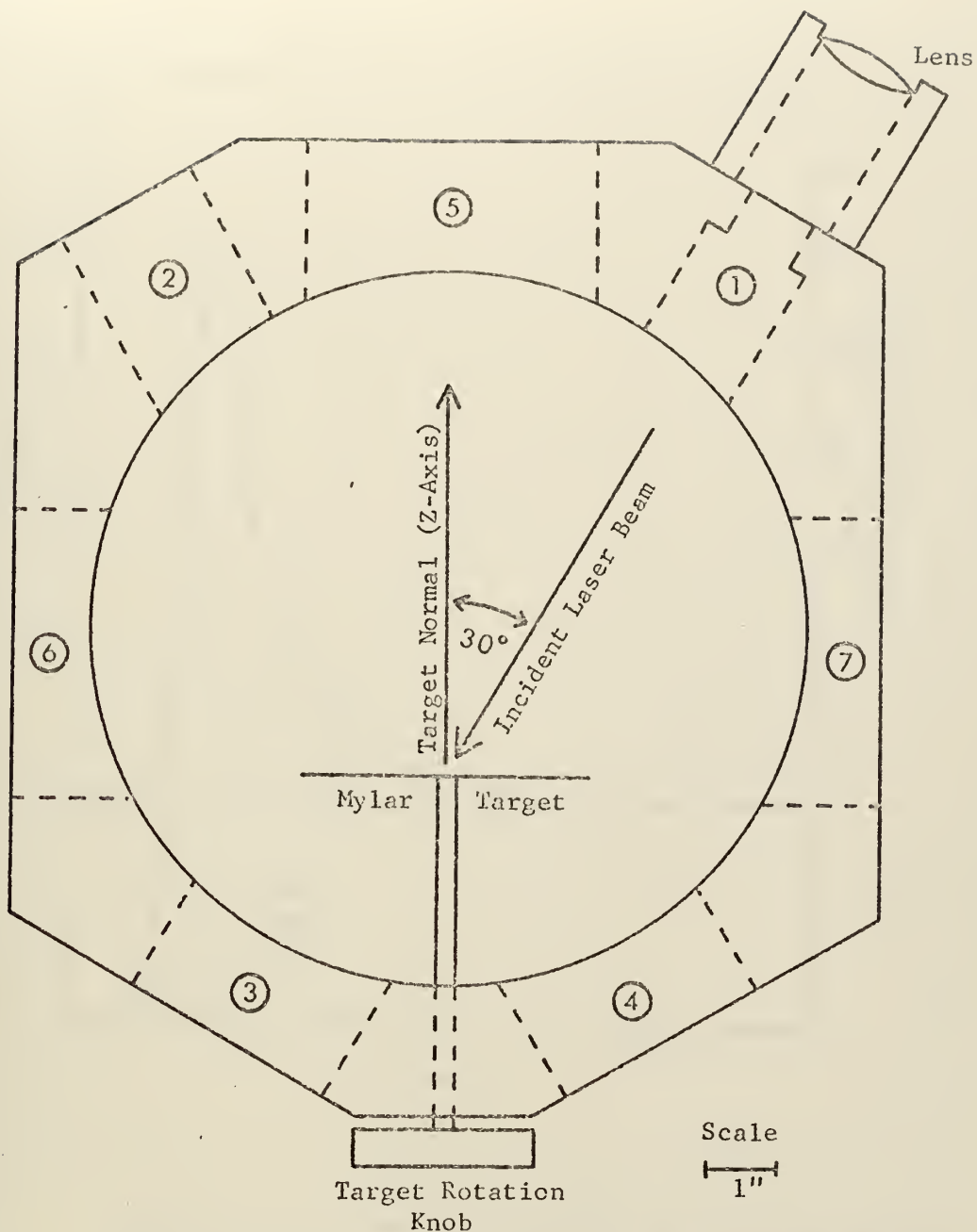


Figure 3. Top view of vacuum chamber. Port #1 is the laser beam entry port, #2 is the reflected laser beam observation port, #3 is the transmitted laser beam observation port, #4 is an optical observation port, #5 is the forward optical/probe observation port, and #6 and #7 are the side optical/probe observation ports.

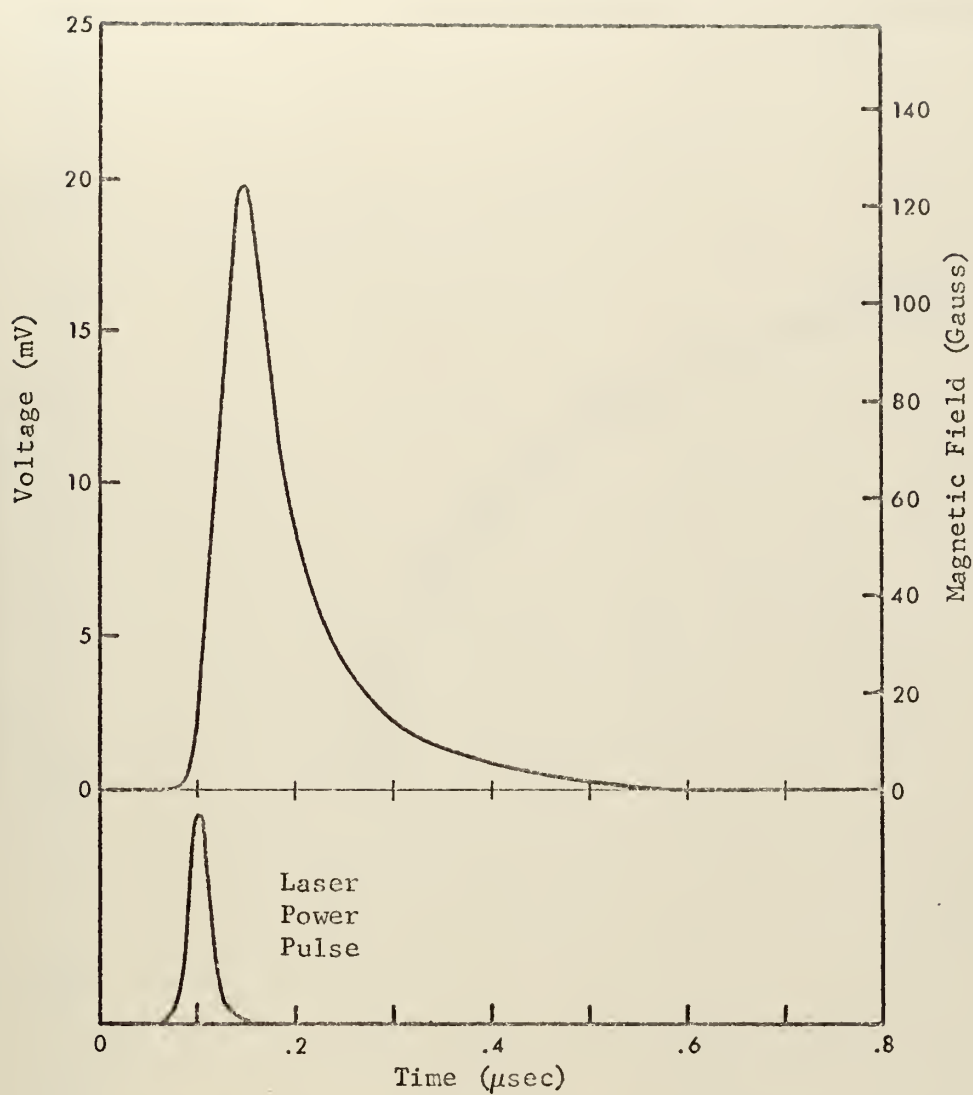


Figure 4. Magnetic probe signal representing the azimuthal magnetic field detected at $z=r=4$ mm, $\theta=0^\circ$, for a nitrogen background gas pressure of 250 mTorr. The laser power pulse is displayed for reference.

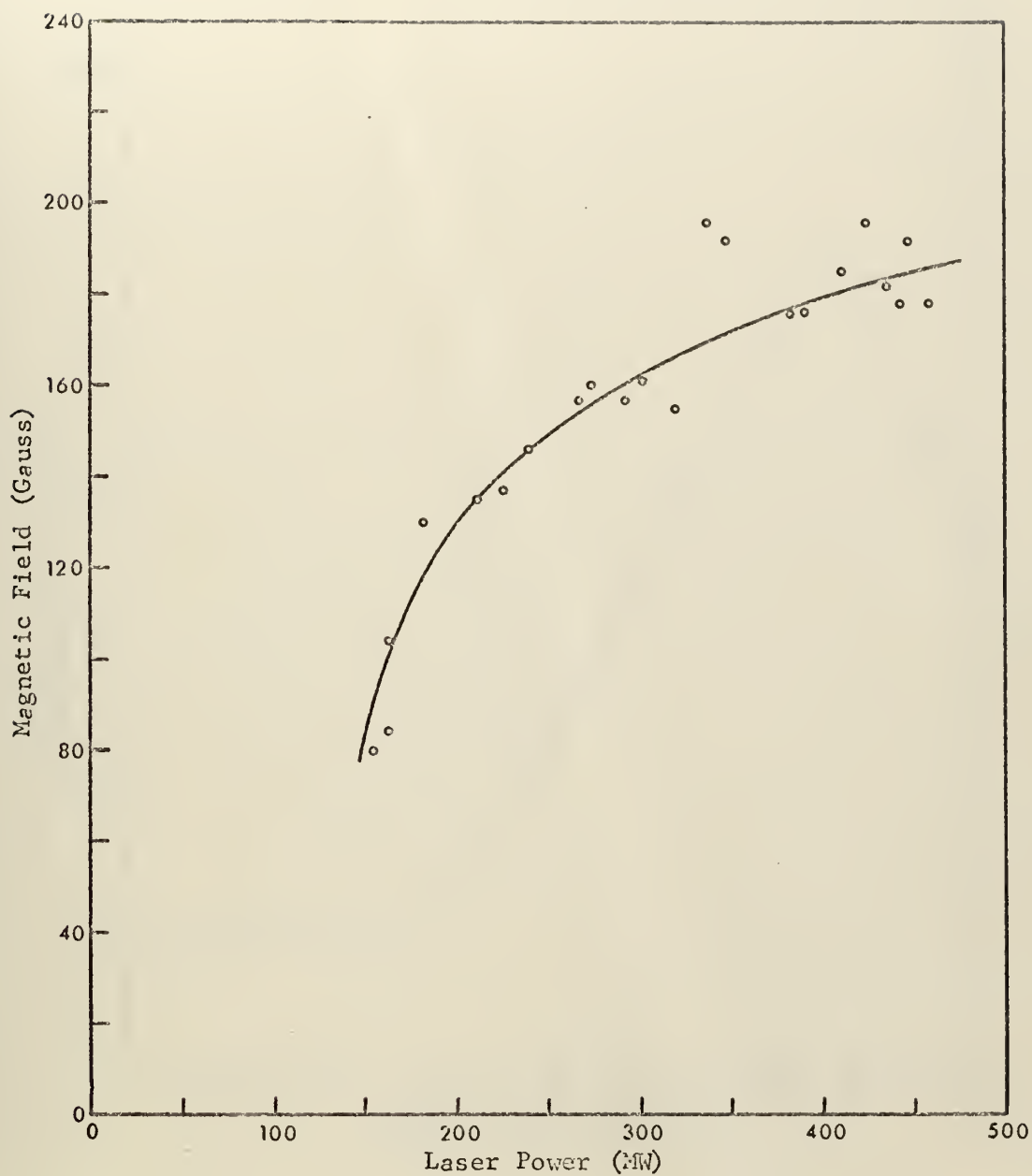


Figure 5. Maximum azimuthal magnetic field at $z=4$ mm, $r=3$ mm, $\theta=0^\circ$, as a function of laser power incident on a .005 in. Mylar foil in a background gas pressure of 25 mTorr of nitrogen.

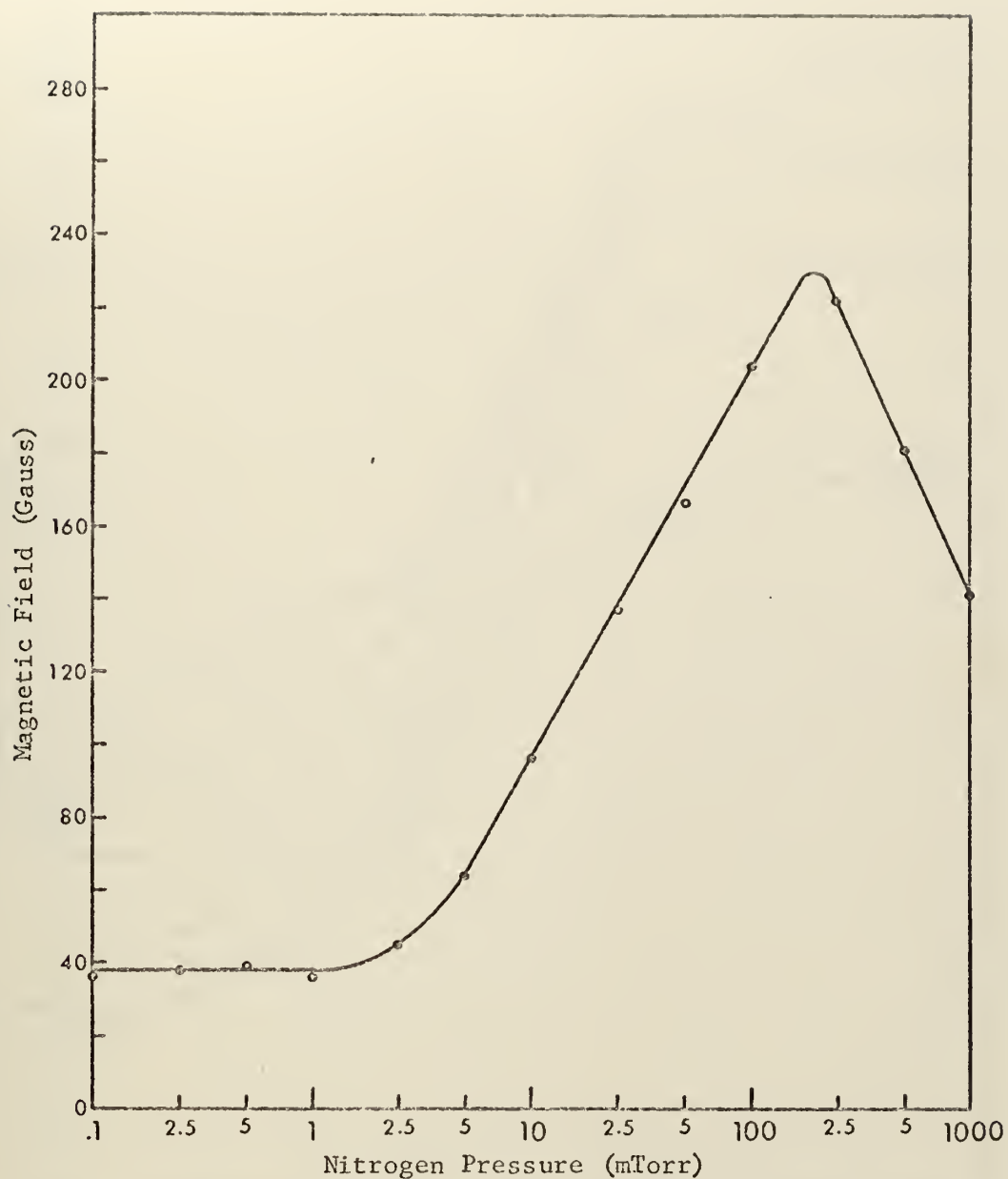


Figure 6. Maximum azimuthal magnetic field at $z=4$ mm, $r=3$ mm, $\theta=0^\circ$, as a function of nitrogen background pressure for an incident laser power of 300 MW.

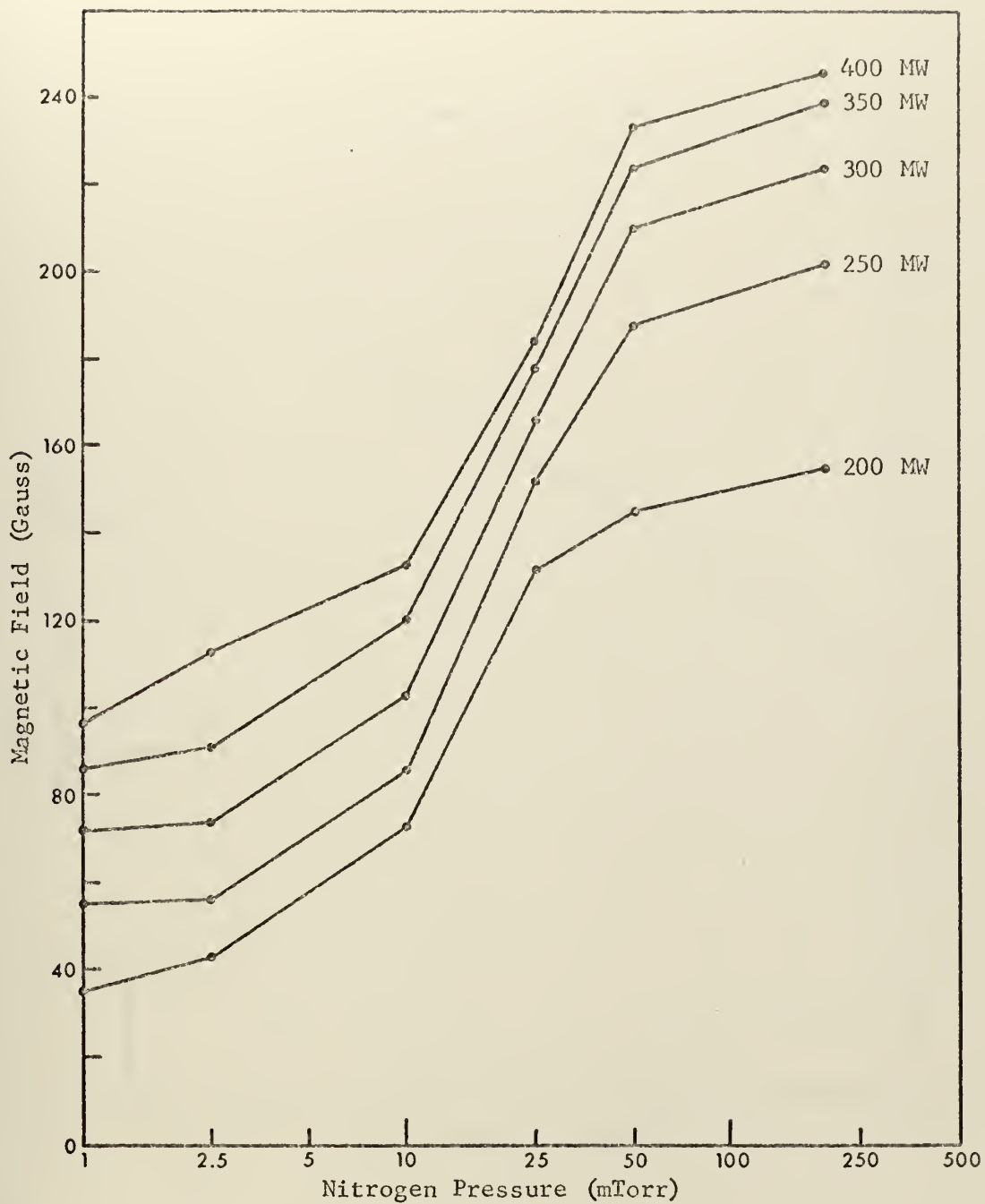


Figure 7. Maximum azimuthal magnetic field at $z=4$ mm, $r=3$ mm, $\theta=0^\circ$, as a function of nitrogen background pressure for a given laser power incident on a .005 in. Mylar foil.

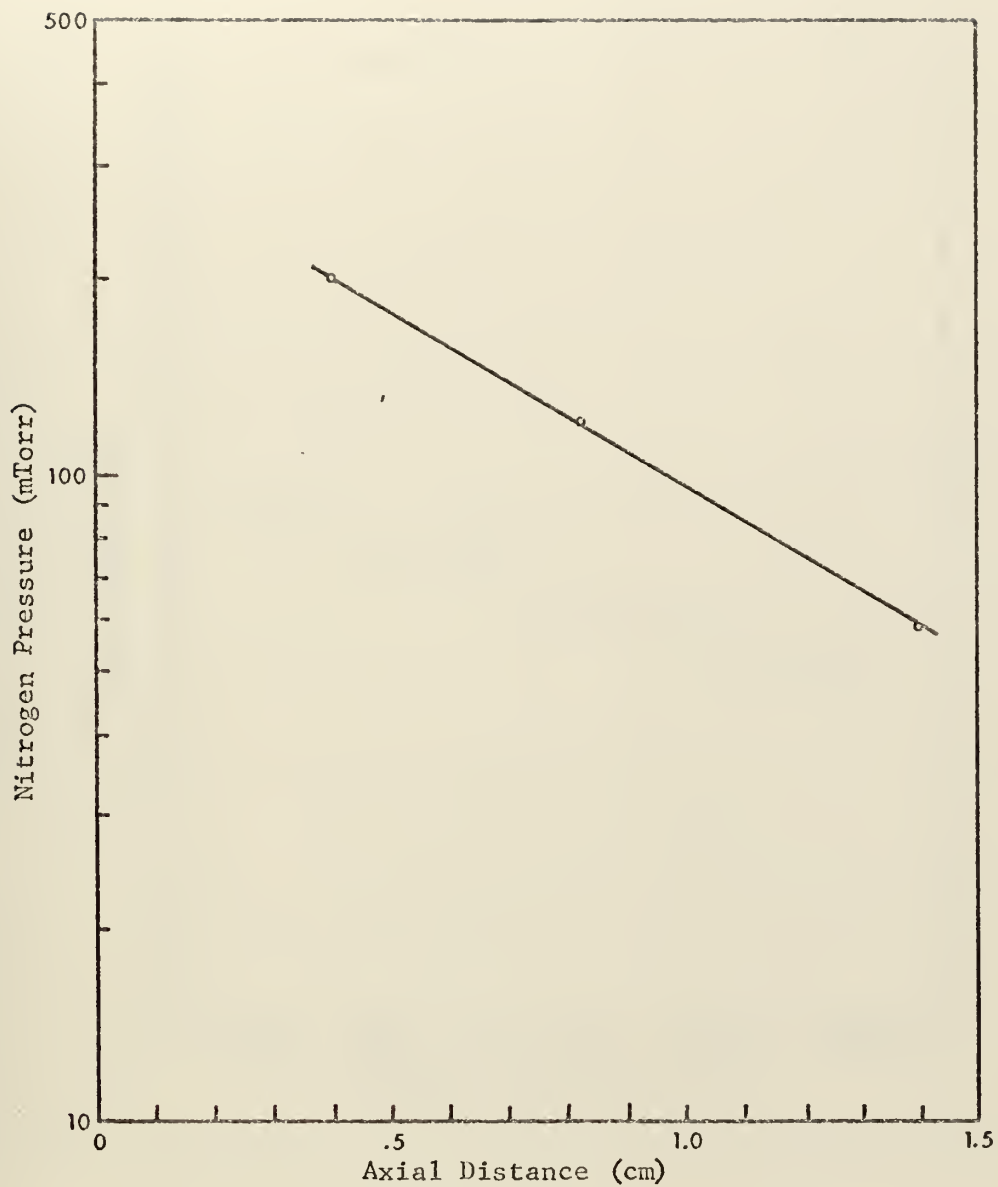


Figure 8. Nitrogen background gas pressure at which the azimuthal magnetic field at a fixed axial position attains its largest value as a function of the axial distance of that position along $r=3$ mm, $\theta=0^\circ$.

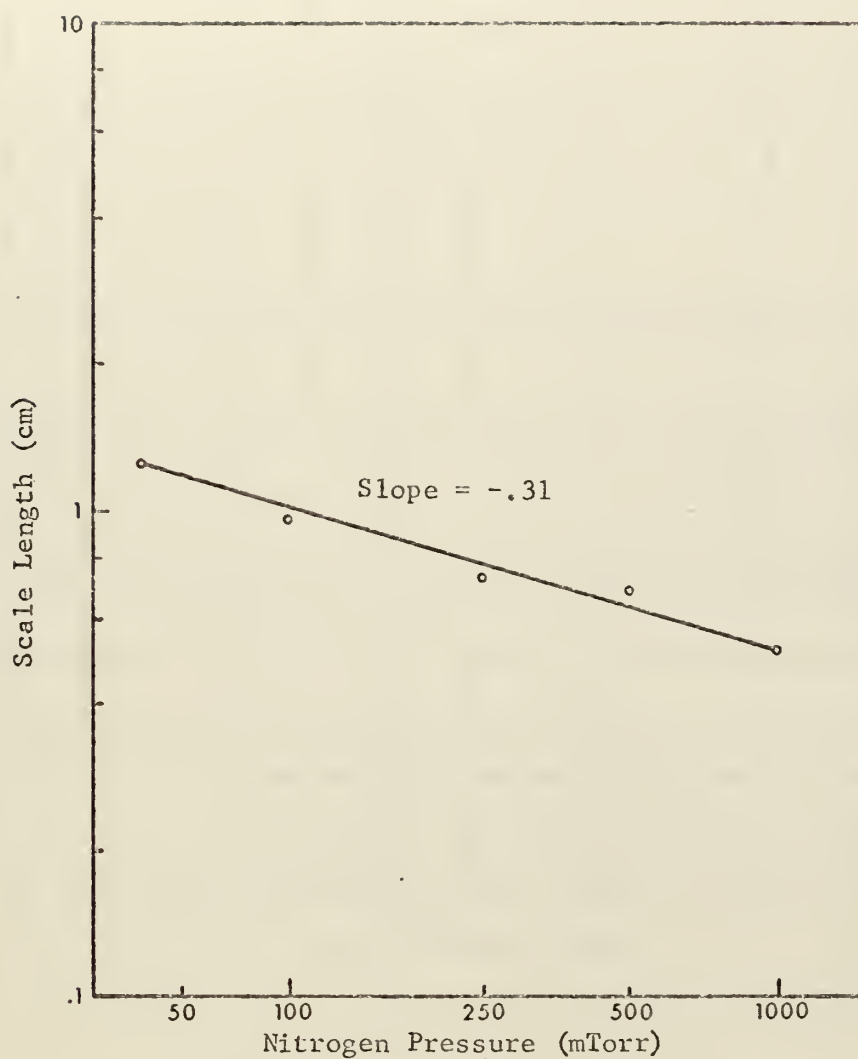


Figure 9. Scale length for the exponential decrease of the maximum azimuthal magnetic field with increasing axial distance along $r=3$ mm, $\theta=0^\circ$, as a function of background pressure of nitrogen gas.

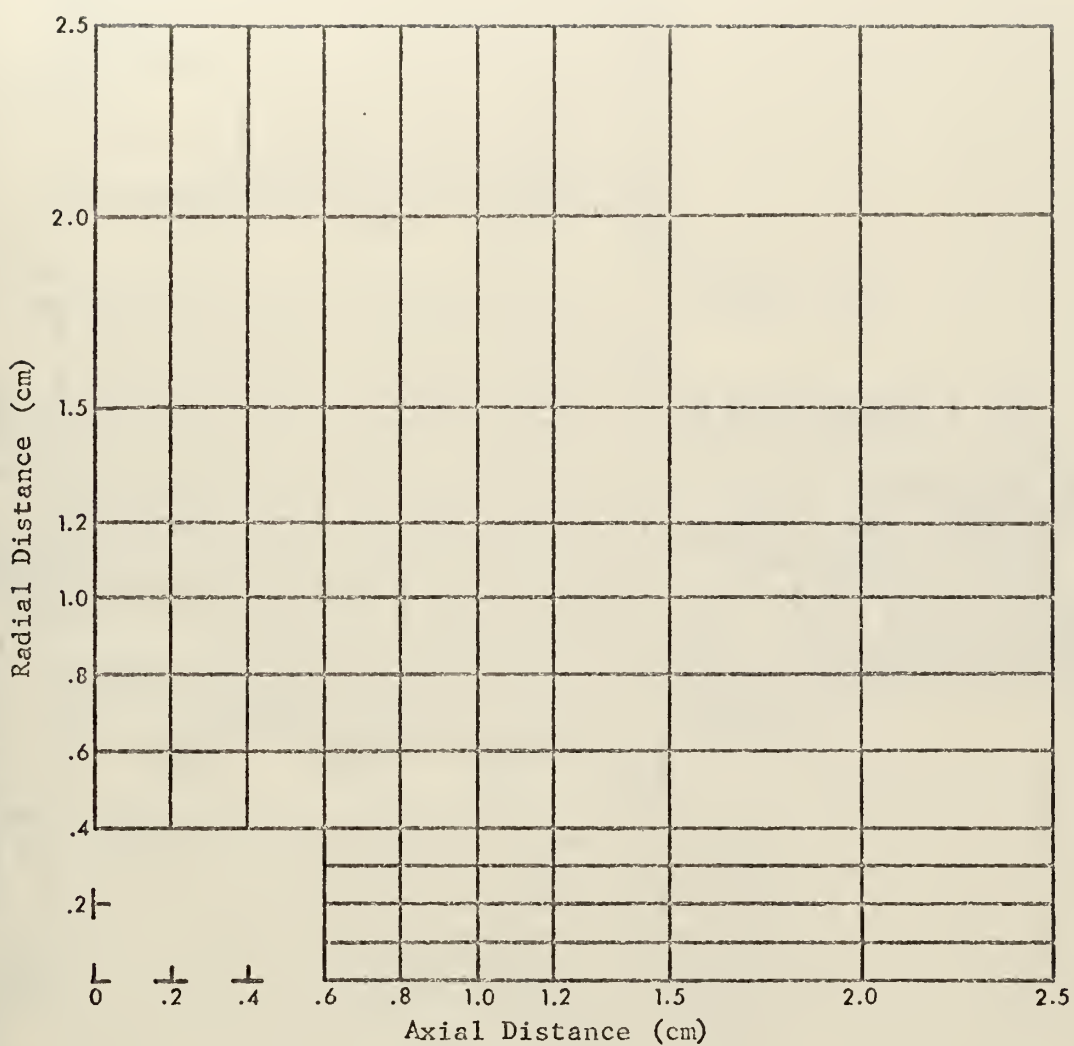


Figure 10. Magnetic field mapping grid in the $\theta=0^\circ$ plane. Probe measurements of the field were taken at each intersection point of the grid lines.

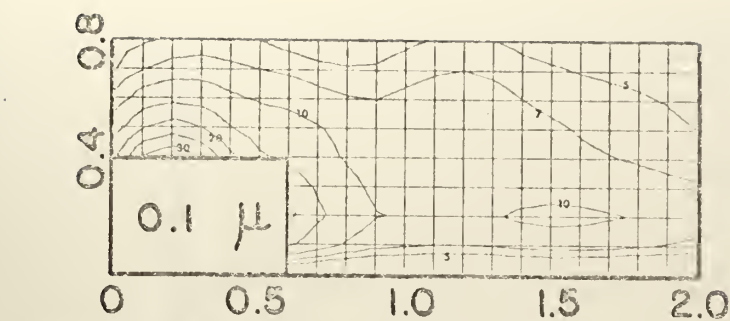
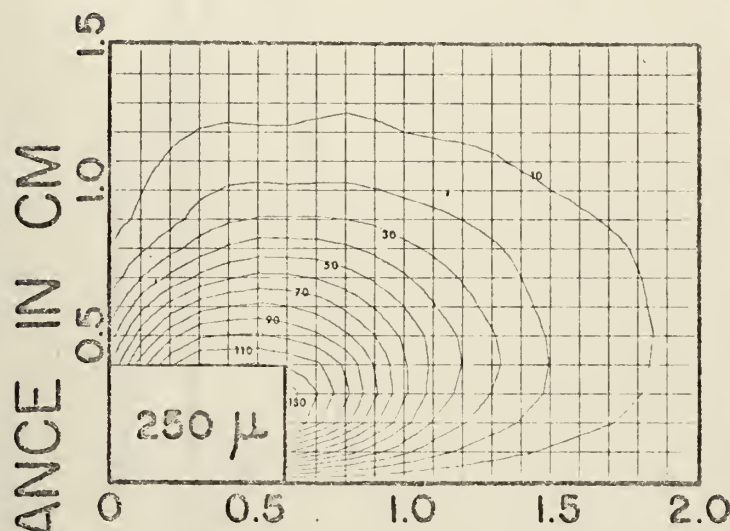
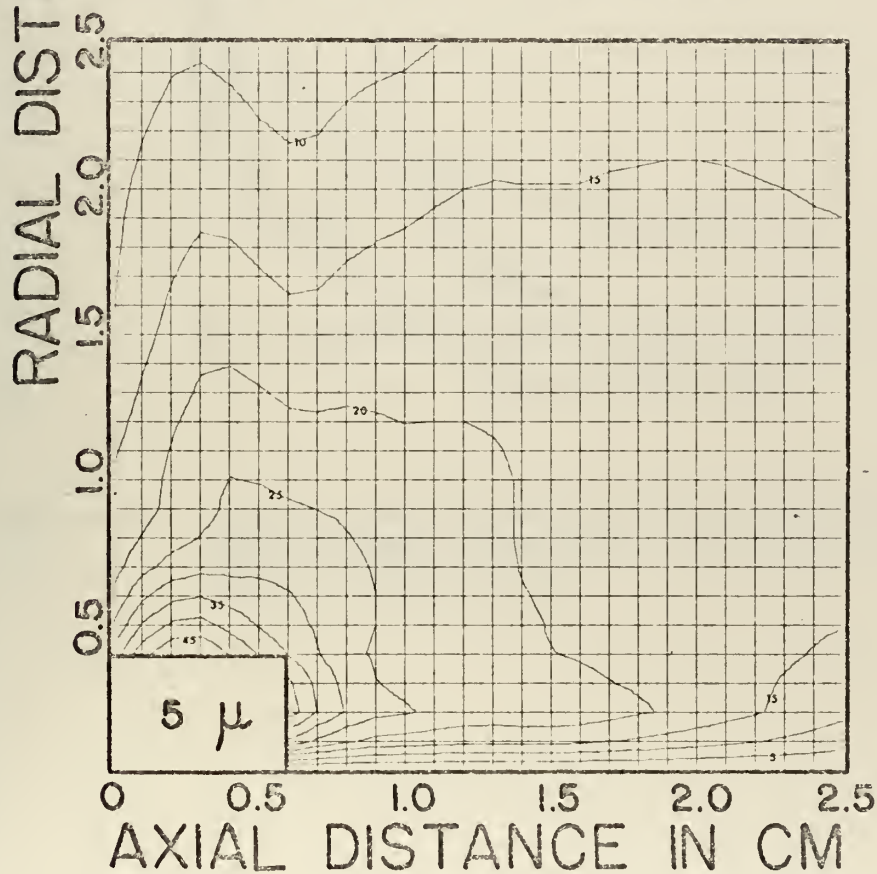


FIG. II



MAXIMUM B_0
FOR VARIOUS
PRESSURES
OF NITROGEN
BACKGROUND
GAS.



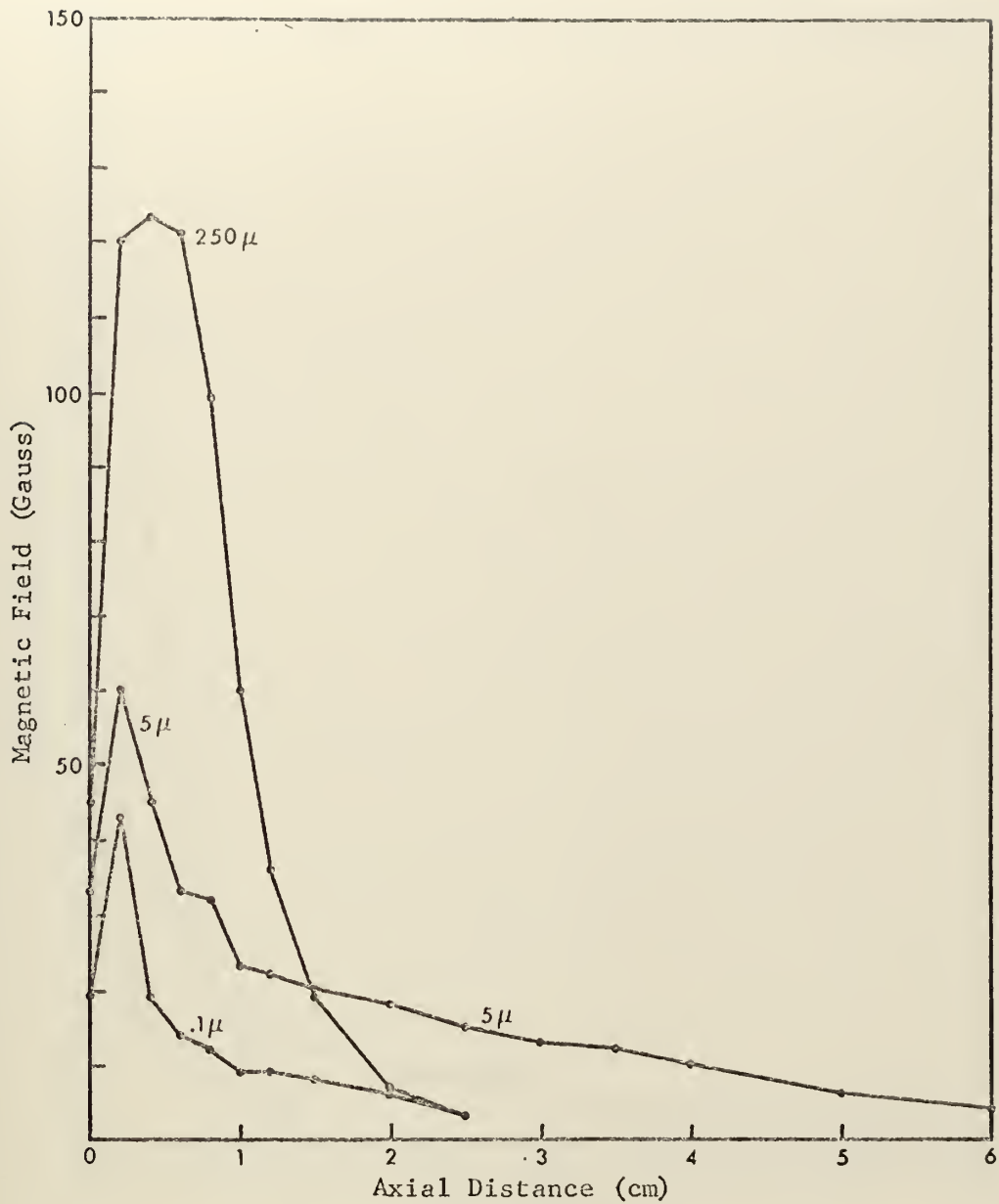


Figure 12. Maximum azimuthal magnetic field as a function of axial distance along $r=4$ mm, $\theta=0^\circ$, for various pressures of nitrogen background gas.

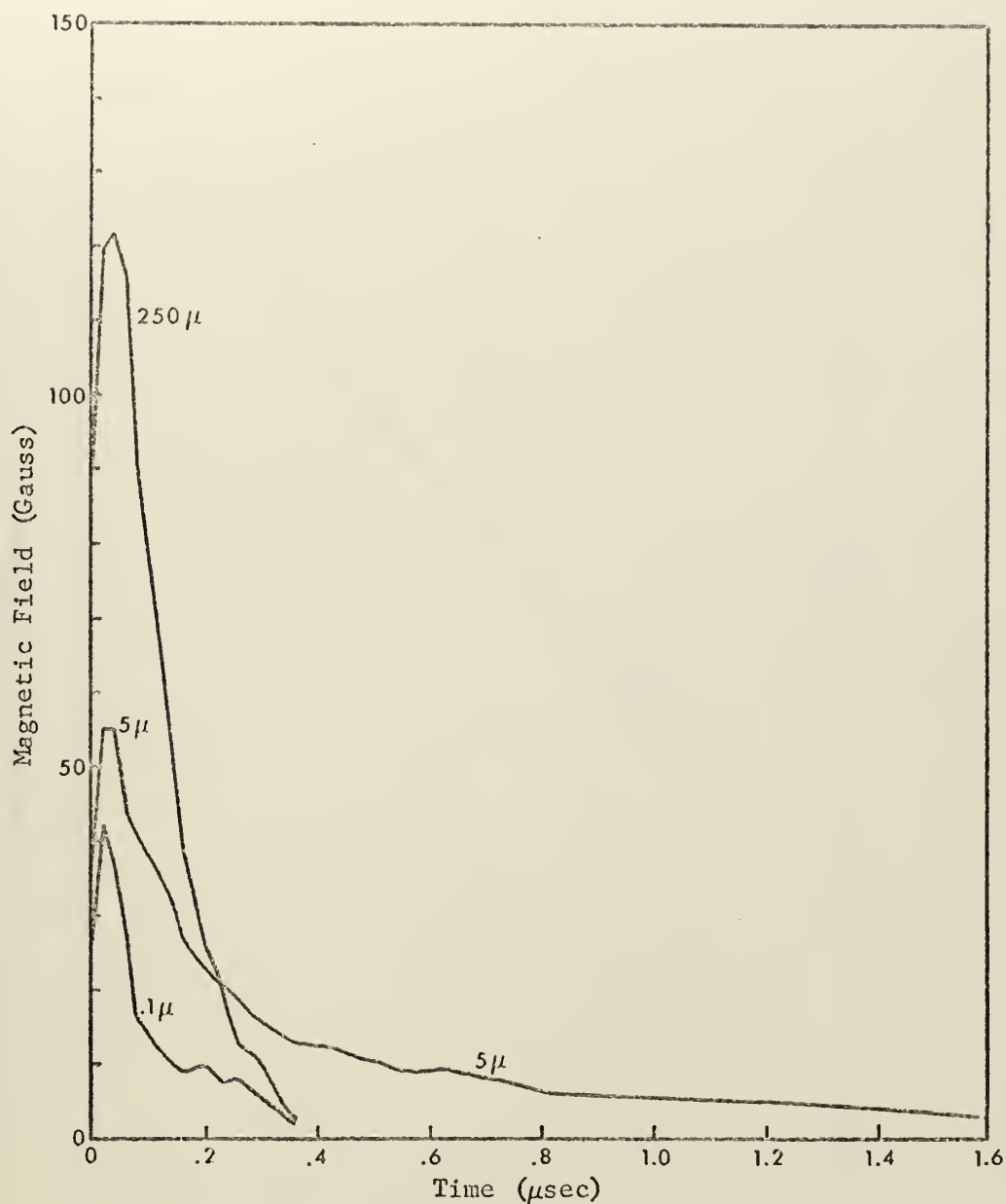


Figure 13. Maximum azimuthal magnetic field along $r=4$ mm, $\theta=0^\circ$, as a function of time, for various pressures of nitrogen background gas.

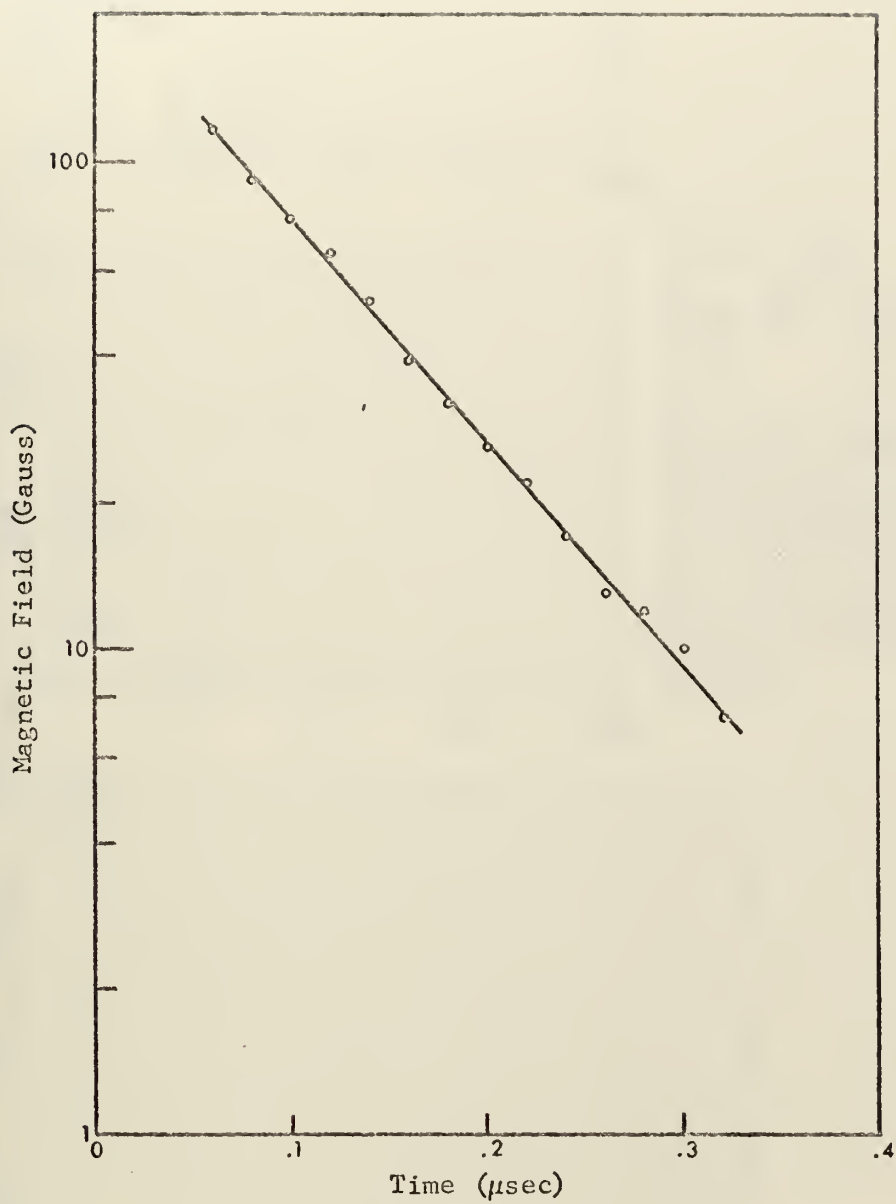


Figure 14. Maximum azimuthal magnetic field along $r=4$ mm, $\theta=0^\circ$, as a function of time, for 250 mTorr of nitrogen background gas.

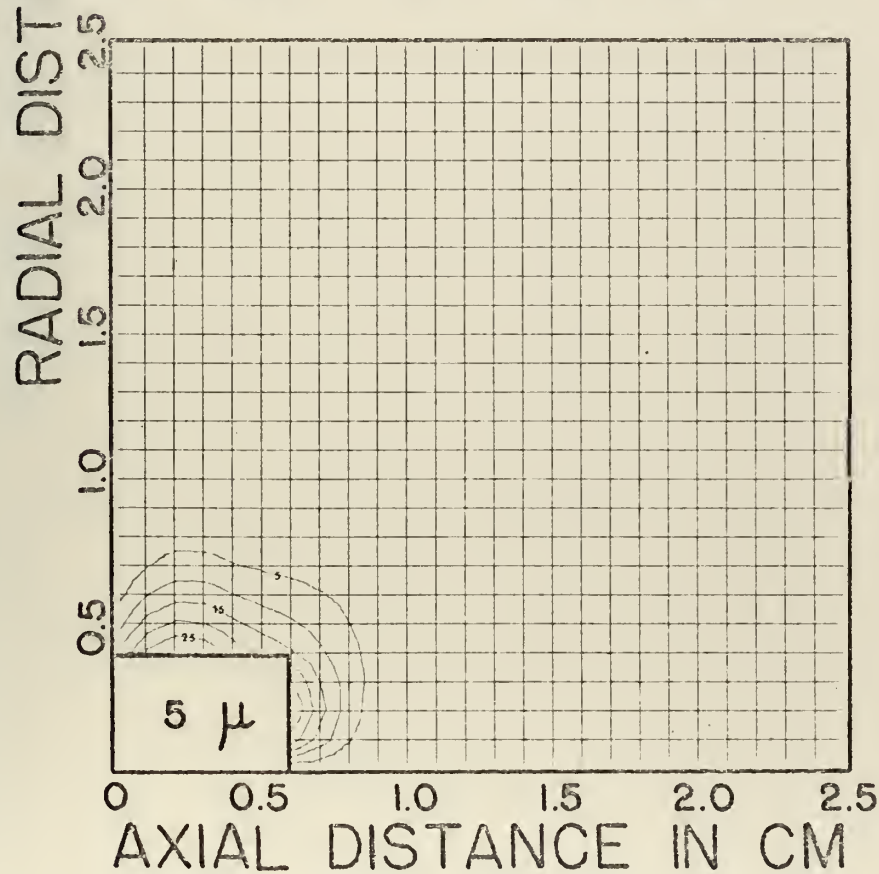
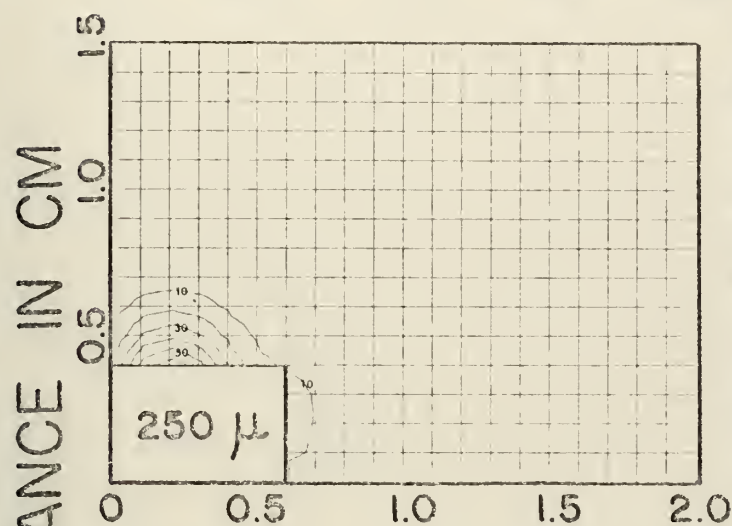
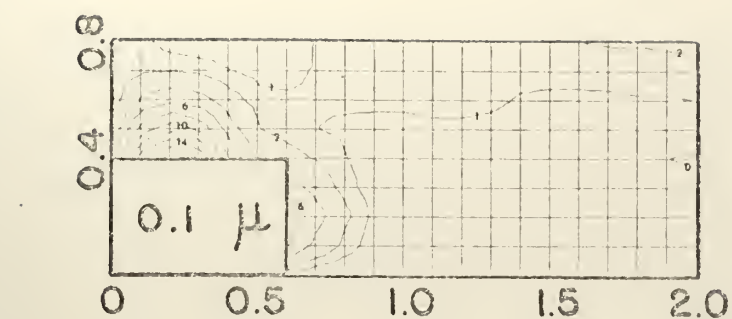


FIG. 15
 B_0 IN GAUSS
 AT 0 NSEC
 FOR VARIOUS
 PRESSURES
 OF NITROGEN
 BACKGROUND
 GAS.

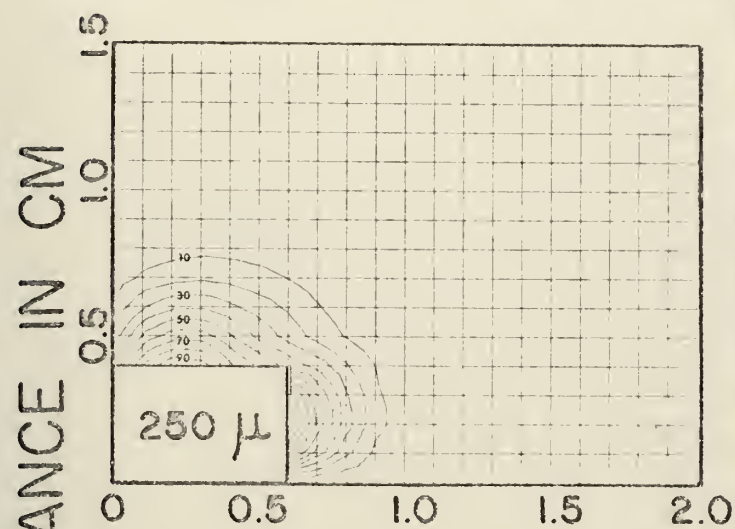
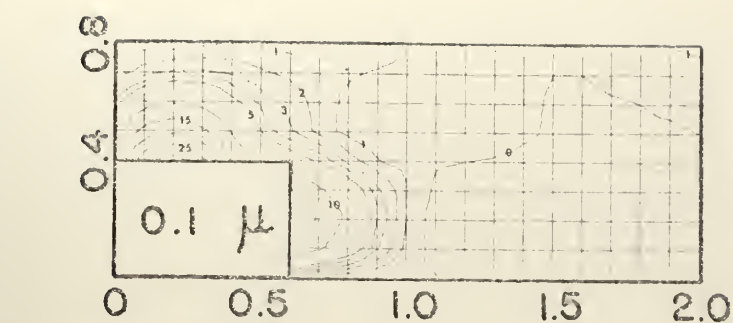
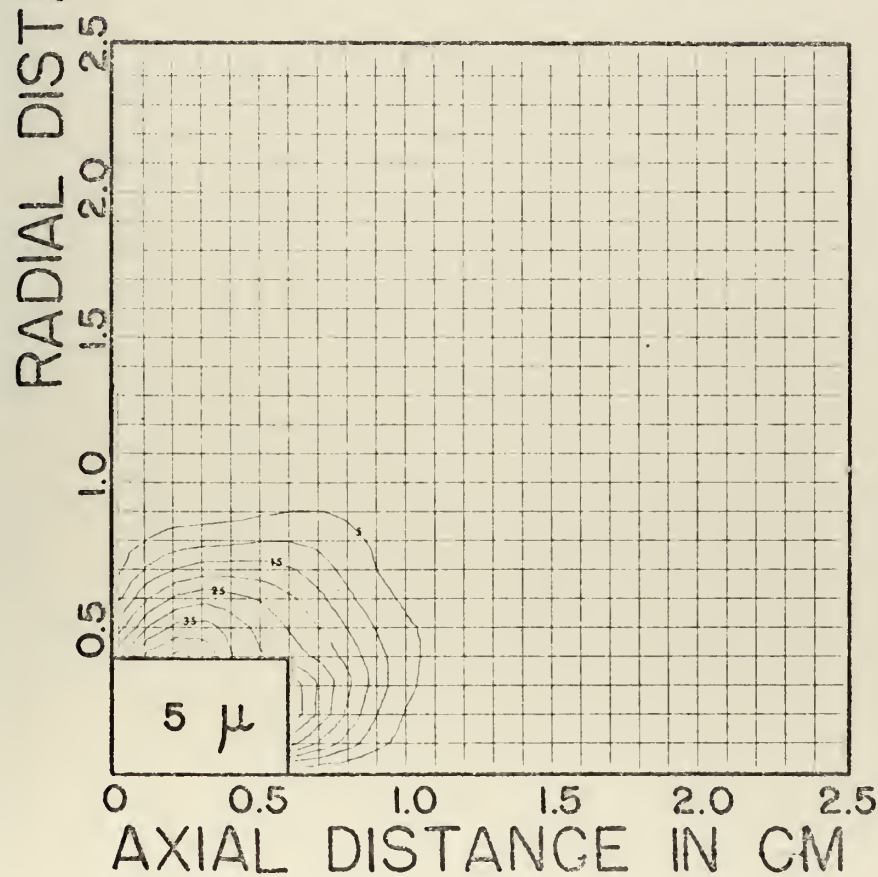


FIG. 16
 B_z IN GAUSS
 AT 20 NSEC
 FOR VARIOUS
 PRESSURES
 OF NITROGEN
 BACKGROUND
 GAS.



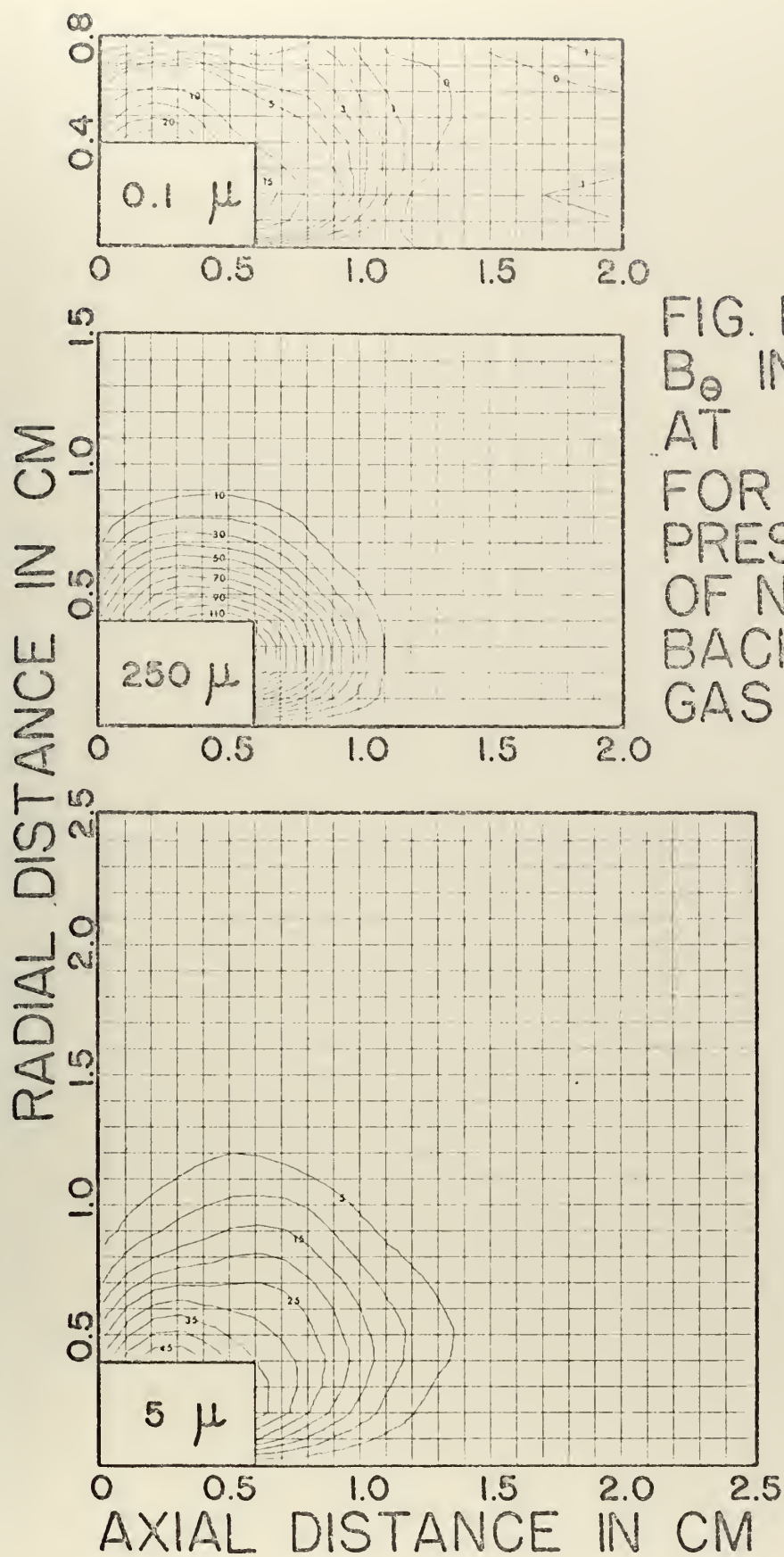


FIG. 17
 B_0 IN GAUSS
 AT 40 NSEC
 FOR VARIOUS
 PRESSURES
 OF NITROGEN
 BACKGROUND
 GAS.

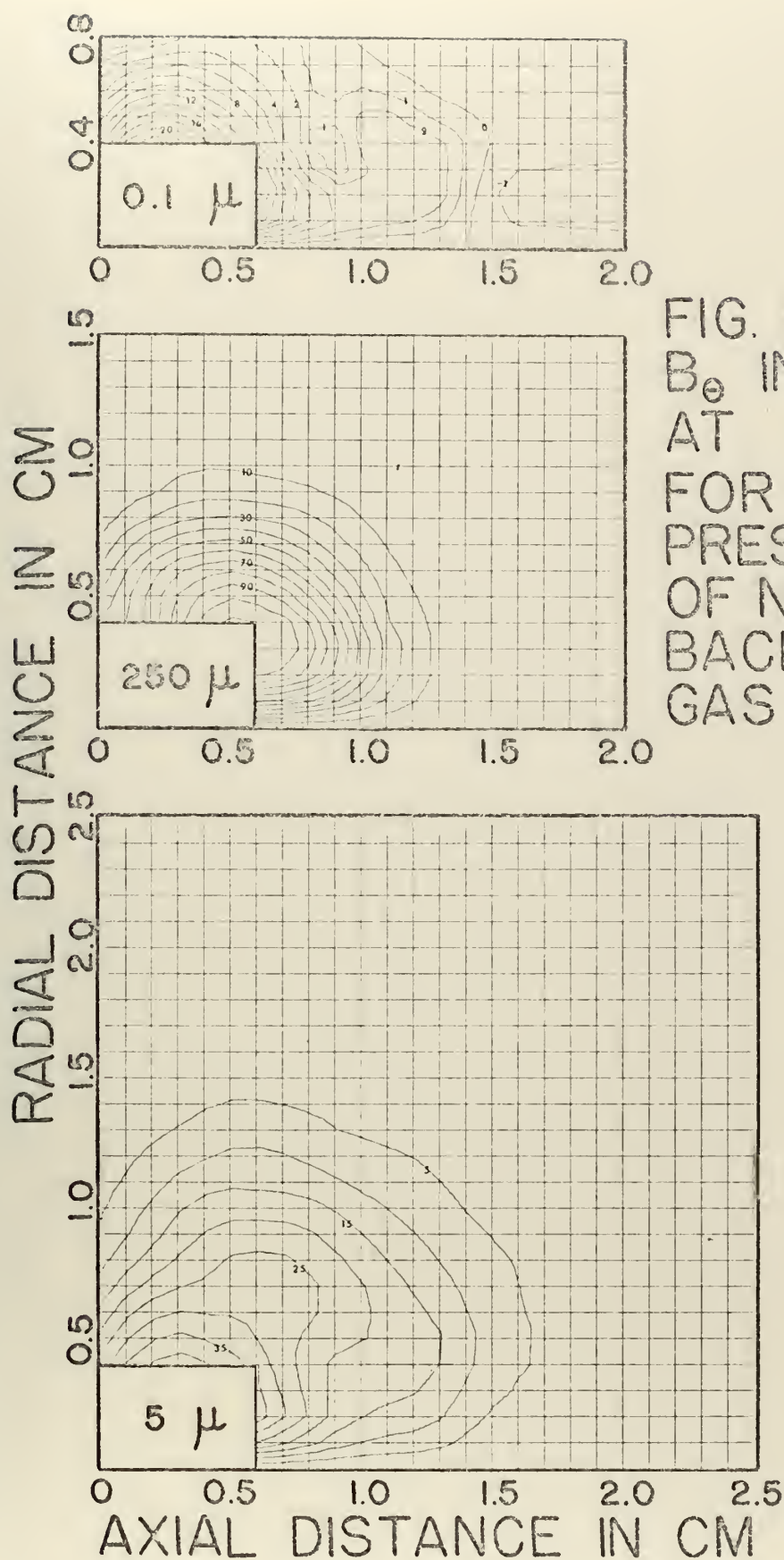


FIG. 18
 B_0 IN GAUSS
 AT 60 NSEC
 FOR VARIOUS
 PRESSURES
 OF NITROGEN
 BACKGROUND
 GAS.

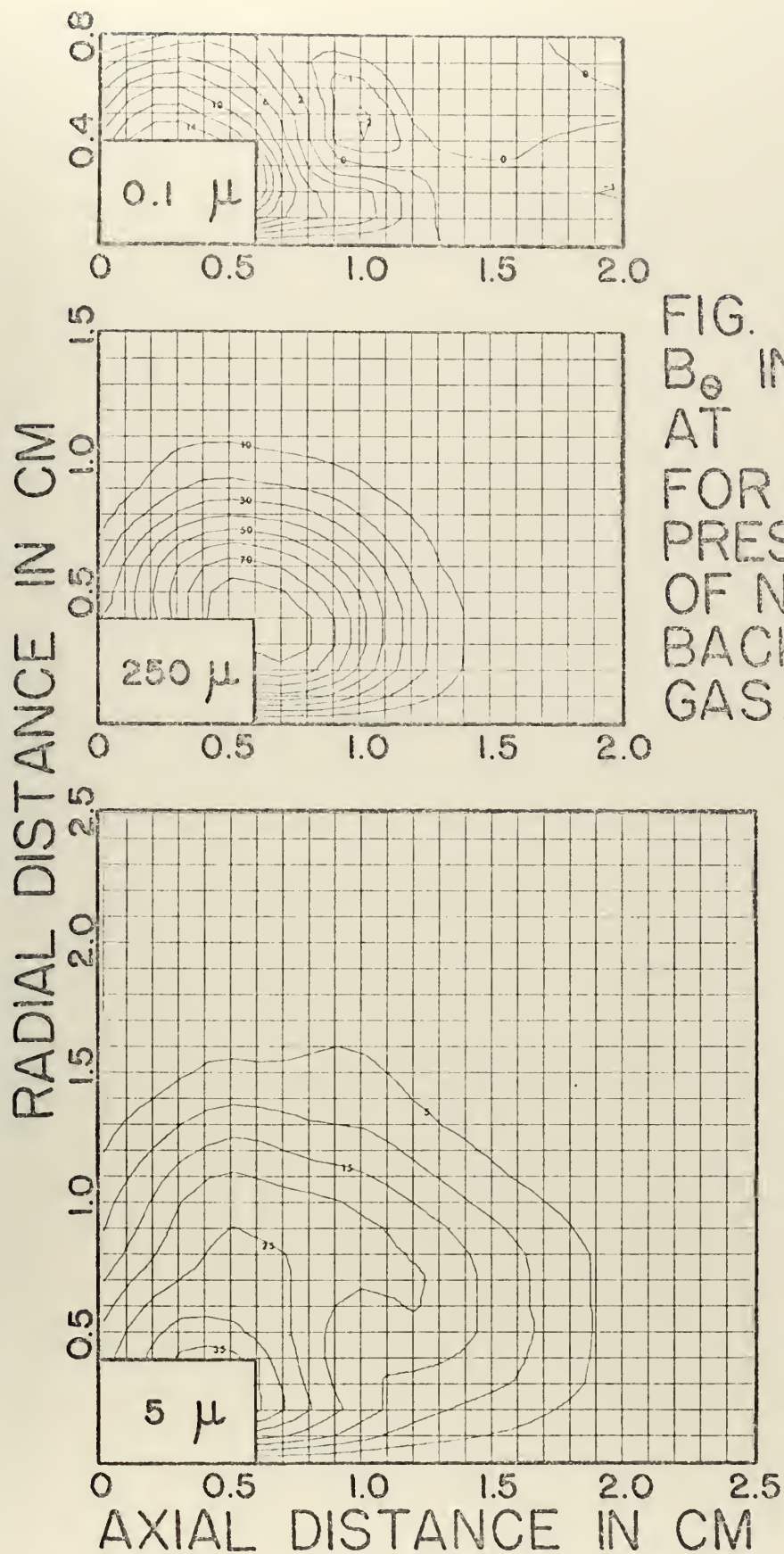


FIG. 19
 B_0 IN GAUSS
 AT 80 NSEC
 FOR VARIOUS
 PRESSURES
 OF NITROGEN
 BACKGROUND
 GAS.

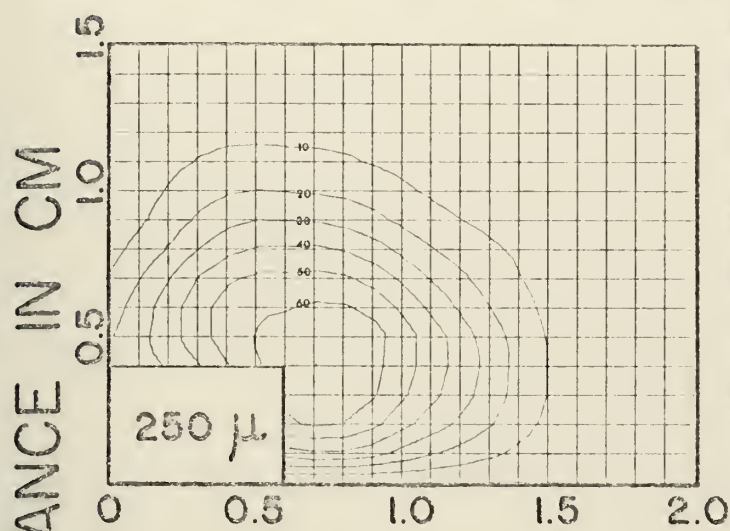
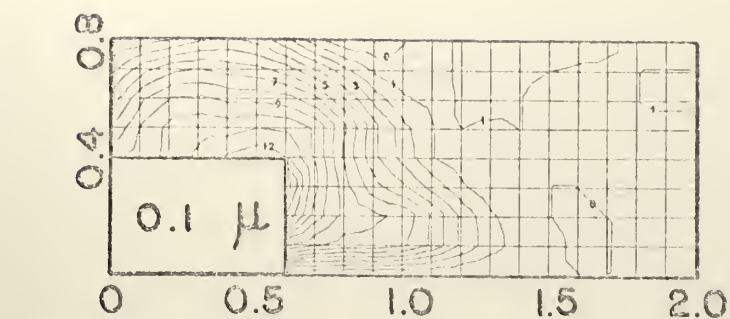
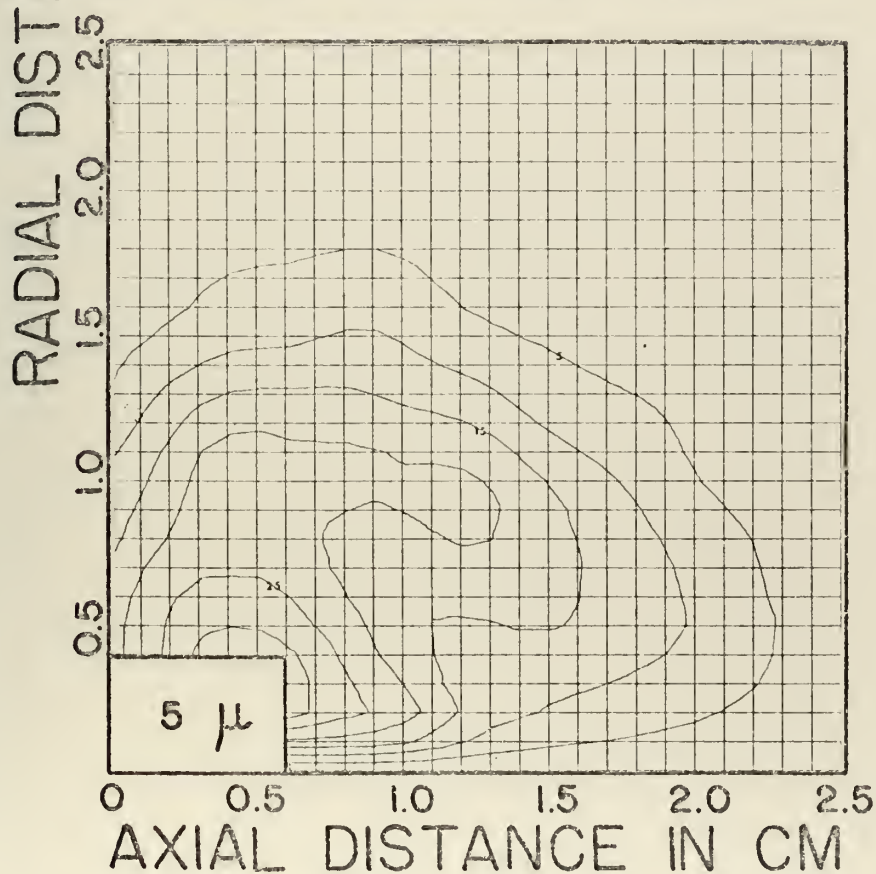


FIG. 20
 B_0 IN GAUSS
 AT 100 NSEC
 FOR VARIOUS
 PRESSURES
 OF NITROGEN
 BACKGROUND
 GAS.



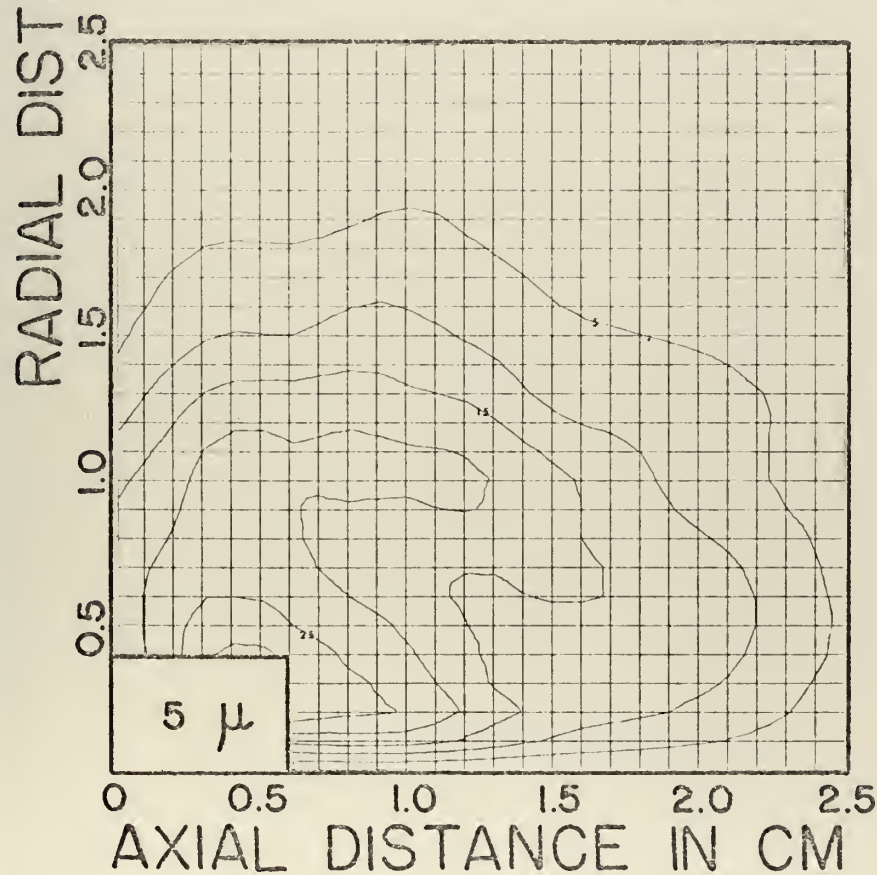
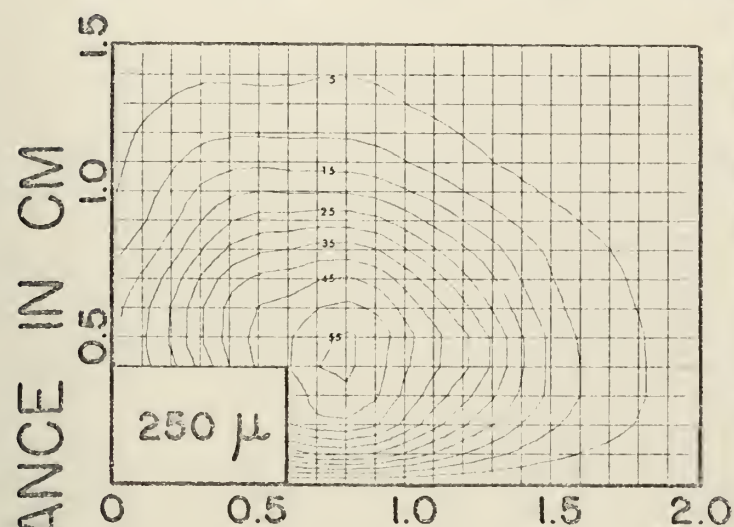
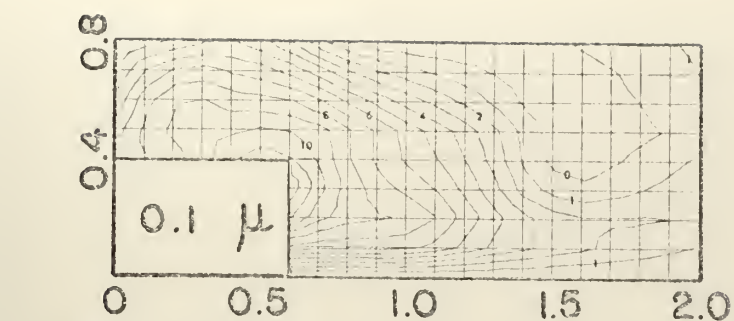


FIG. 21
 B_0 IN GAUSS
 AT 120 NSEC
 FOR VARIOUS
 PRESSURES
 OF NITROGEN
 BACKGROUND
 GAS.

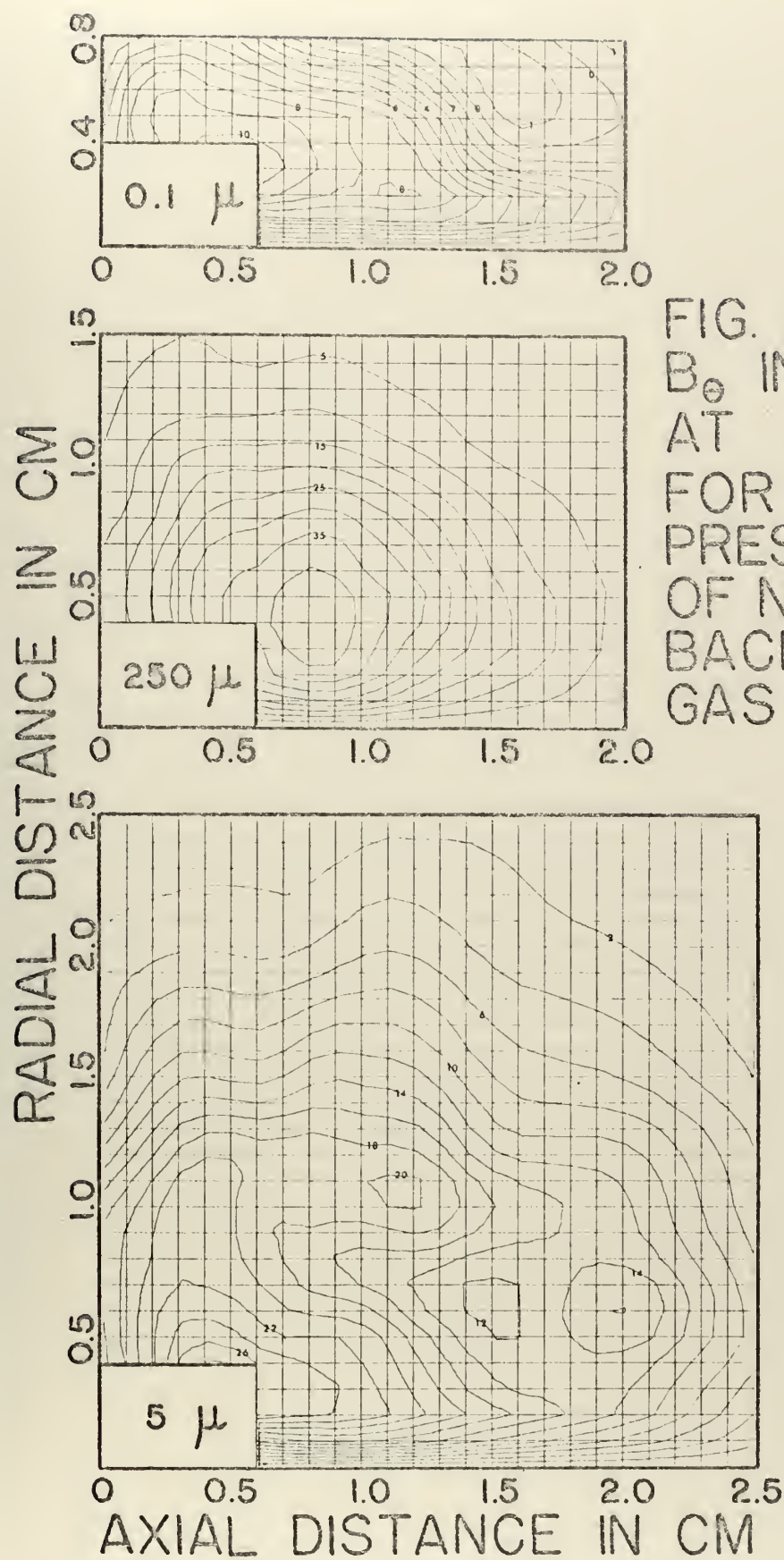


FIG. 22
 B_0 IN GAUSS
 AT 140 NSEC
 FOR VARIOUS
 PRESSURES
 OF NITROGEN
 BACKGROUND
 GAS.

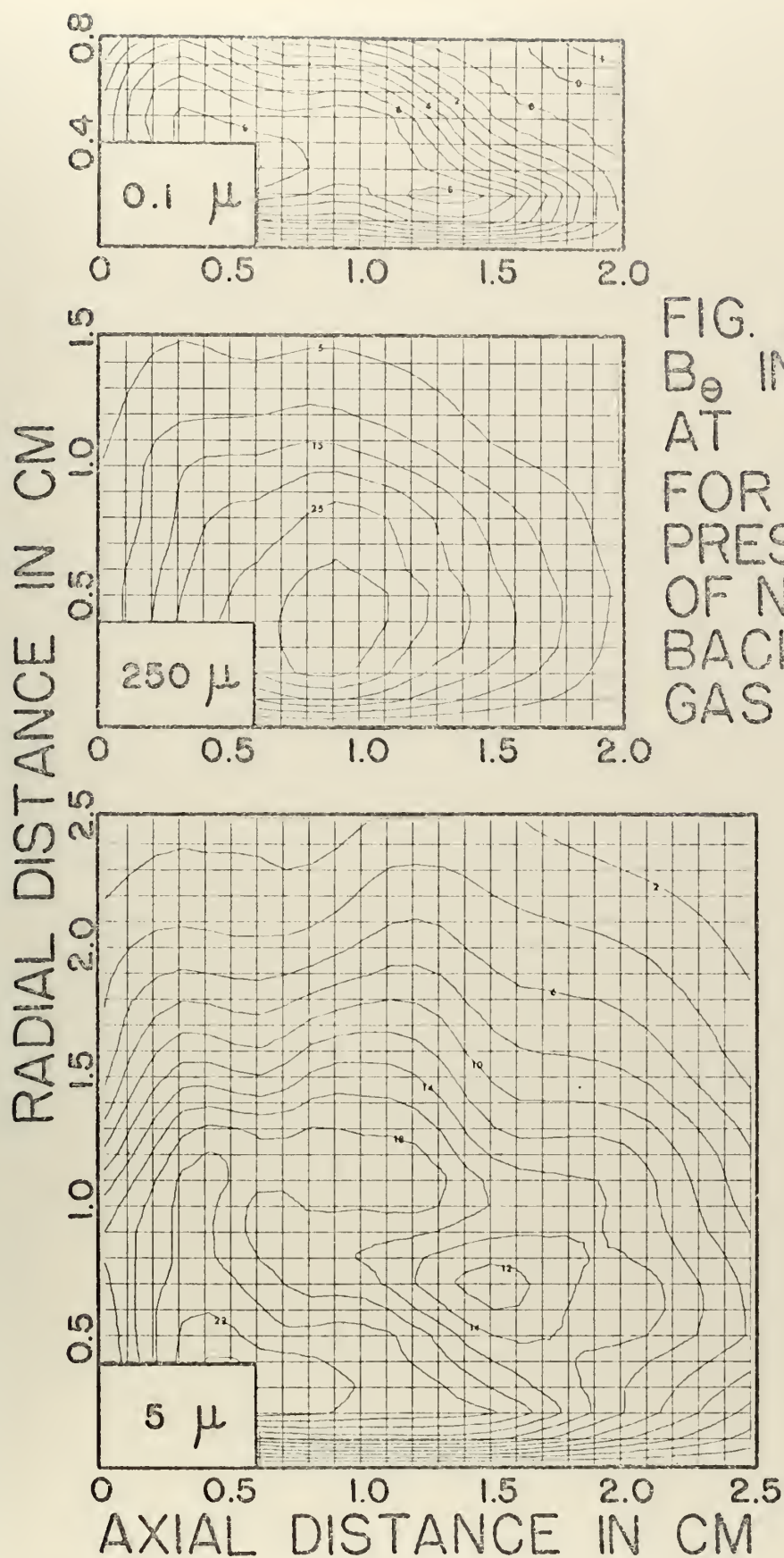


FIG. 23
 B_0 IN GAUSS
 AT 160 NSEC
 FOR VARIOUS
 PRESSURES
 OF NITROGEN
 BACKGROUND
 GAS.

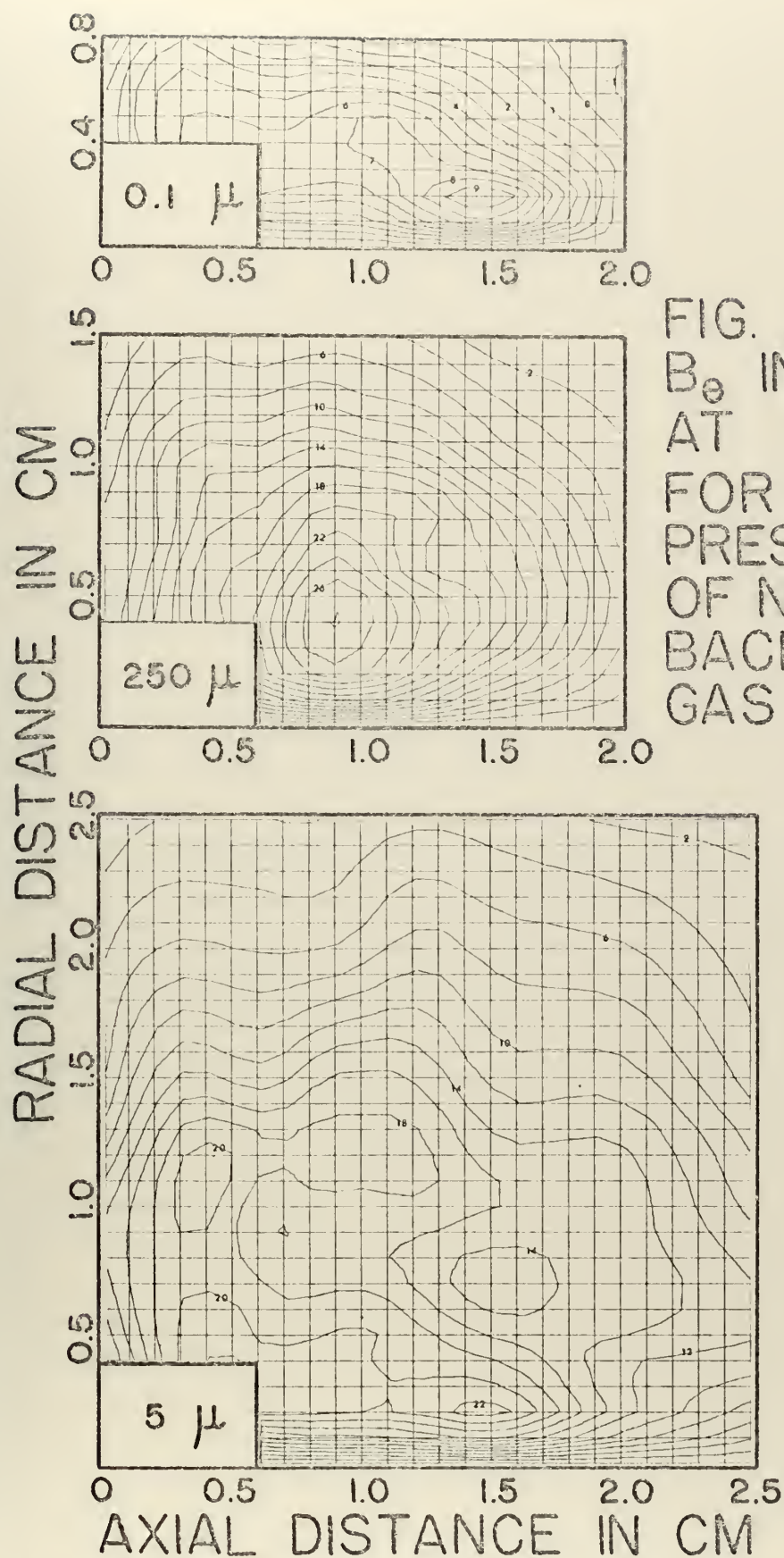


FIG. 24
 B_0 IN GAUSS
 AT 180 NSEC
 FOR VARIOUS
 PRESSURES
 OF NITROGEN
 BACKGROUND
 GAS.

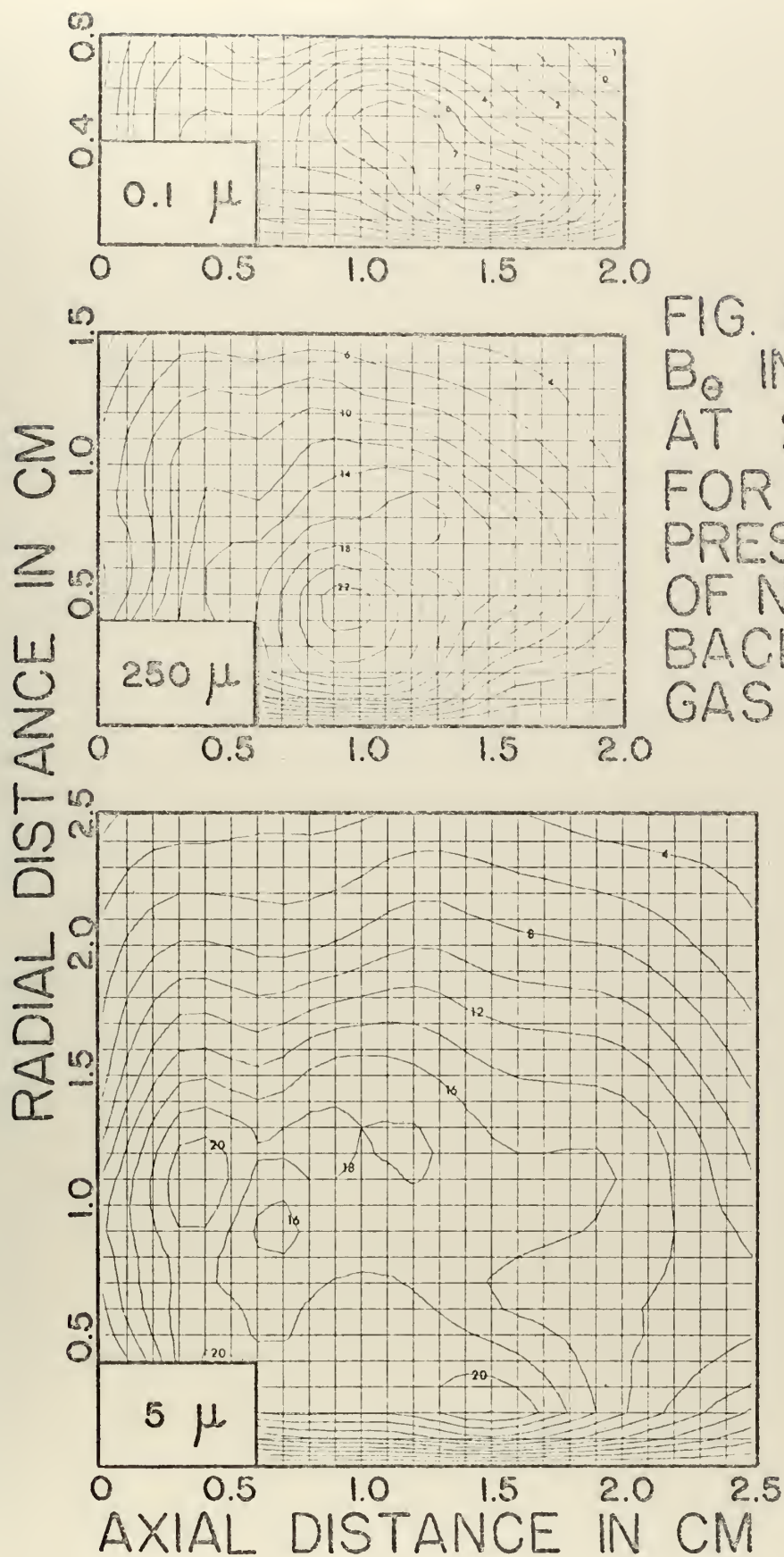


FIG. 25
 B_0 IN GAUSS
 AT 200 NSEC
 FOR VARIOUS
 PRESSURES
 OF NITROGEN
 BACKGROUND
 GAS.

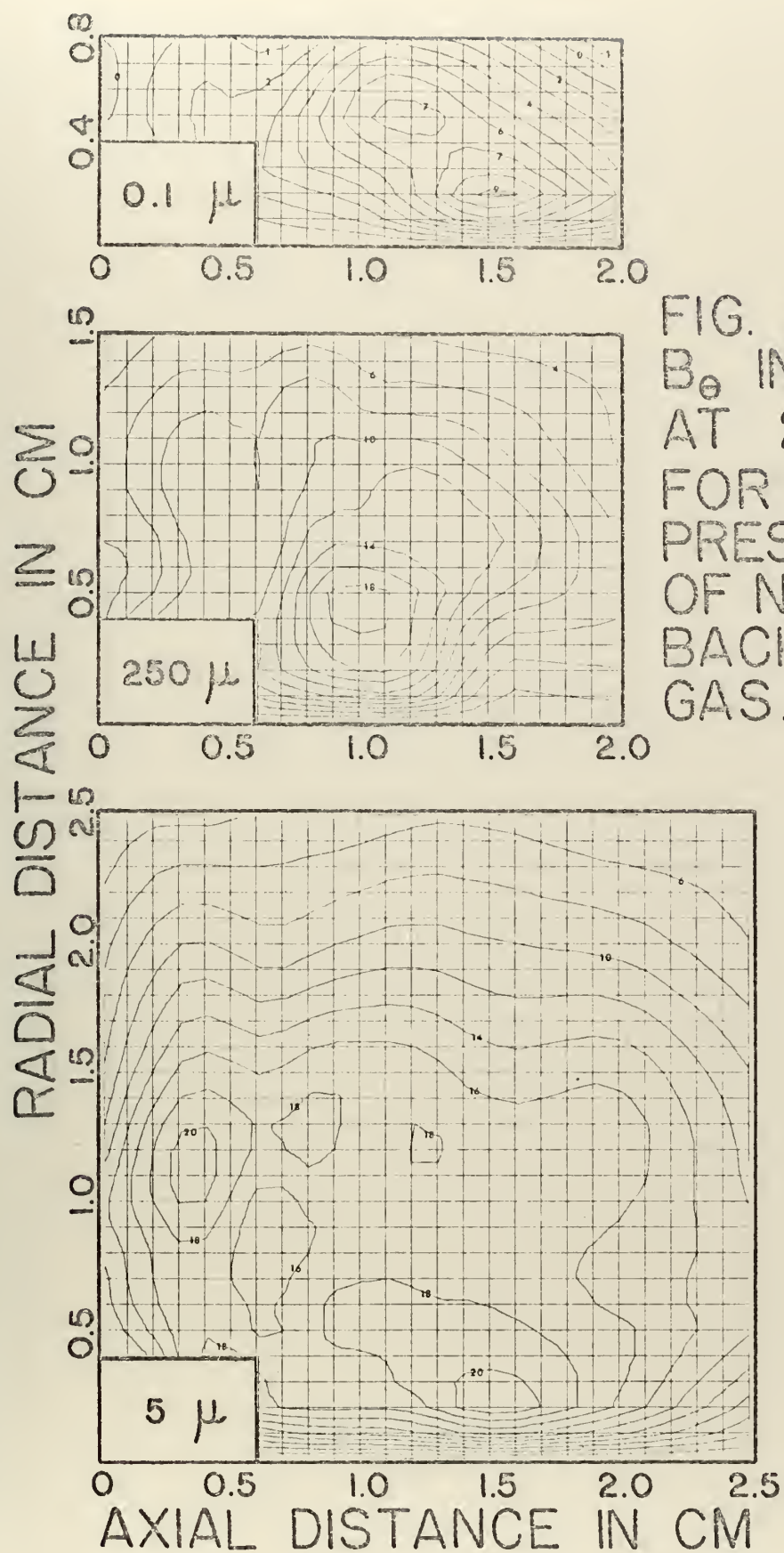


FIG. 26
 B_0 IN GAUSS
 AT 220 NSEC
 FOR VARIOUS
 PRESSURES
 OF NITROGEN
 BACKGROUND
 GAS.

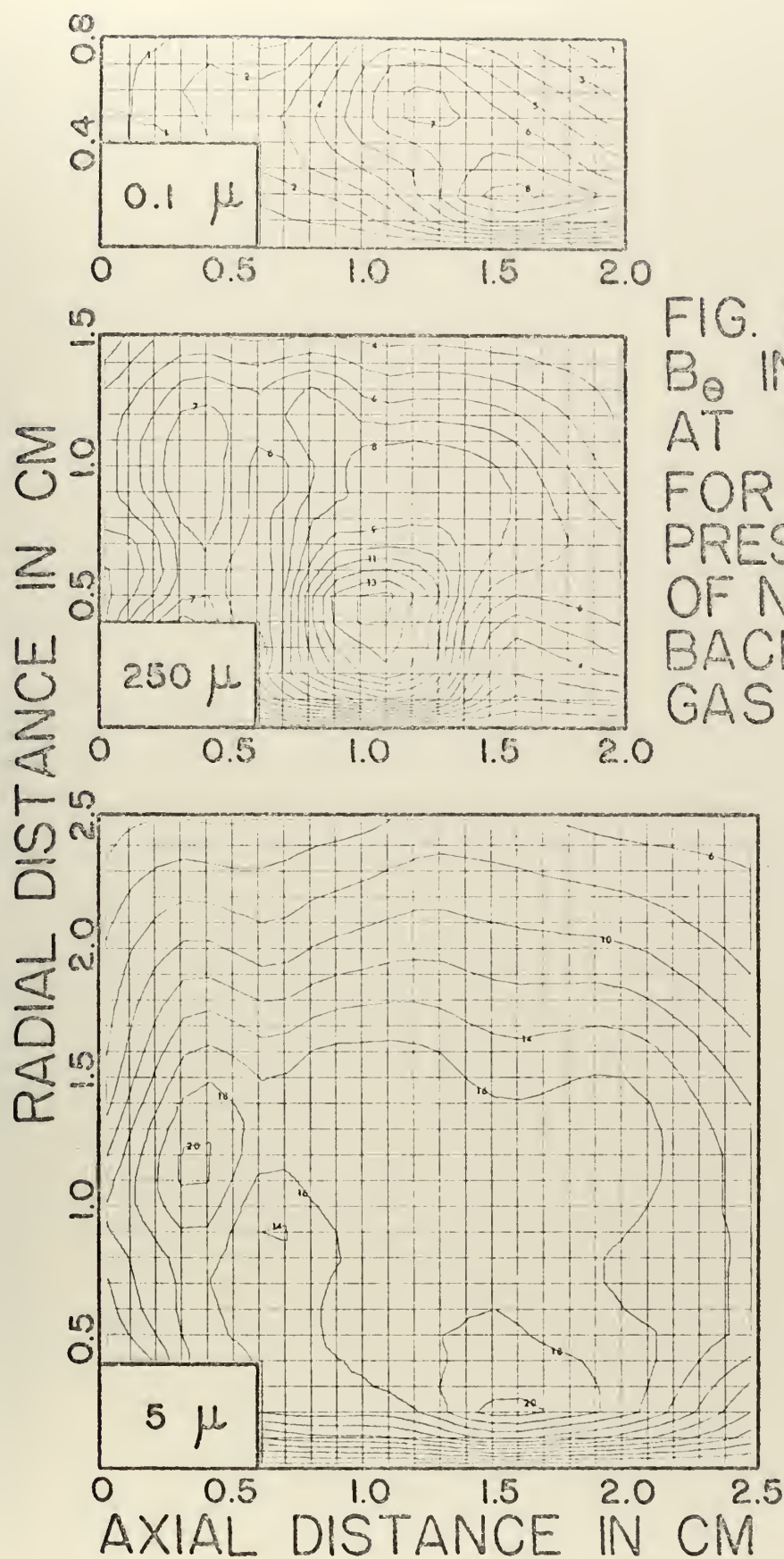


FIG. 27
 B_0 IN GAUSS
 AT 240 NSEC
 FOR VARIOUS
 PRESSURES
 OF NITROGEN
 BACKGROUND
 GAS.

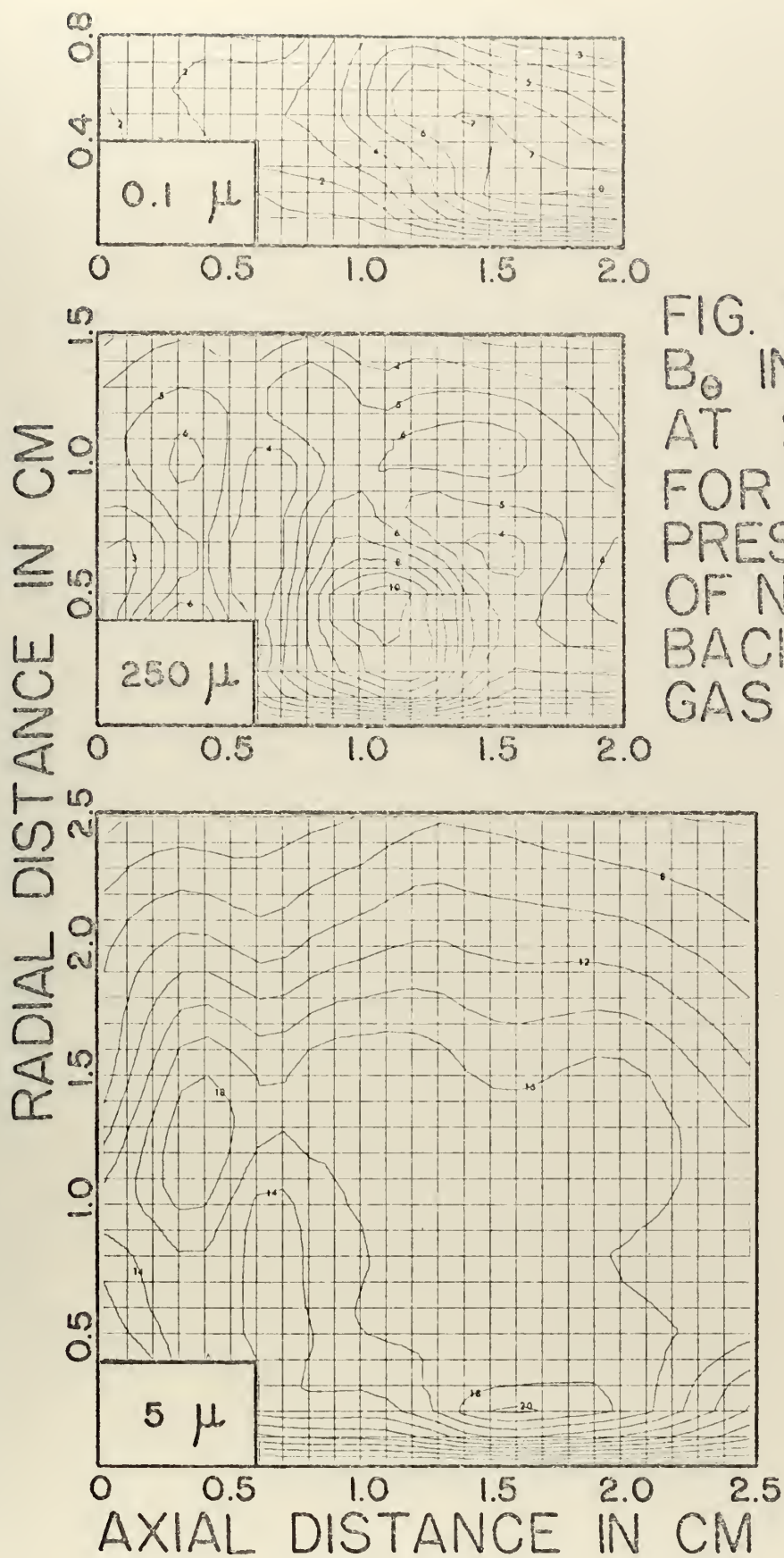


FIG. 28
 B_0 IN GAUSS
 AT 260 NSEC
 FOR VARIOUS
 PRESSURES
 OF NITROGEN
 BACKGROUND
 GAS.

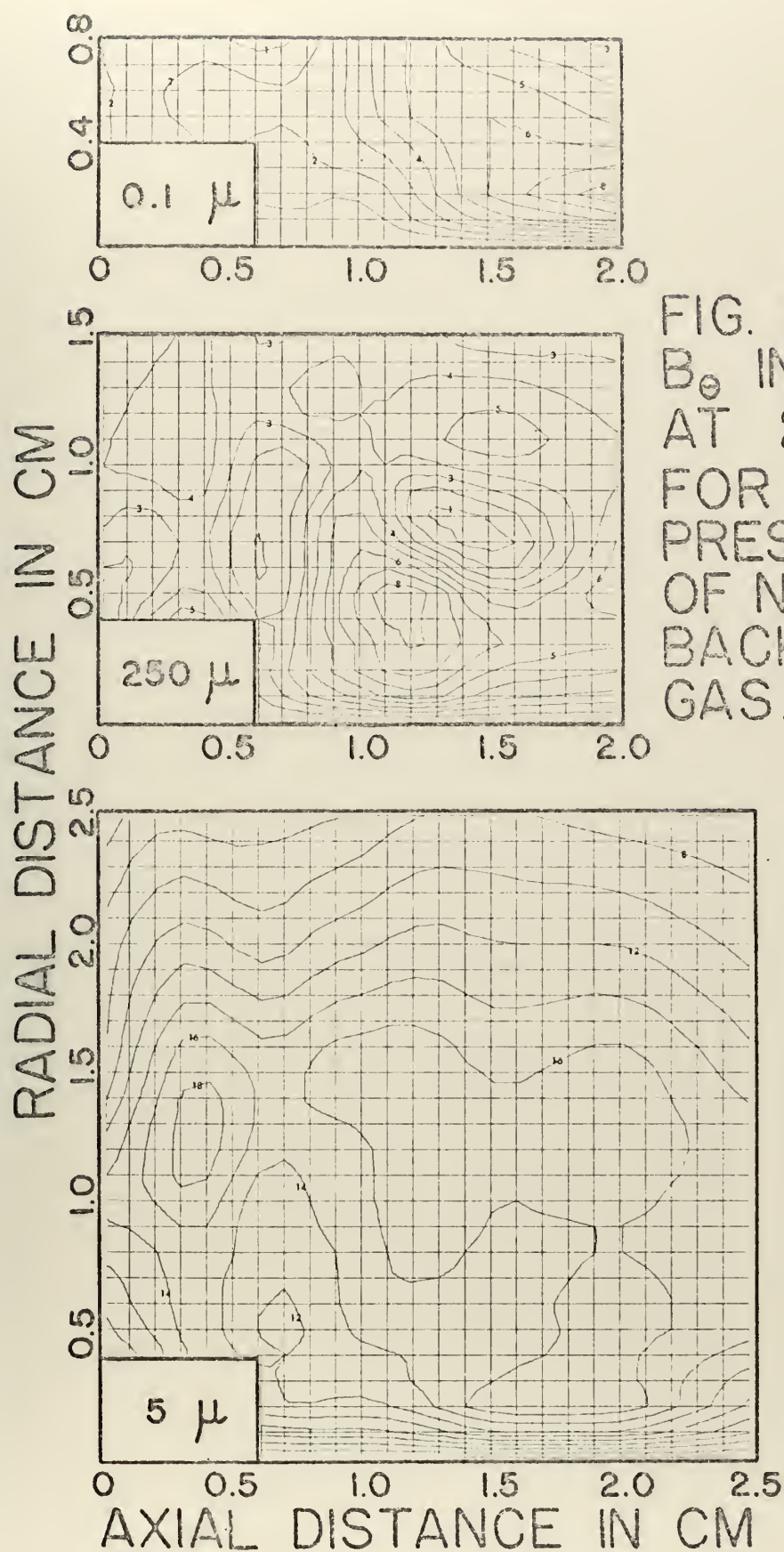


FIG. 29
 B_0 IN GAUSS
 AT 280 NSEC
 FOR VARIOUS
 PRESSURES
 OF NITROGEN
 BACKGROUND
 GAS.

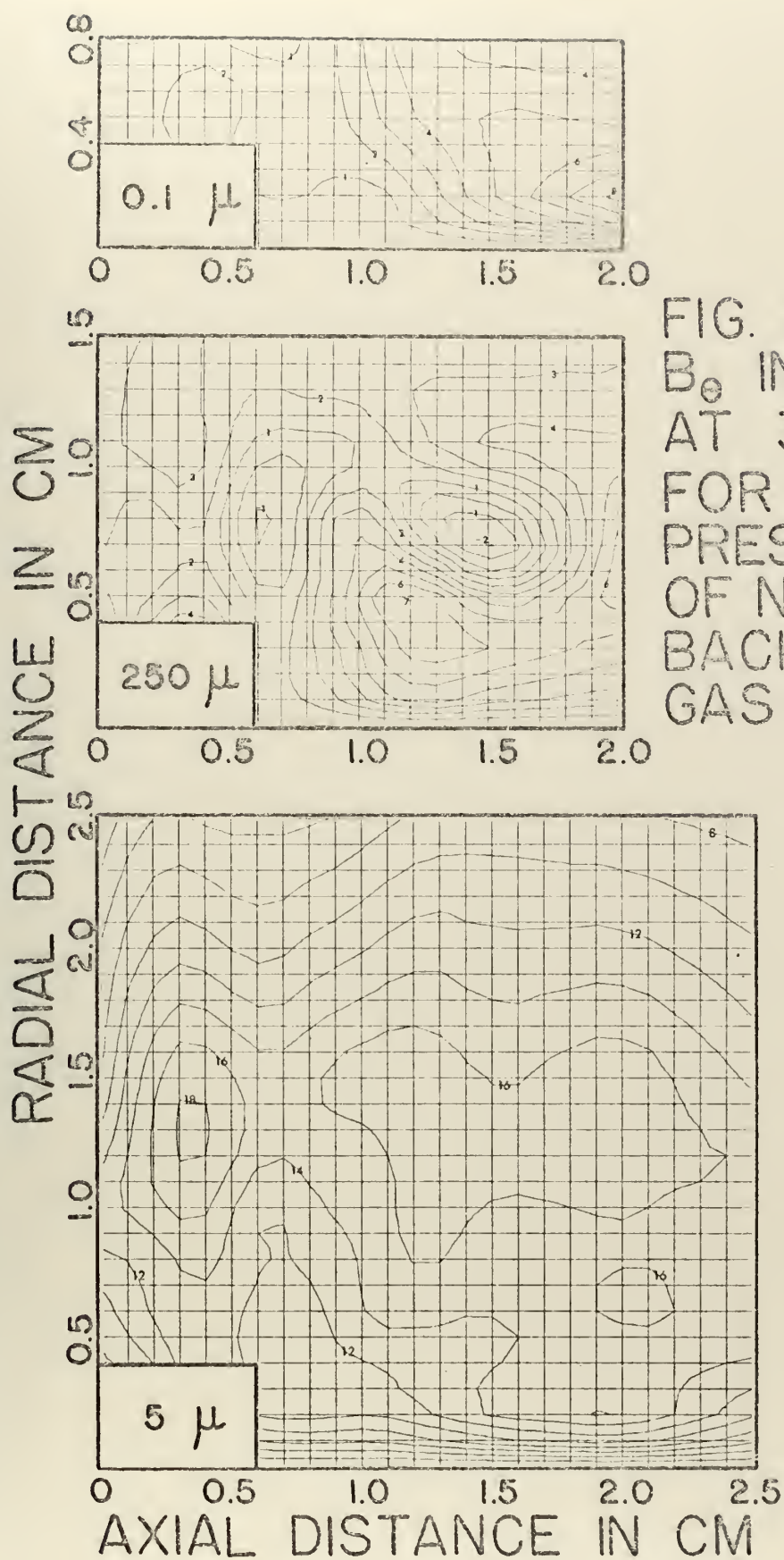


FIG. 30
 B_0 IN GAUSS
 AT 300 NSEC
 FOR VARIOUS
 PRESSURES
 OF NITROGEN
 BACKGROUND
 GAS.

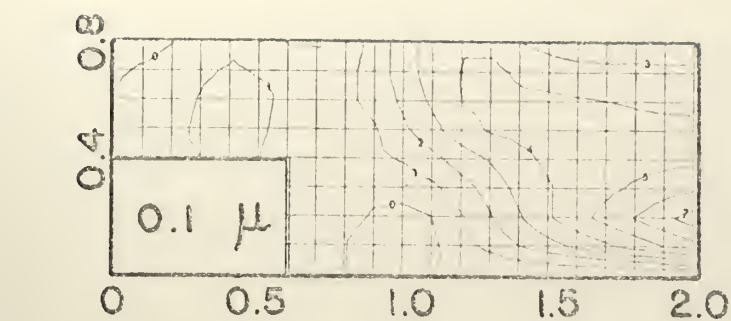
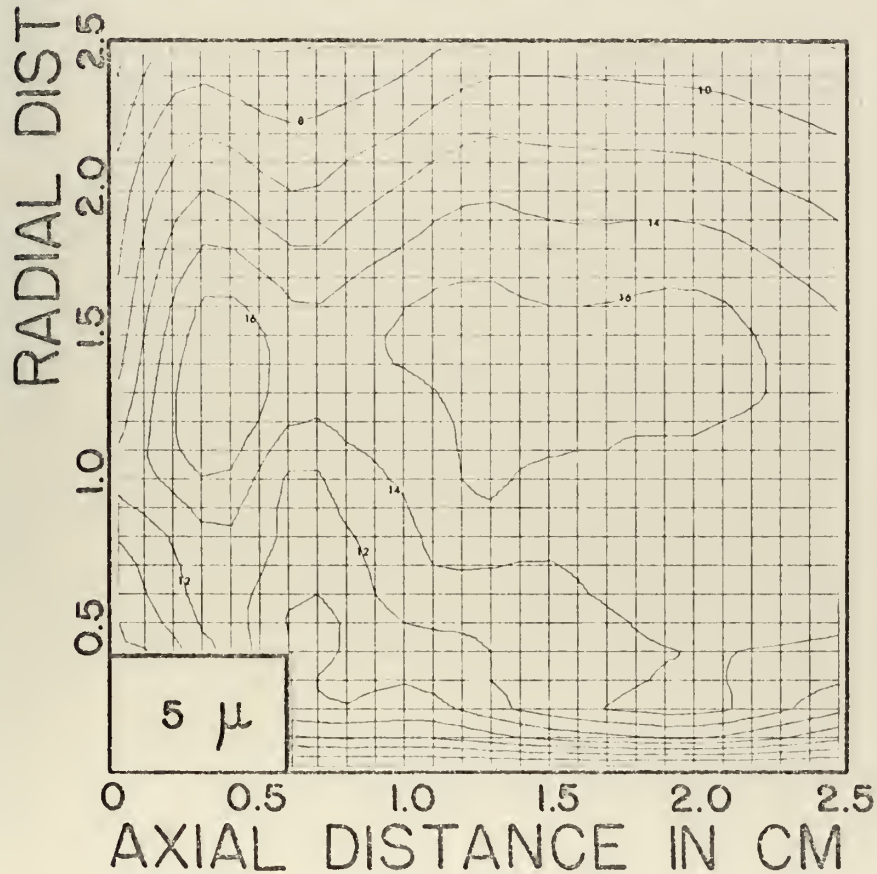
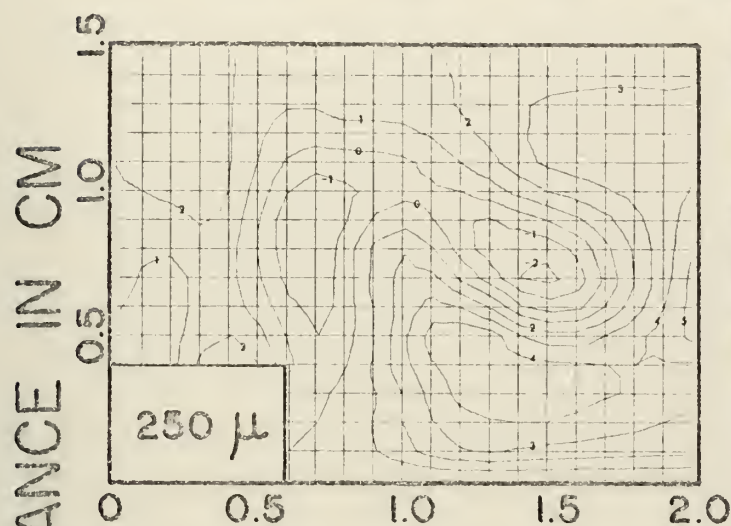


FIG. 31
 B_0 IN GAUSS
 AT 320 NSEC
 FOR VARIOUS
 PRESSURES
 OF NITROGEN
 BACKGROUND
 GAS.



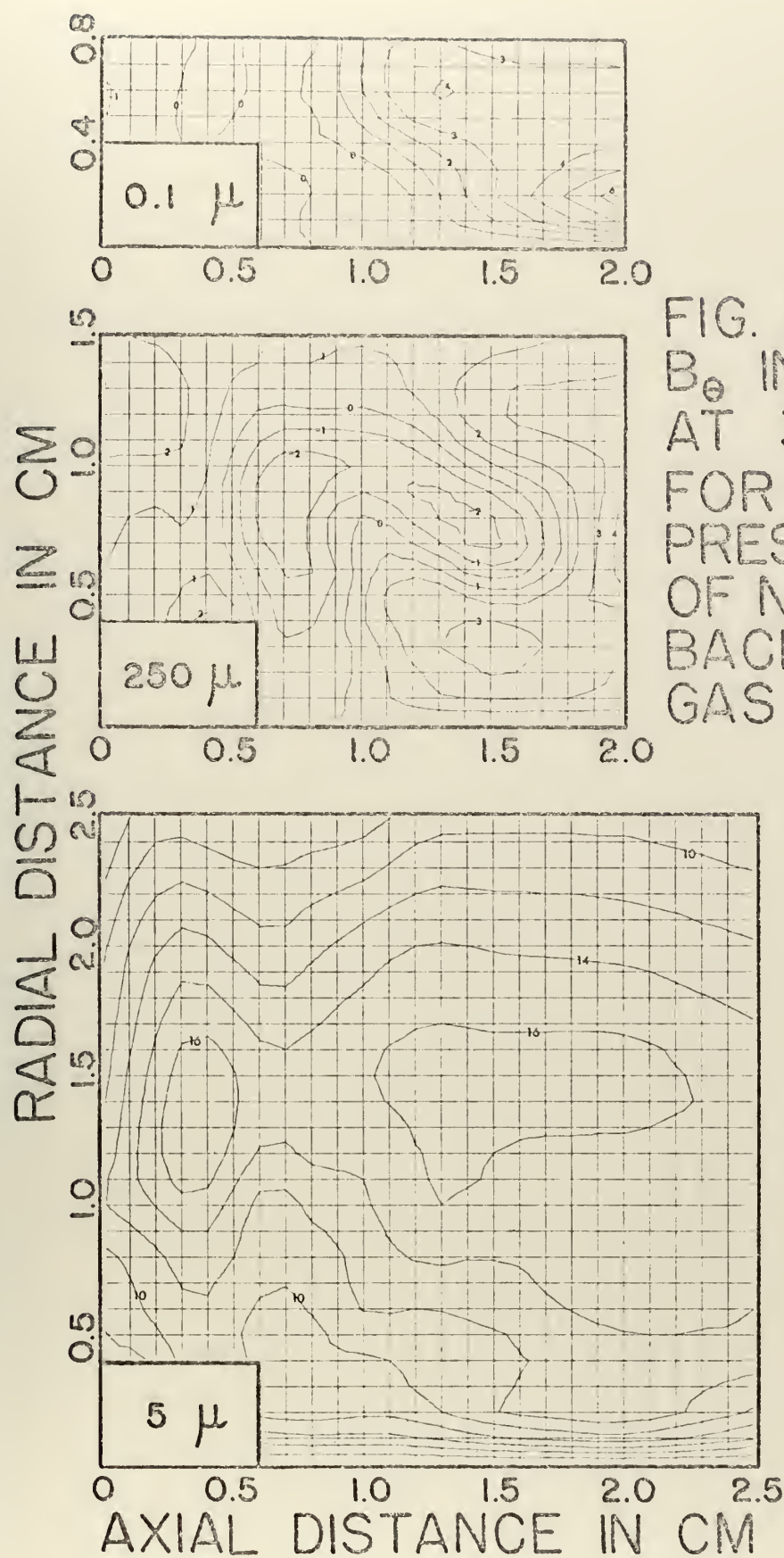


FIG. 32
 B_0 IN GAUSS
 AT 340 NSEC
 FOR VARIOUS
 PRESSURES
 OF NITROGEN
 BACKGROUND
 GAS.

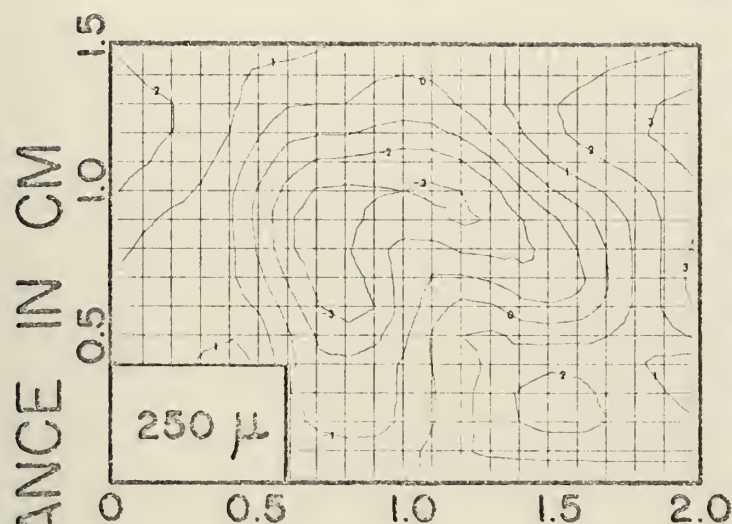
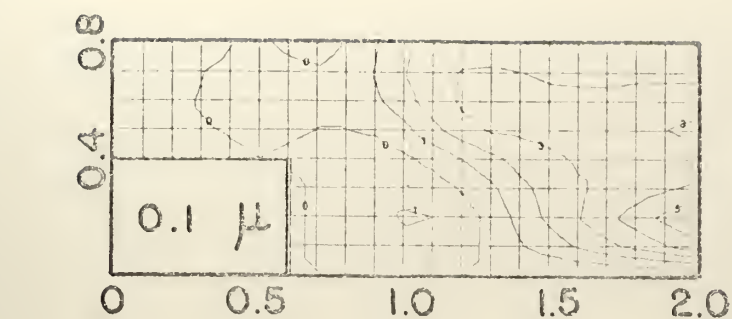
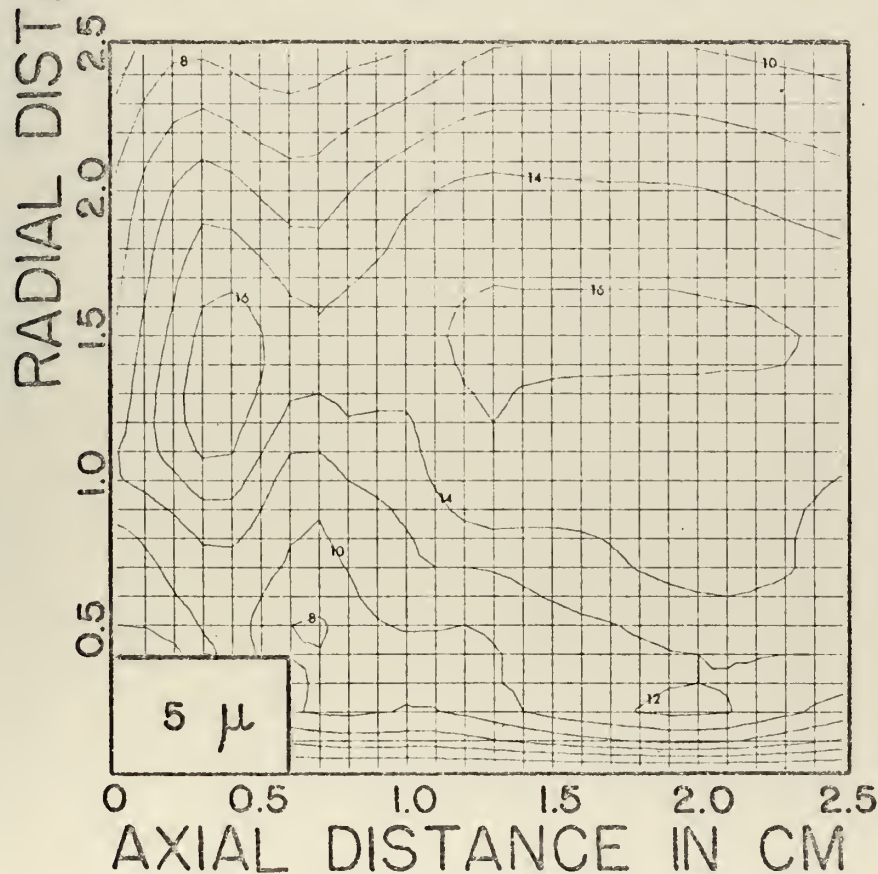


FIG. 33
 B_0 IN GAUSS
 AT 360 NSEC
 FOR VARIOUS
 PRESSURES
 OF NITROGEN
 BACKGROUND
 GAS.



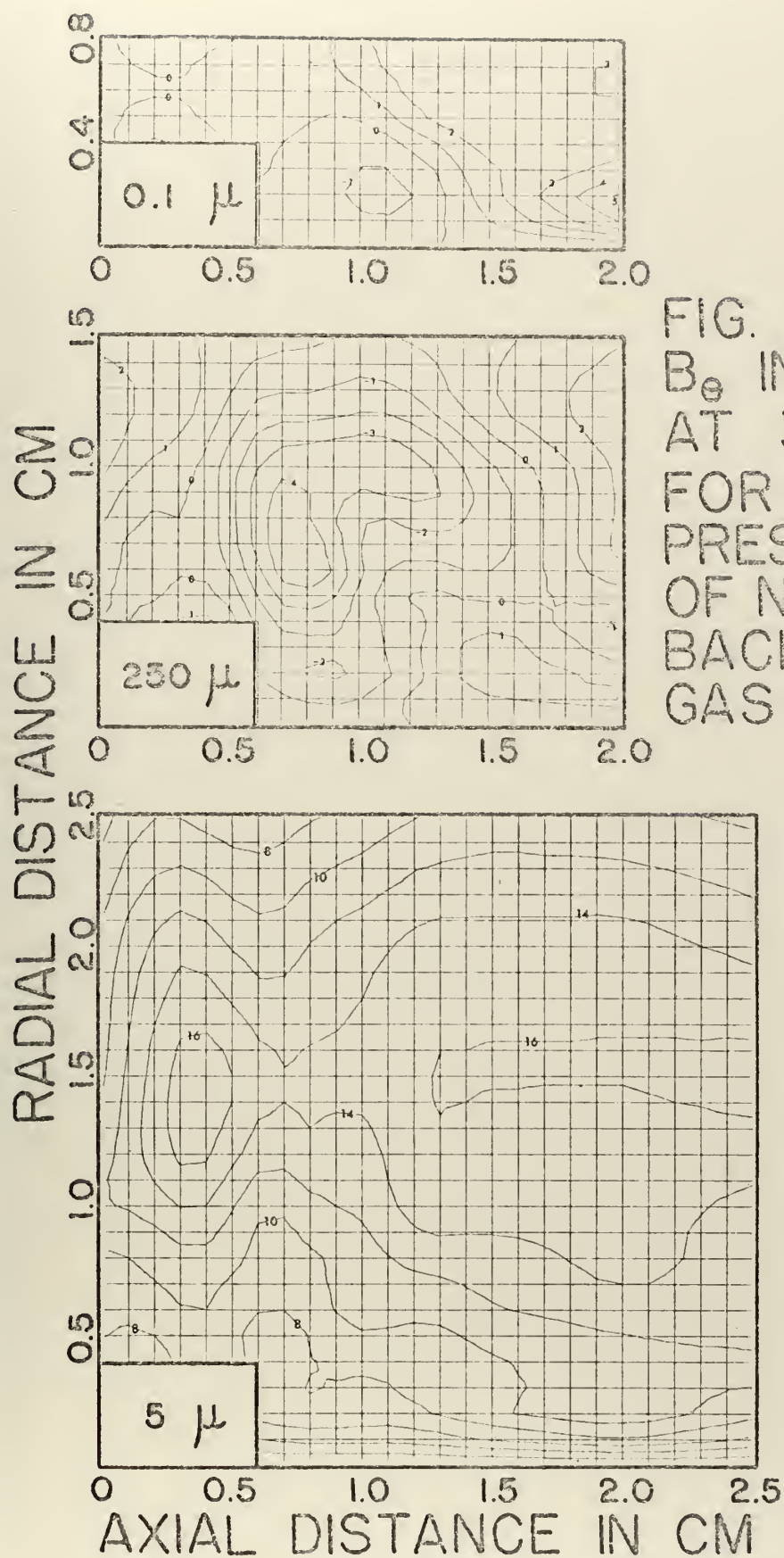


FIG. 34
 B_z IN GAUSS
 AT 380 NSEC
 FOR VARIOUS
 PRESSURES
 OF NITROGEN
 BACKGROUND
 GAS.

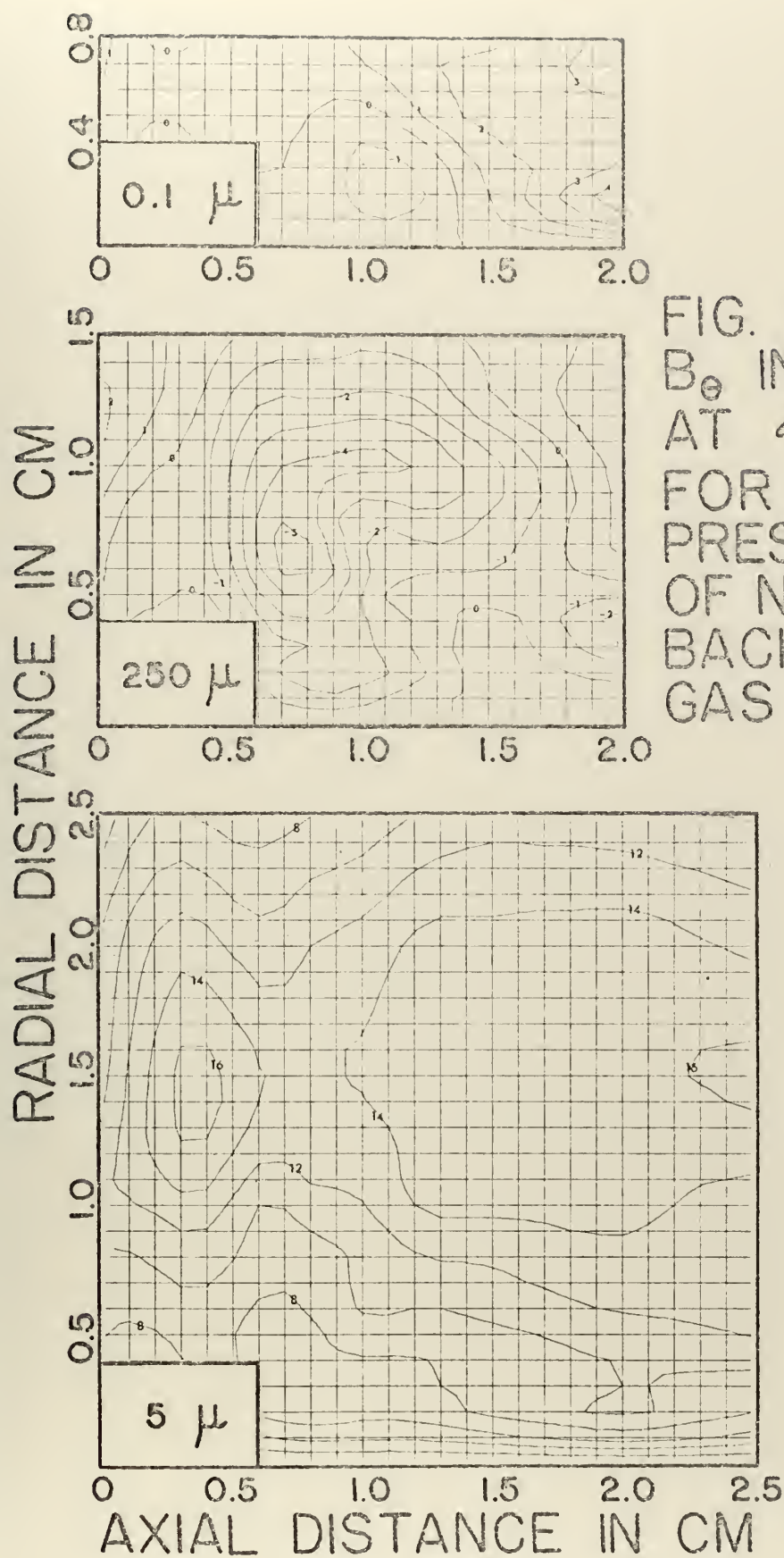


FIG. 35
 B_z IN GAUSS
 AT 400 NSEC
 FOR VARIOUS
 PRESSURES
 OF NITROGEN
 BACKGROUND
 GAS.

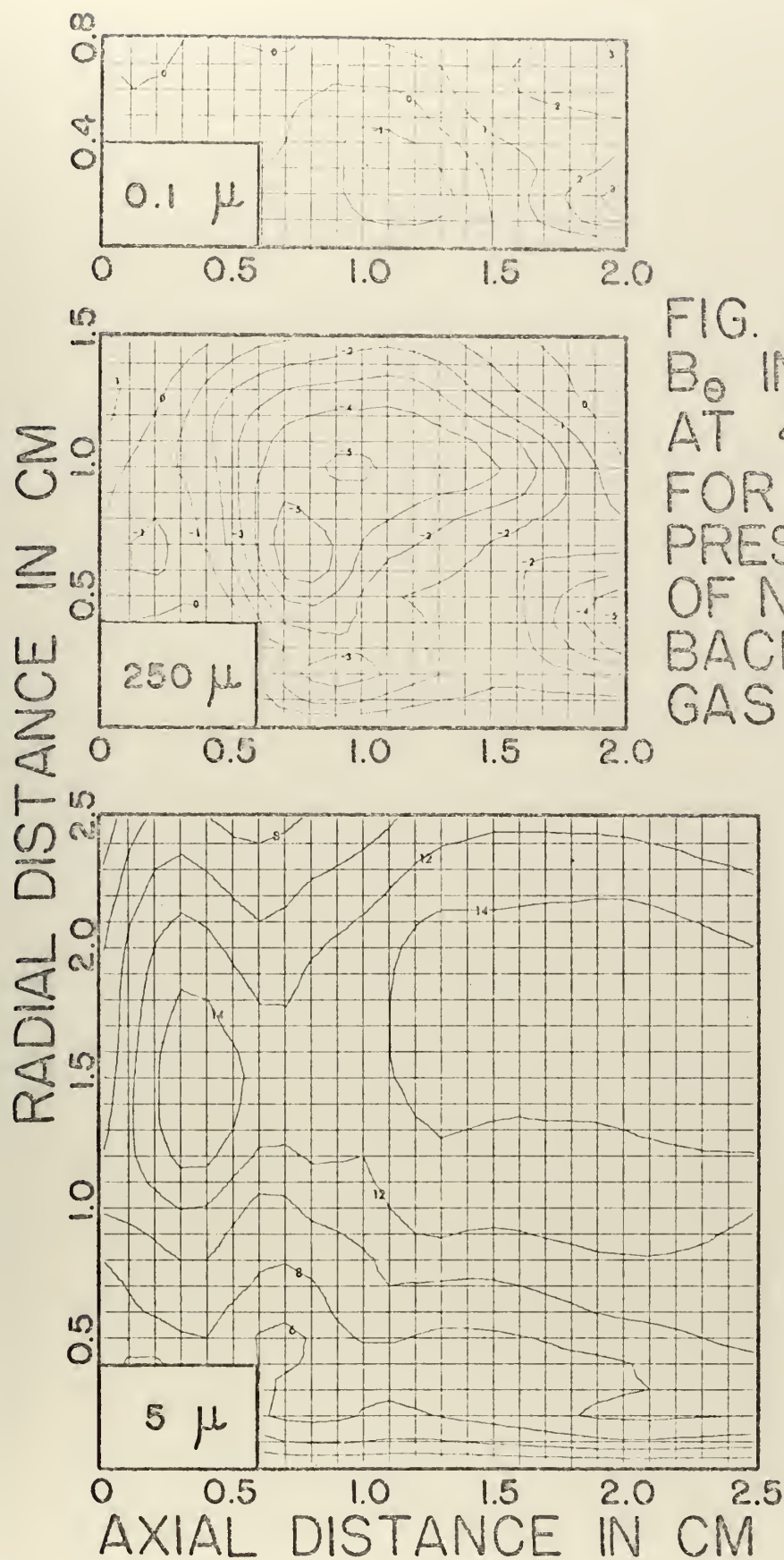


FIG. 36
 B_0 IN GAUSS
 AT 440 NSEC
 FOR VARIOUS
 PRESSURES
 OF NITROGEN
 BACKGROUND
 GAS.

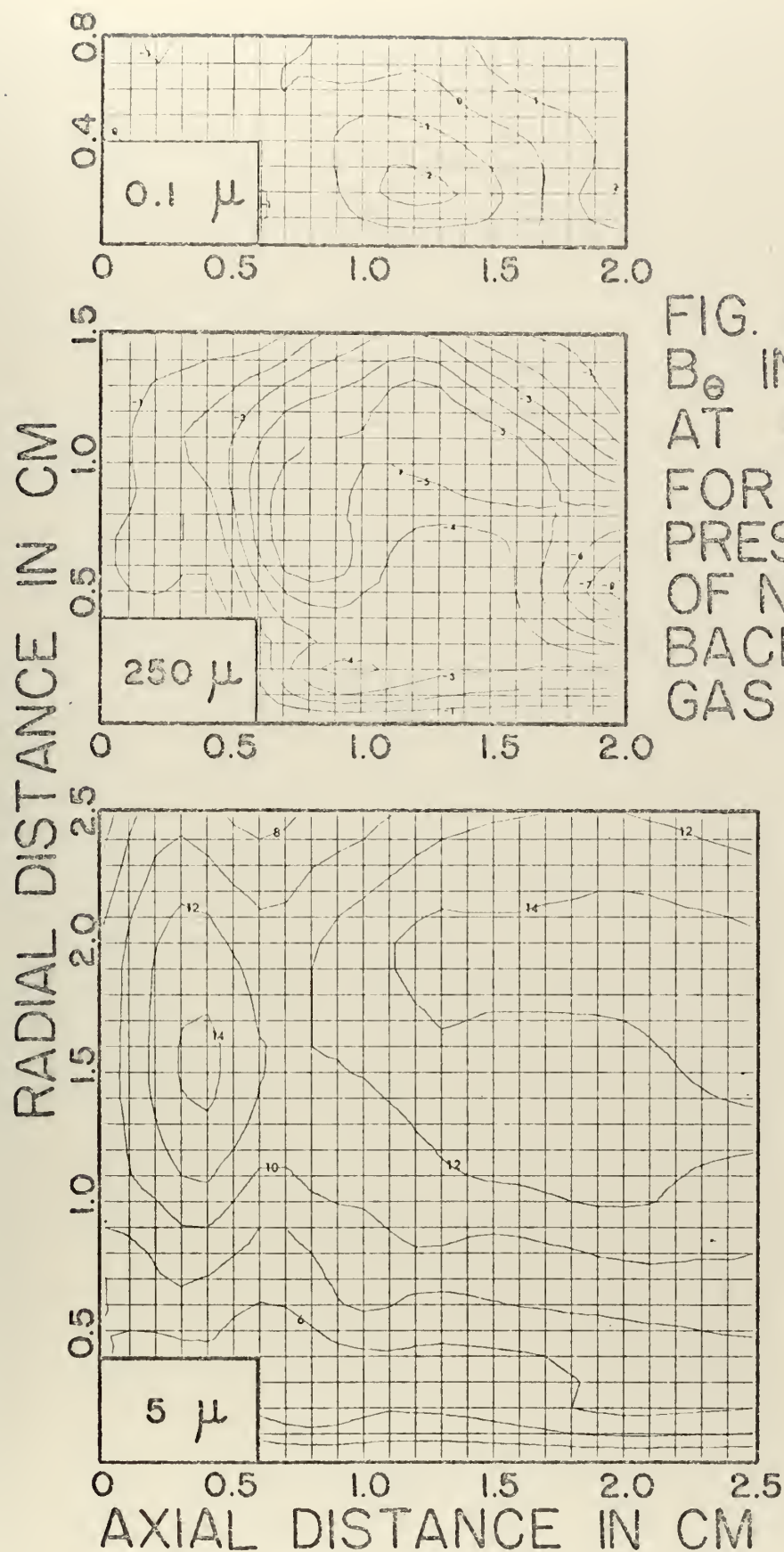


FIG. 37
 B_0 IN GAUSS
 AT 500 NSEC
 FOR VARIOUS
 PRESSURES
 OF NITROGEN
 BACKGROUND
 GAS.

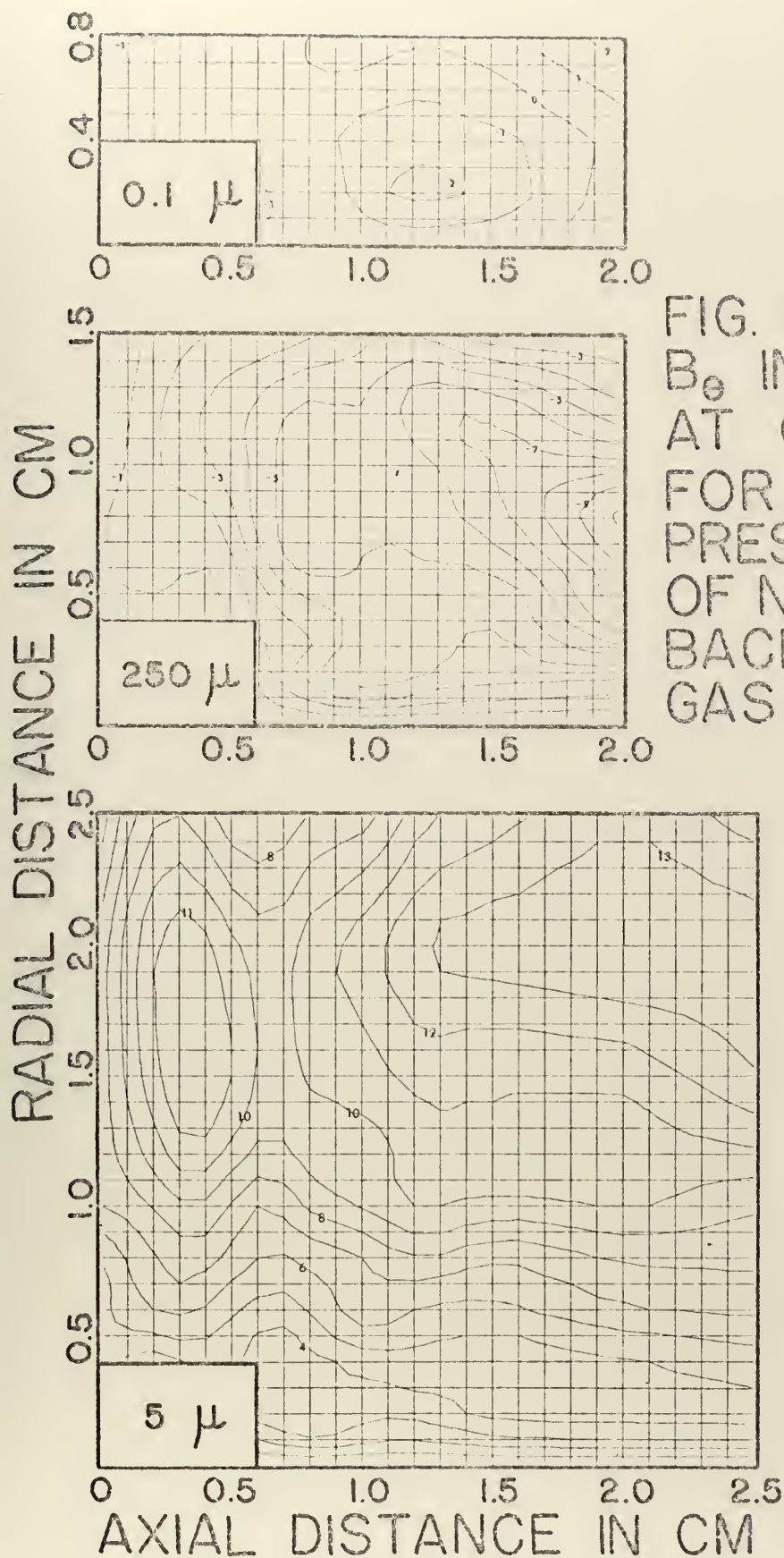


FIG. 38
 B_0 IN GAUSS
 AT 600 NSEC
 FOR VARIOUS
 PRESSURES
 OF NITROGEN
 BACKGROUND
 GAS.

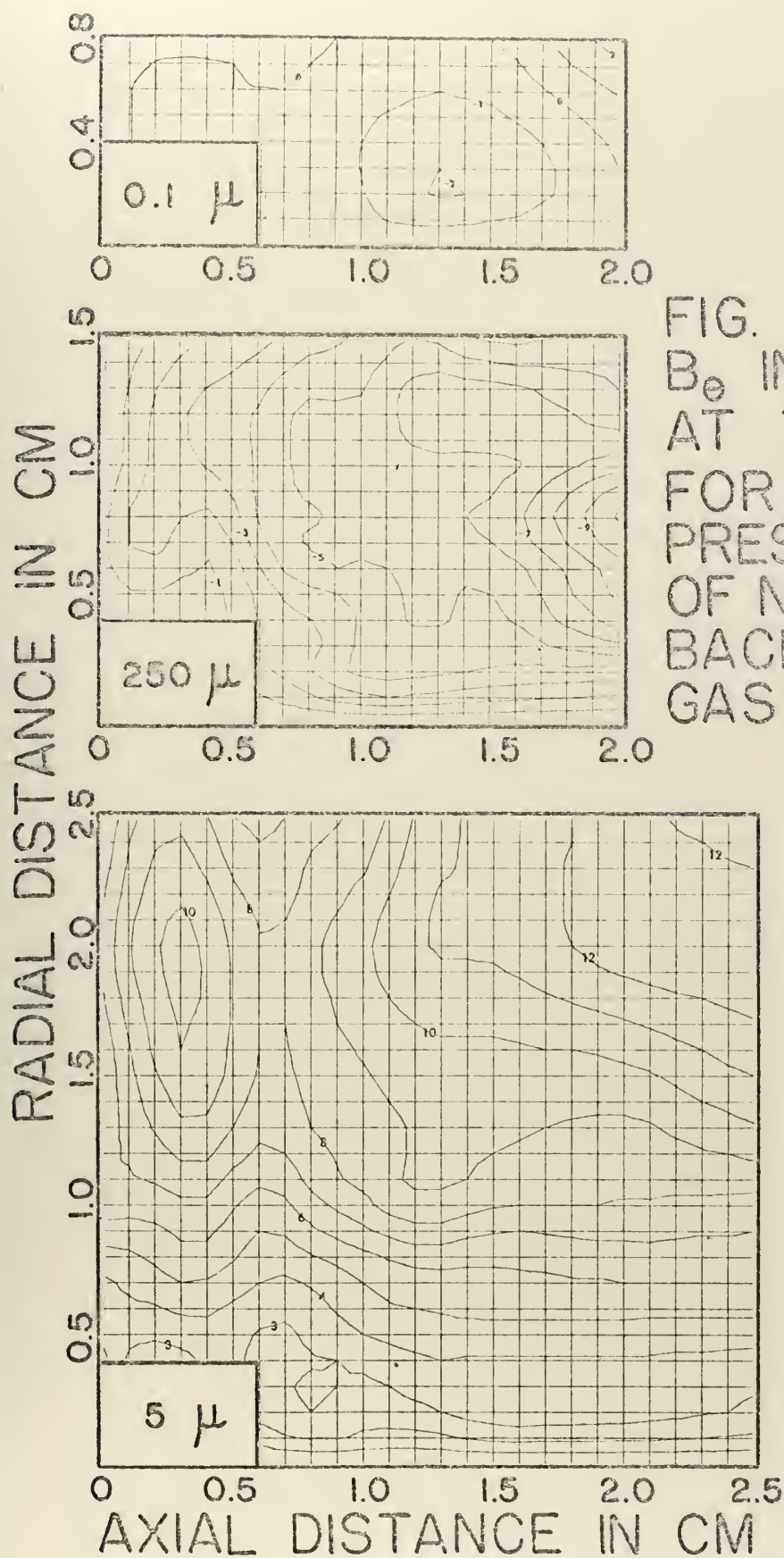


FIG. 39
 B_0 IN GAUSS
 AT 700 NSEC
 FOR VARIOUS
 PRESSURES
 OF NITROGEN
 BACKGROUND
 GAS.

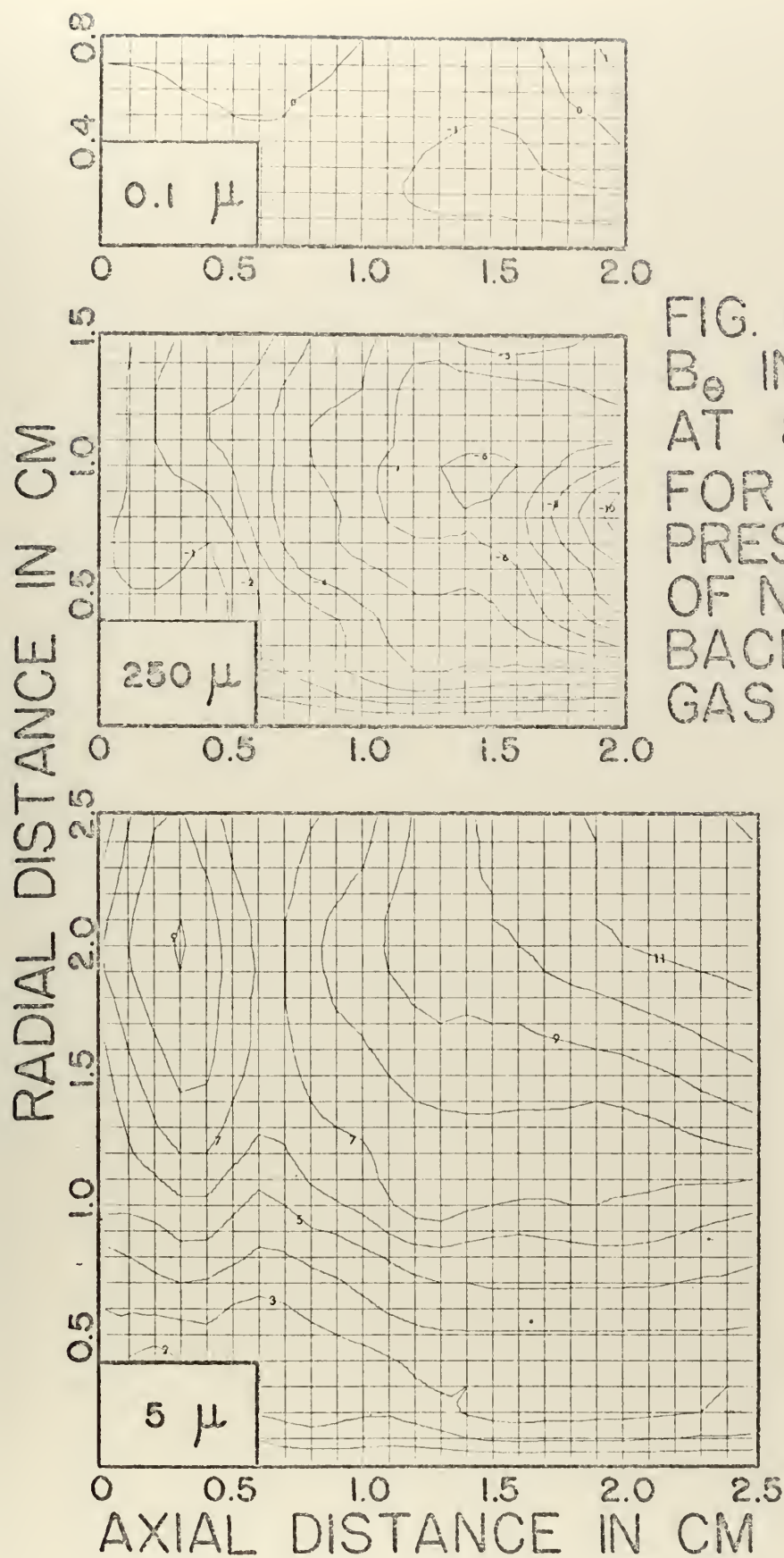


FIG. 40
 B_0 IN GAUSS
 AT 800 NSEC
 FOR VARIOUS
 PRESSURES
 OF NITROGEN
 BACKGROUND
 GAS.

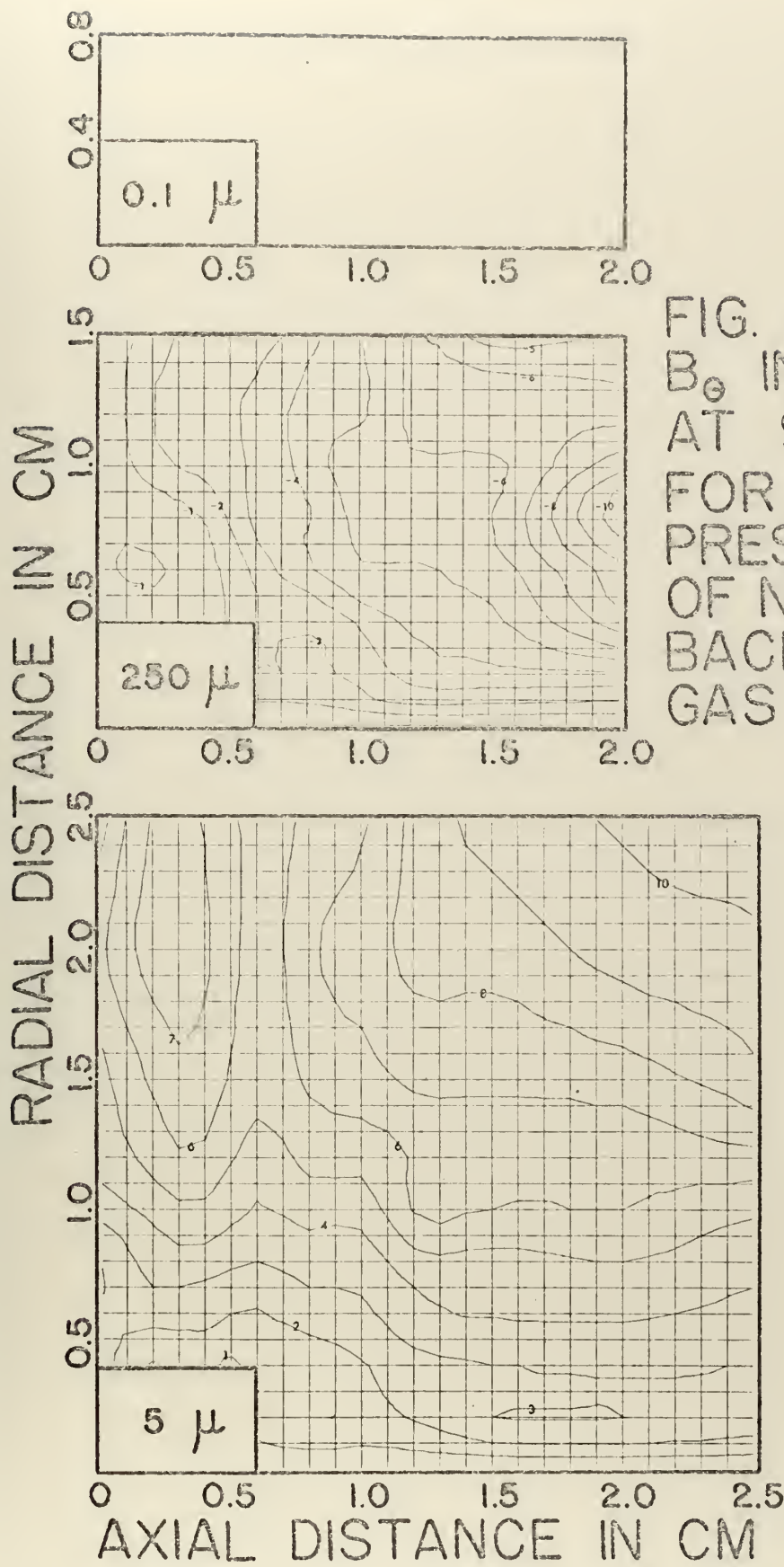


FIG. 41
 B_0 IN GAUSS
 AT 900 NSEC
 FOR VARIOUS
 PRESSURES
 OF NITROGEN
 BACKGROUND
 GAS.

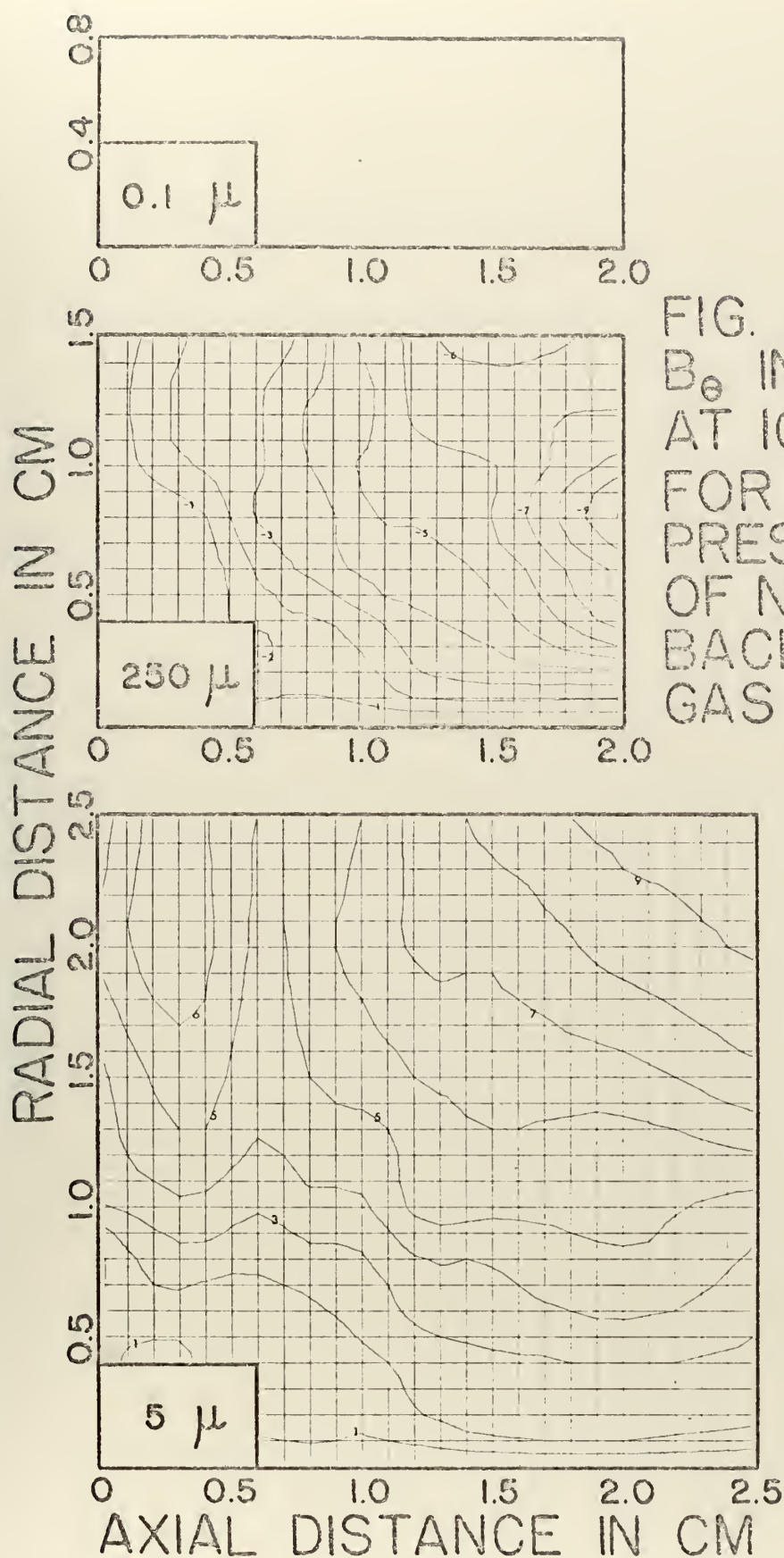


FIG. 42
 B_z IN GAUSS
 AT 1000 NSEC
 FOR VARIOUS
 PRESSURES
 OF NITROGEN
 BACKGROUND
 GAS.

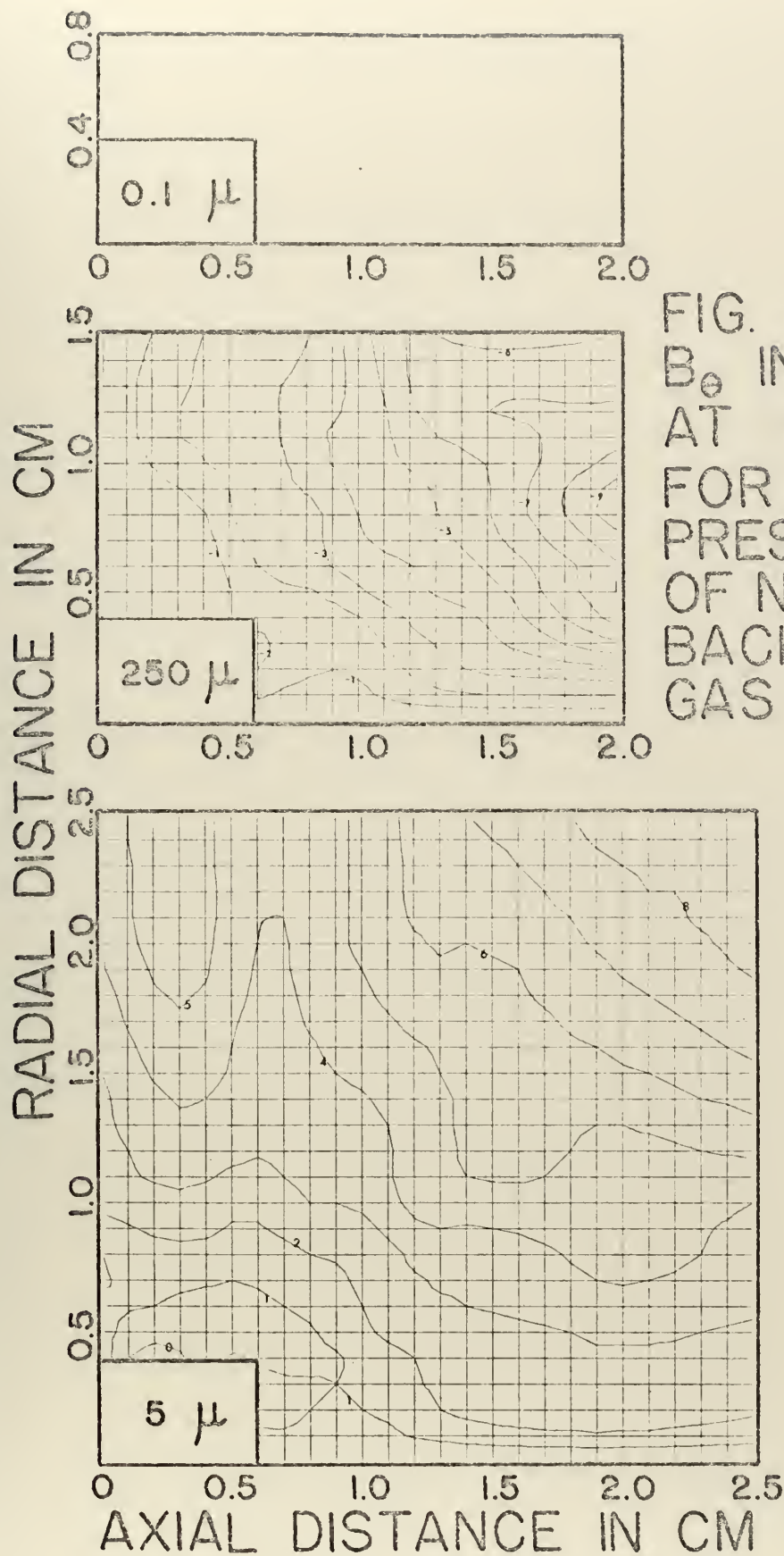


FIG. 43
 B_0 IN GAUSS
 AT 1100 NSEC
 FOR VARIOUS
 PRESSURES
 OF NITROGEN
 BACKGROUND
 GAS.

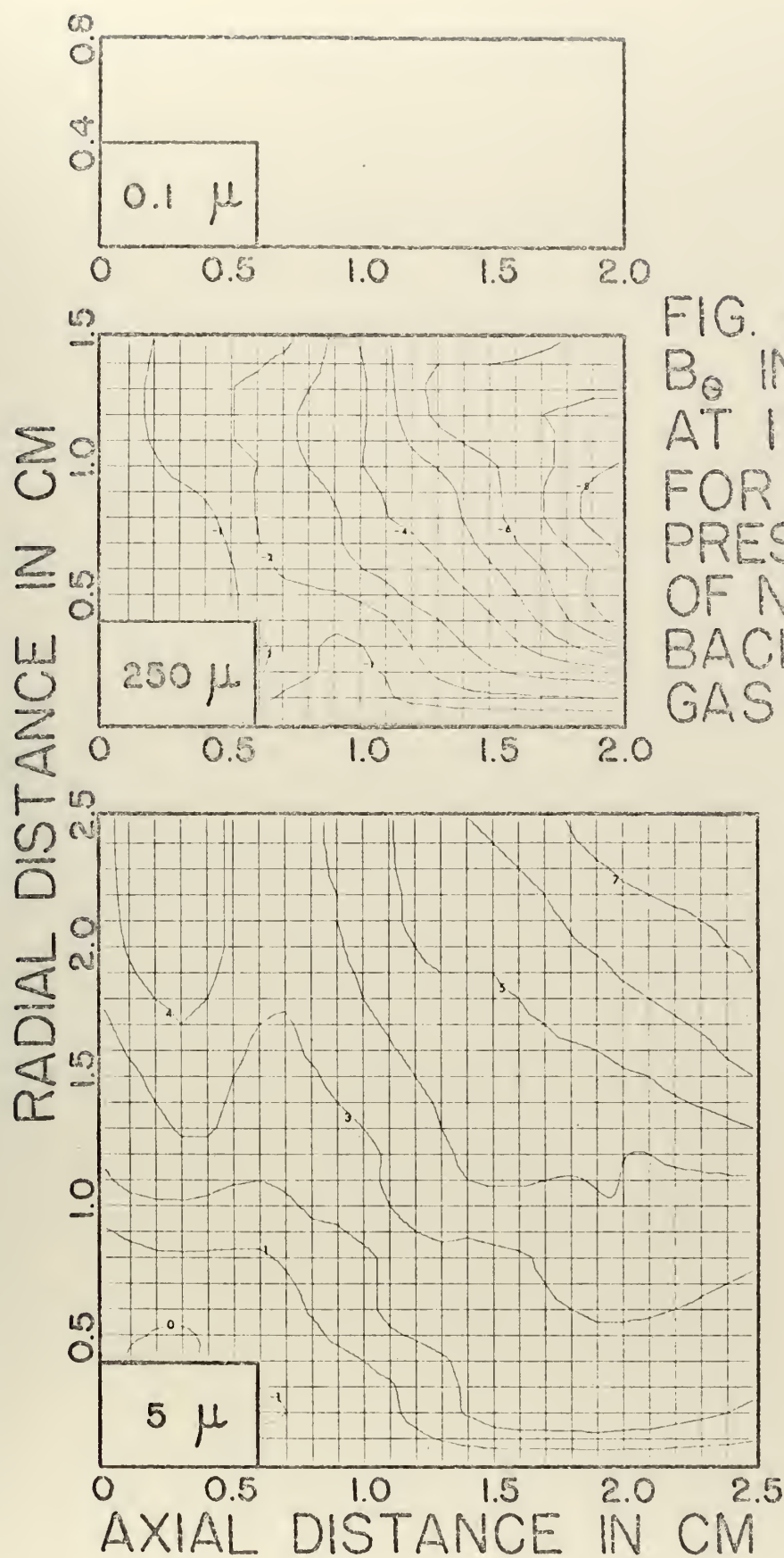


FIG. 44
 B_z IN GAUSS
 AT 1200 NSEC
 FOR VARIOUS
 PRESSURES
 OF NITROGEN
 BACKGROUND
 GAS.

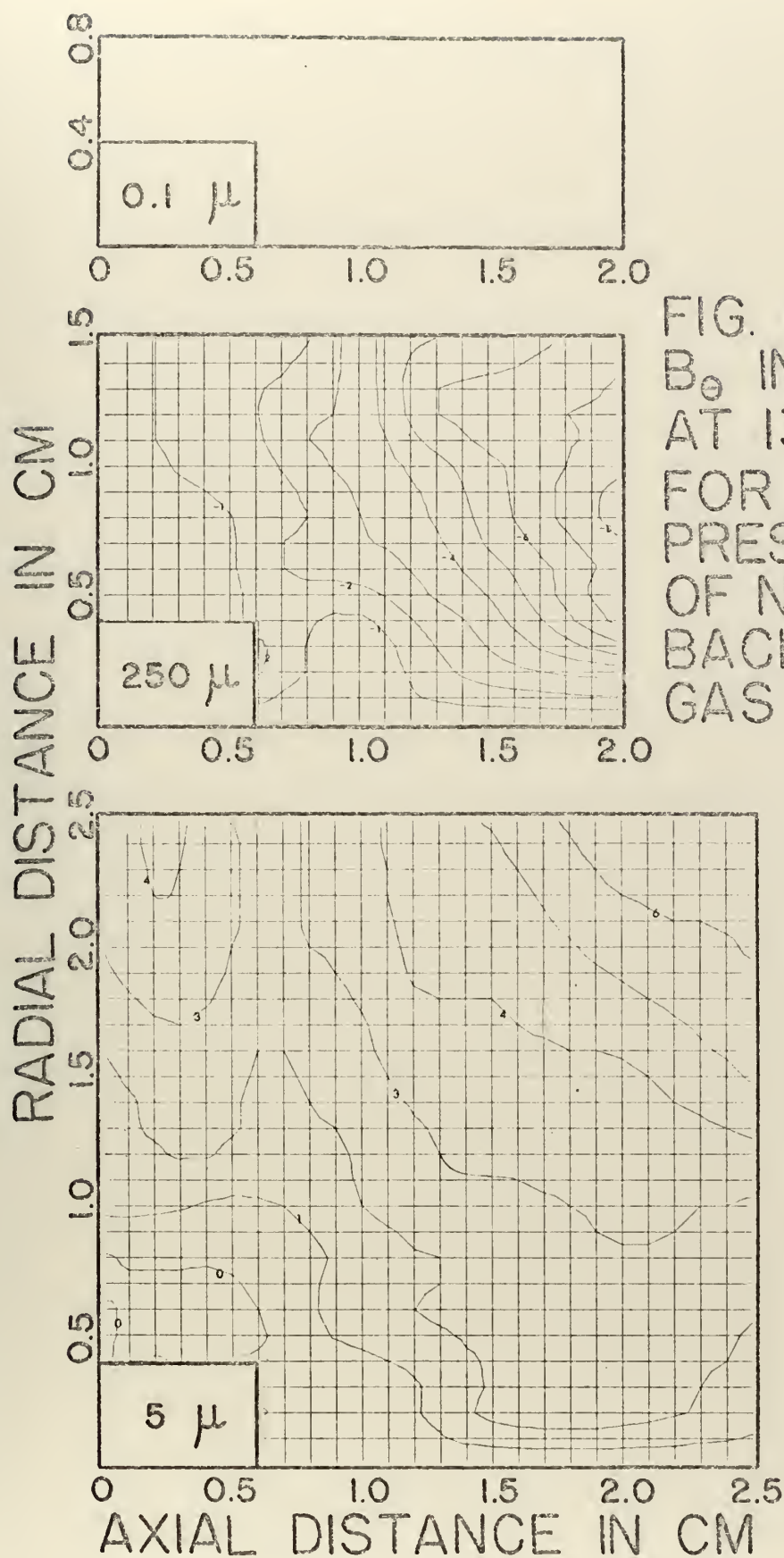


FIG. 45
 B_0 IN GAUSS
 AT 1300 NSEC
 FOR VARIOUS
 PRESSURES
 OF NITROGEN
 BACKGROUND
 GAS.

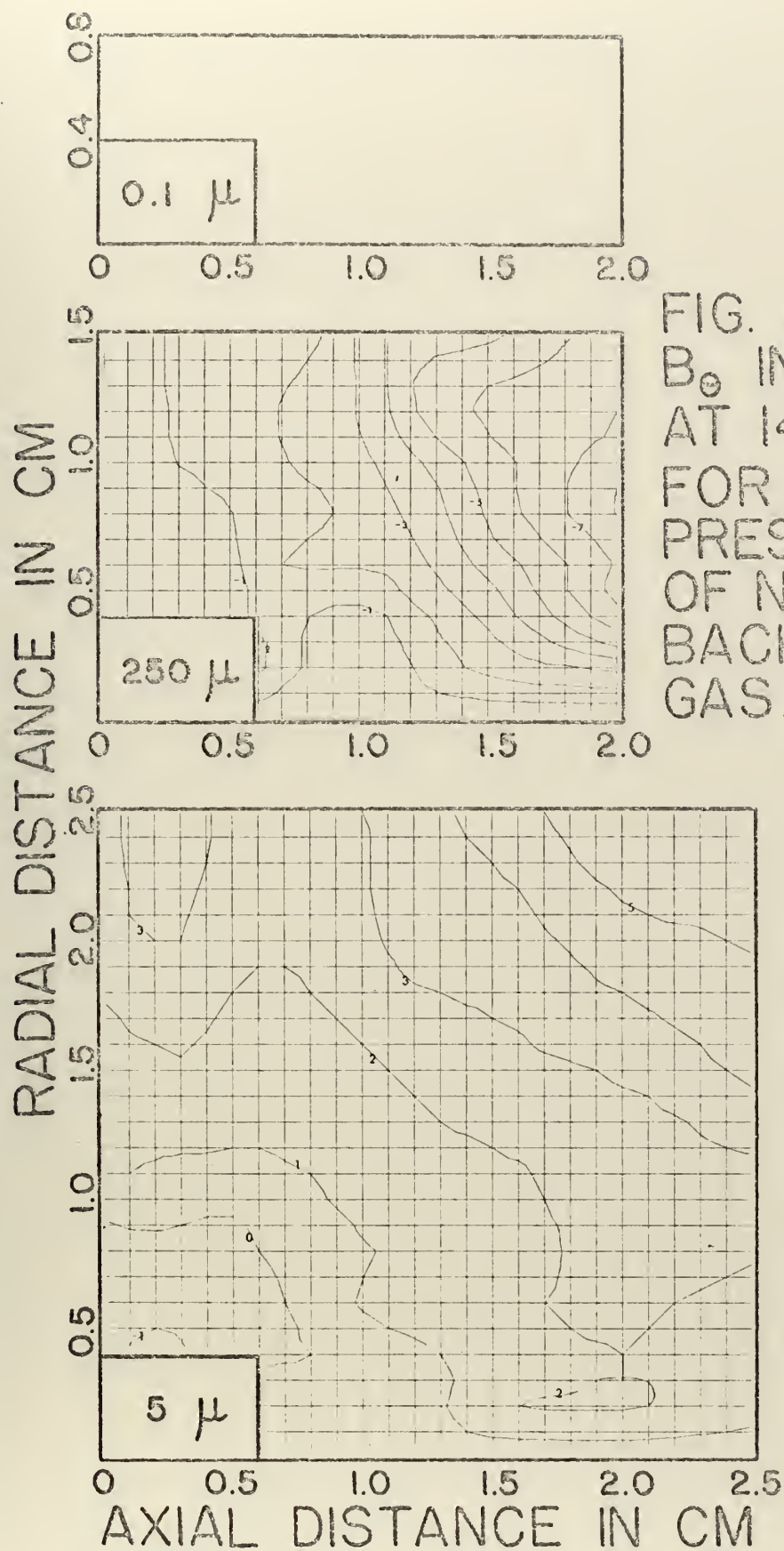


FIG. 46
 B_0 IN GAUSS
 AT 1400 NSEC
 FOR VARIOUS
 PRESSURES
 OF NITROGEN
 BACKGROUND
 GAS.

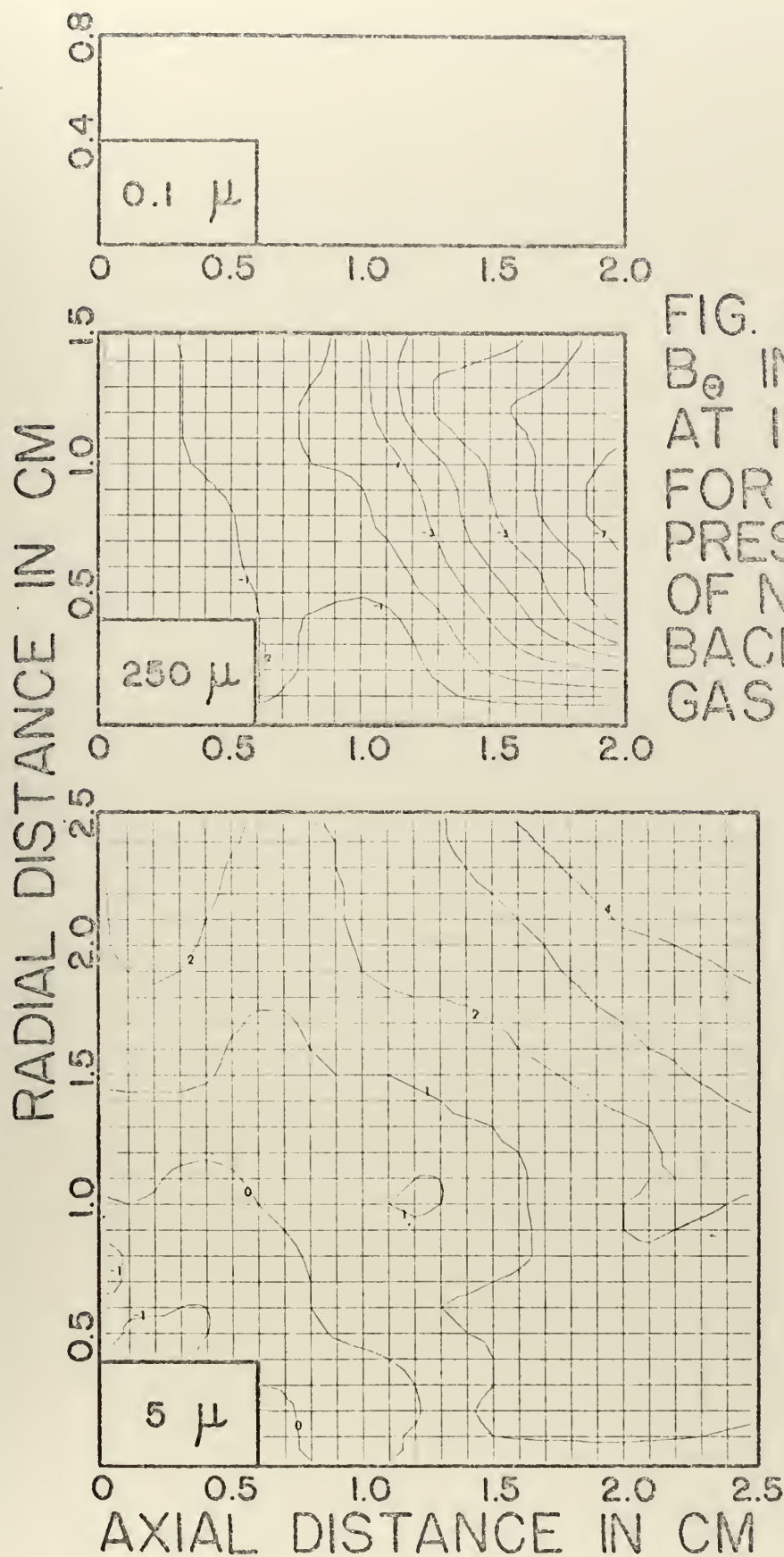


FIG. 47
 B_0 IN GAUSS
 AT 1500 NSEC
 FOR VARIOUS
 PRESSURES
 OF NITROGEN
 BACKGROUND
 GAS.

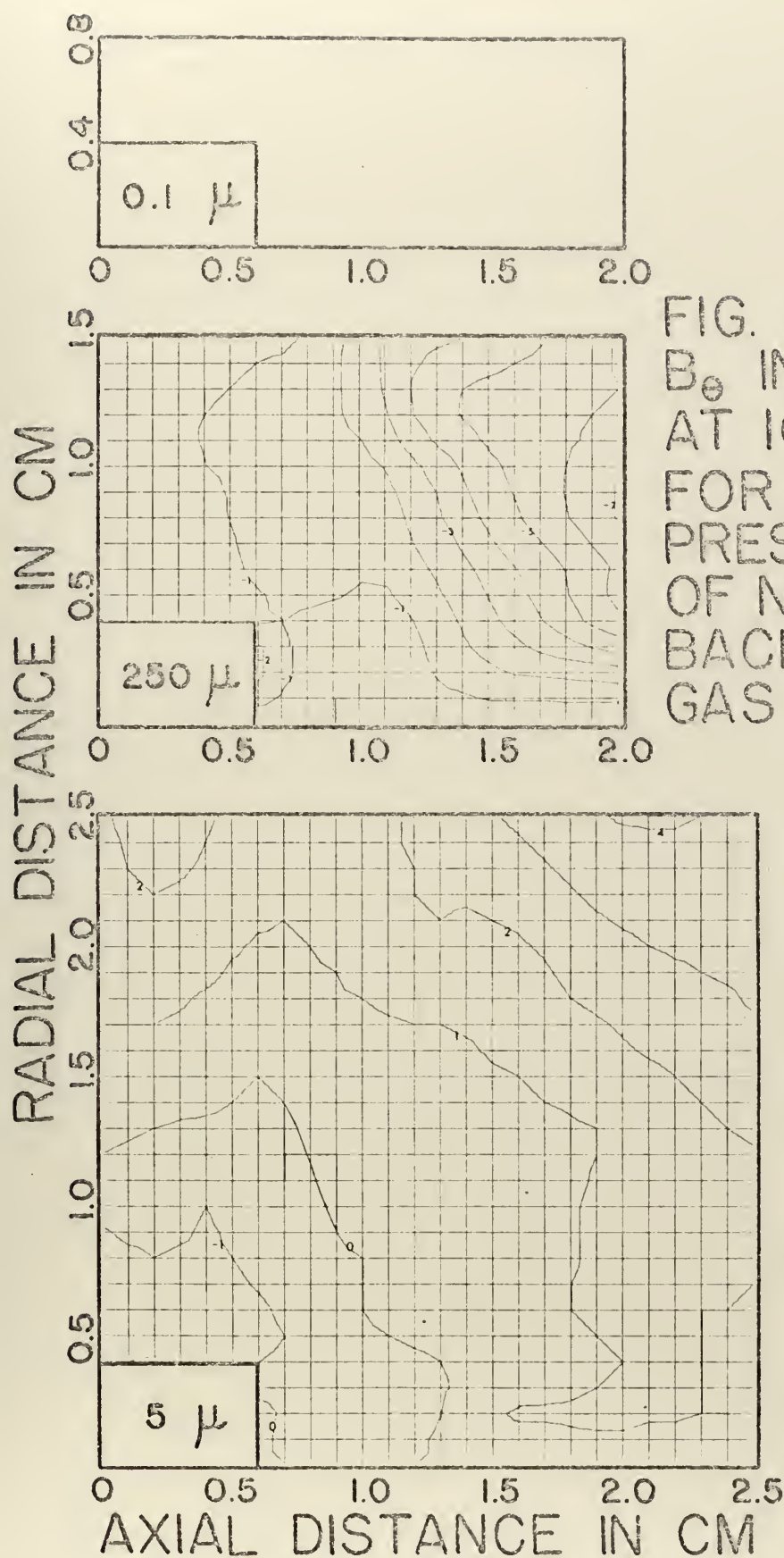


FIG. 48
 B_0 IN GAUSS
 AT 1600 NSEC
 FOR VARIOUS
 PRESSURES
 OF NITROGEN
 BACKGROUND
 GAS.

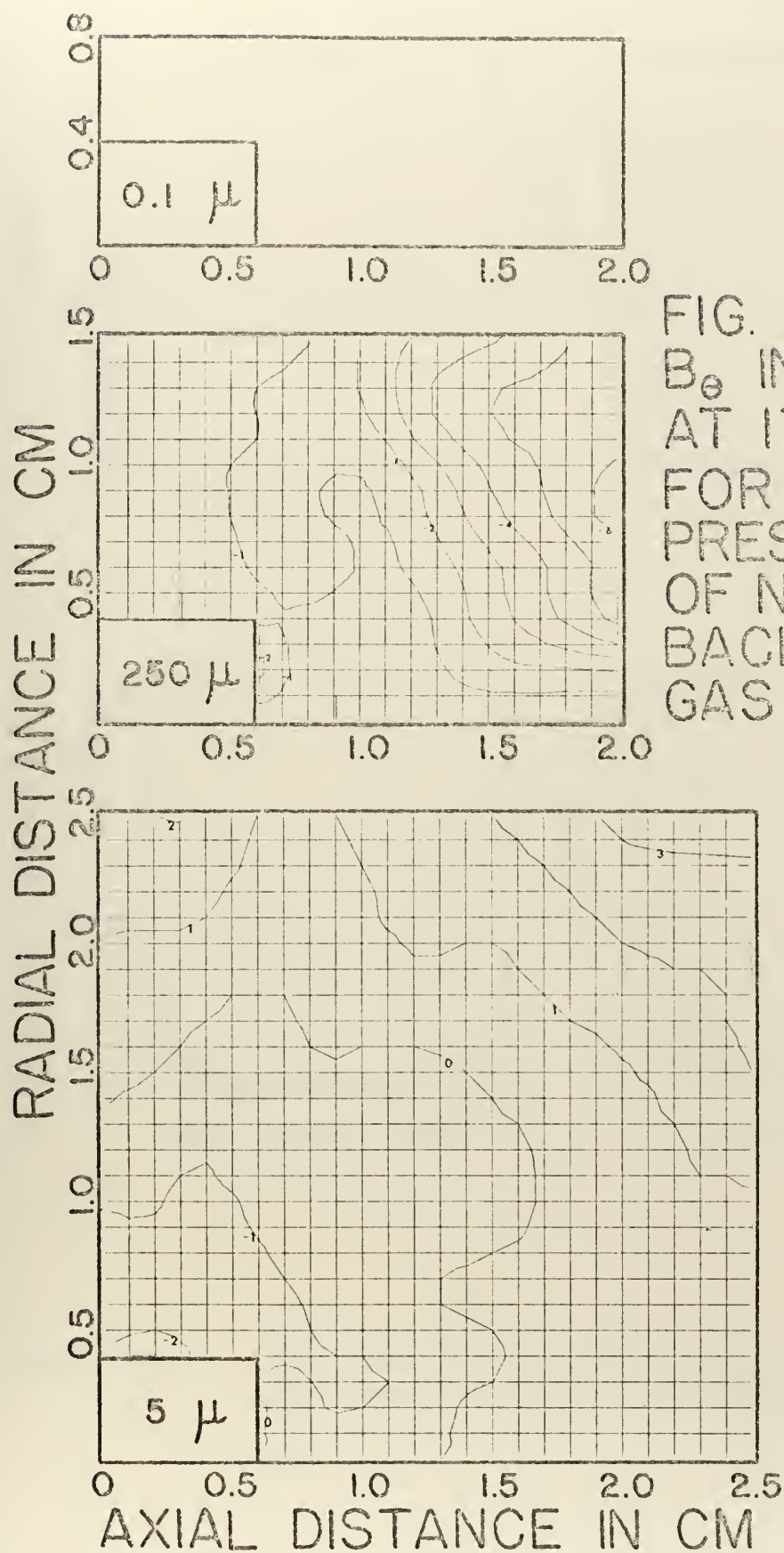


FIG. 49
 B_z IN GAUSS
 AT 1700 NSEC
 FOR VARIOUS
 PRESSURES
 OF NITROGEN
 BACKGROUND
 GAS.

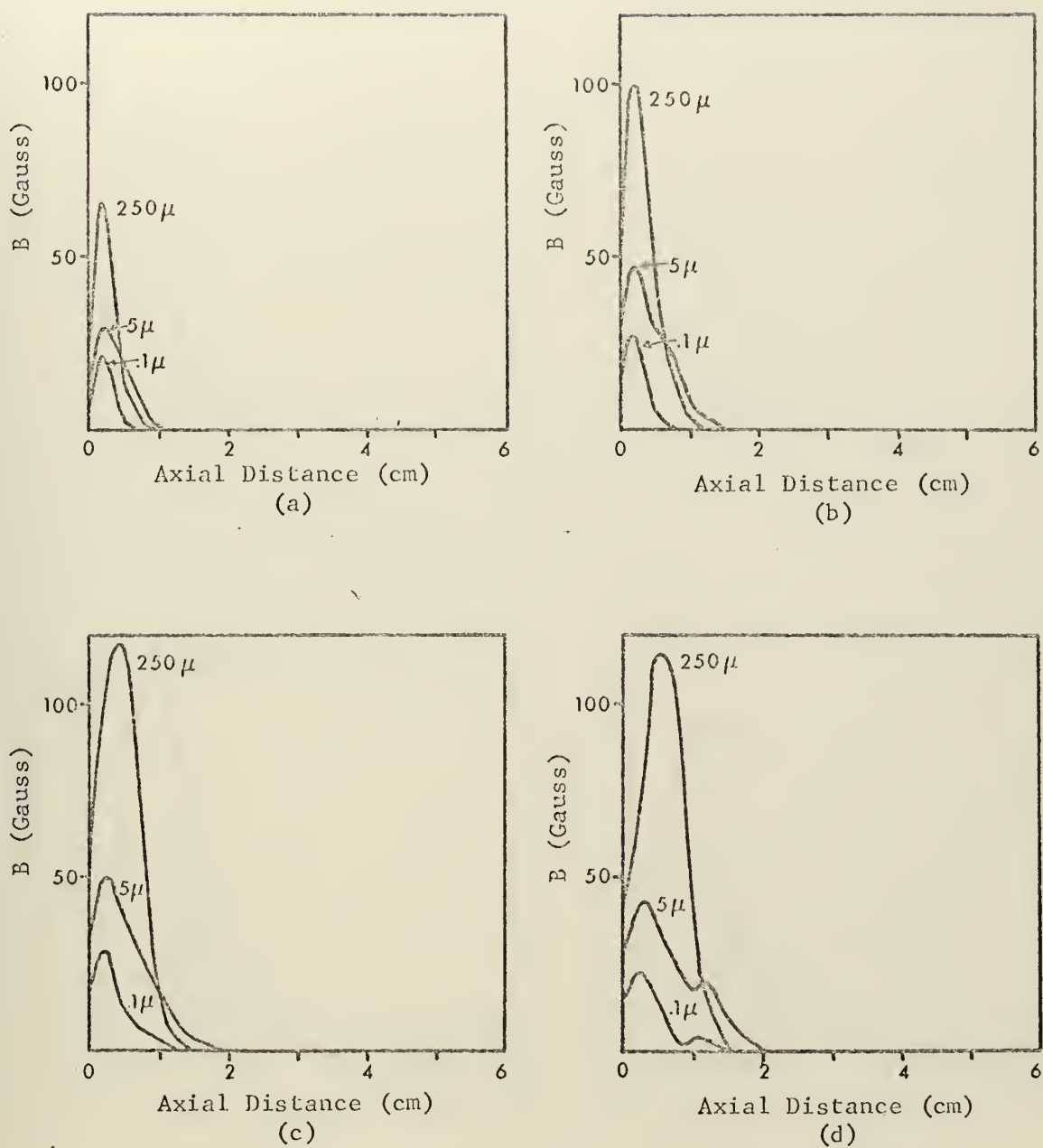


Figure 50. Axial variation of B_0 along $r=4$ mm, $\theta=0^\circ$ at (a) 0 nsec, (b) 20 nsec, (c) 40 nsec, (d) 60 nsec, for different pressures of nitrogen background gas.

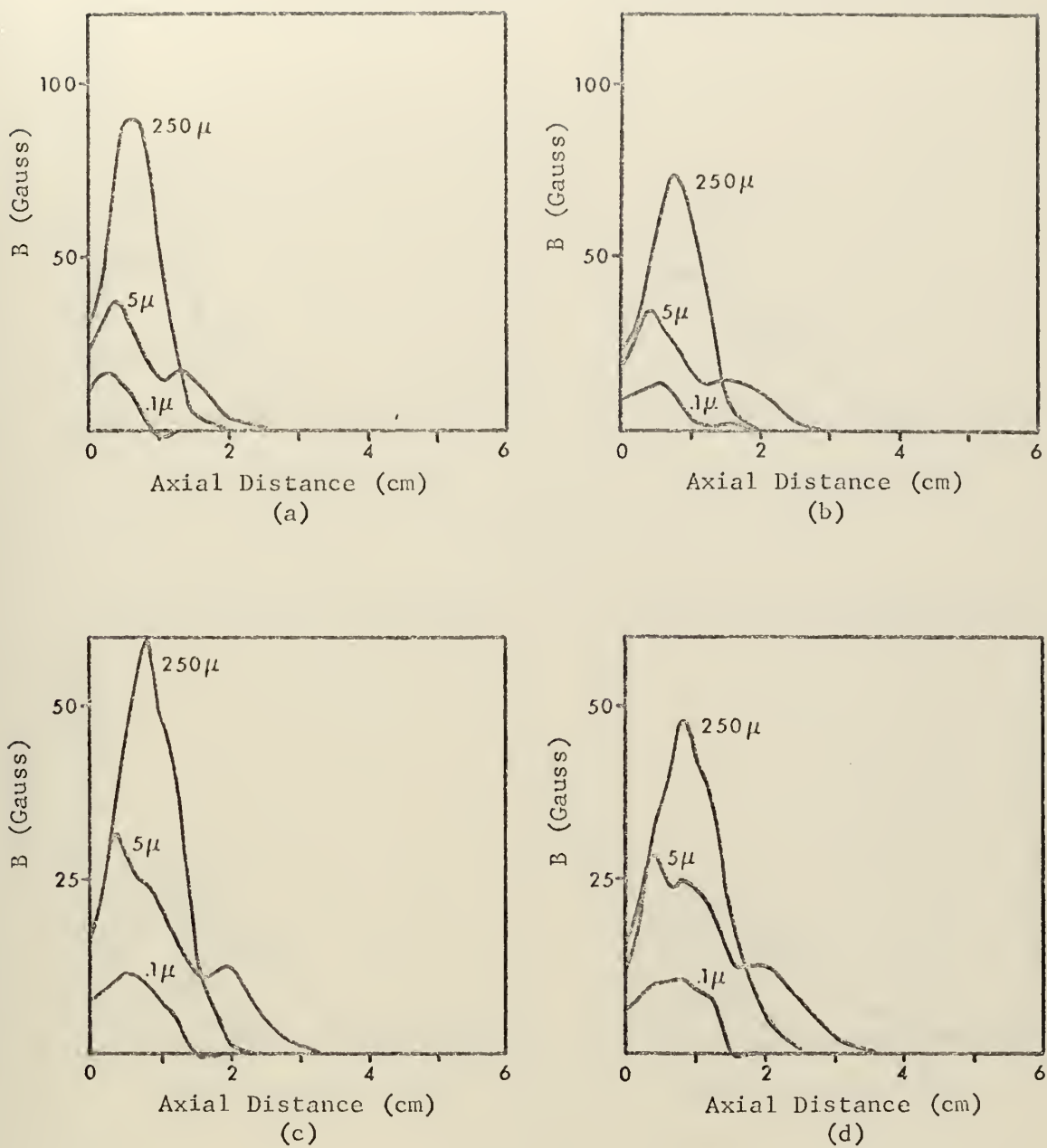


Figure 51.

Axial variation of B_0 along $r=4\text{ mm}$, $\theta=0^\circ$ at
 (a) 80 nsec, (b) 100 nsec, (c) 120 nsec, (d) 140
 nsec, for different pressures of nitrogen background
 gas.

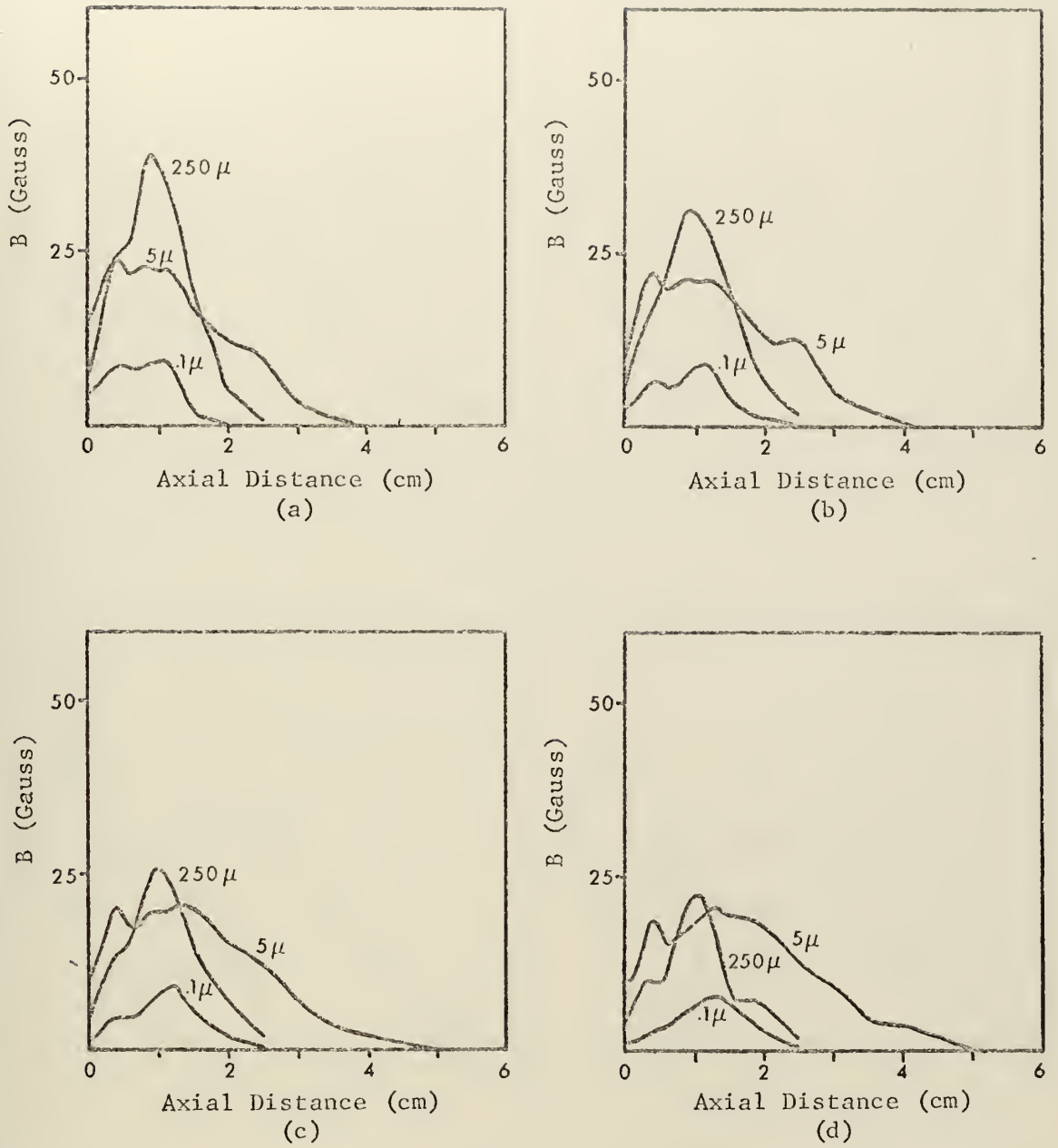


Figure 52.

Axial variation of B_0 along $r=4\text{ mm}$, $\theta=0^\circ$ at
 (a) 160 nsec, (b) 180 nsec, (c) 200 nsec, (d) 220
 nsec, for different pressures of nitrogen background
 gas.

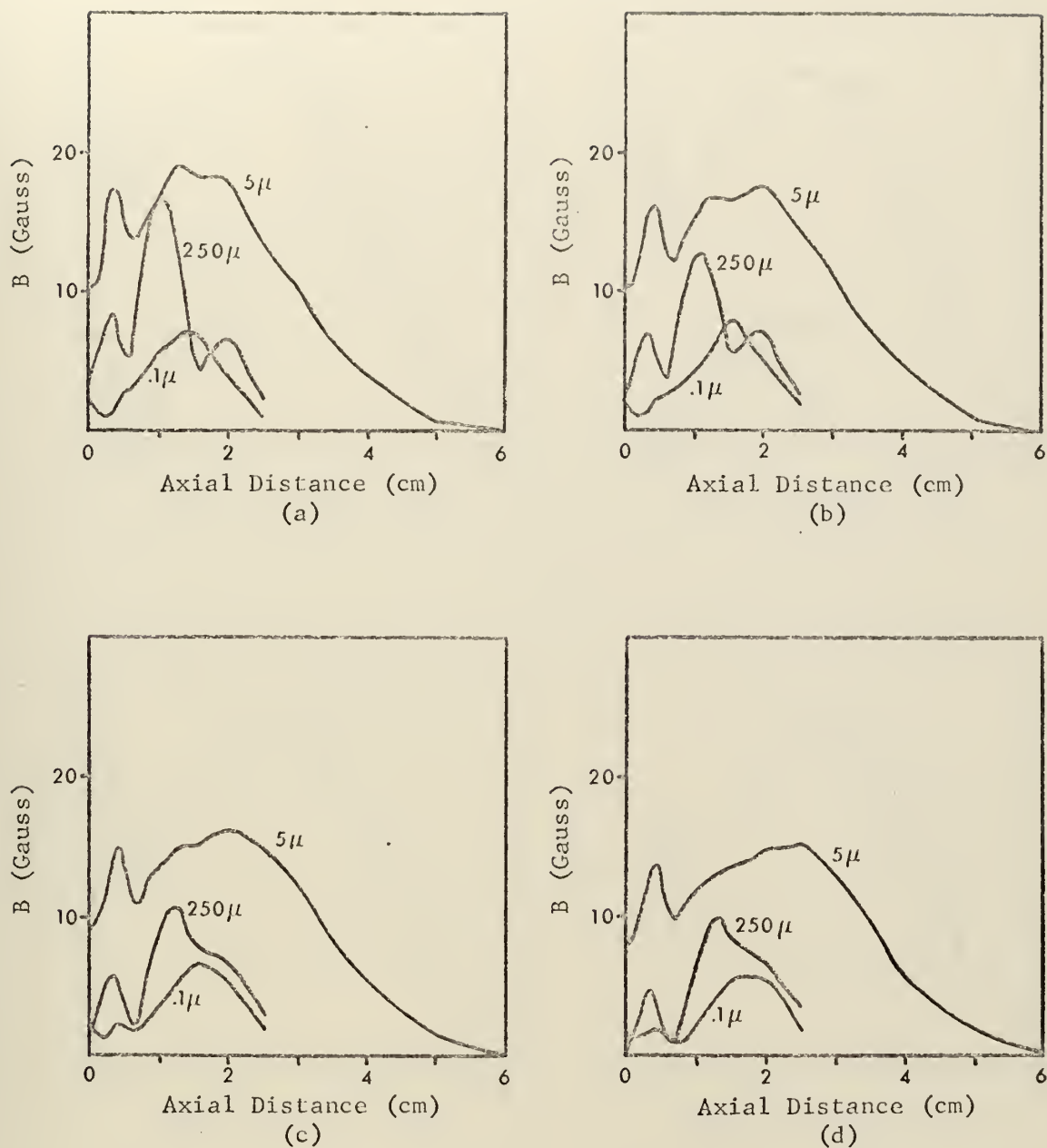


Figure 53.

Axial variation of B_0 along $r=4$ mm, $\theta=0^\circ$ at
 (a) 240 nsec, (b) 260 nsec, (c) 280 nsec, (d) 300
 nsec, for different pressures of nitrogen background
 gas.

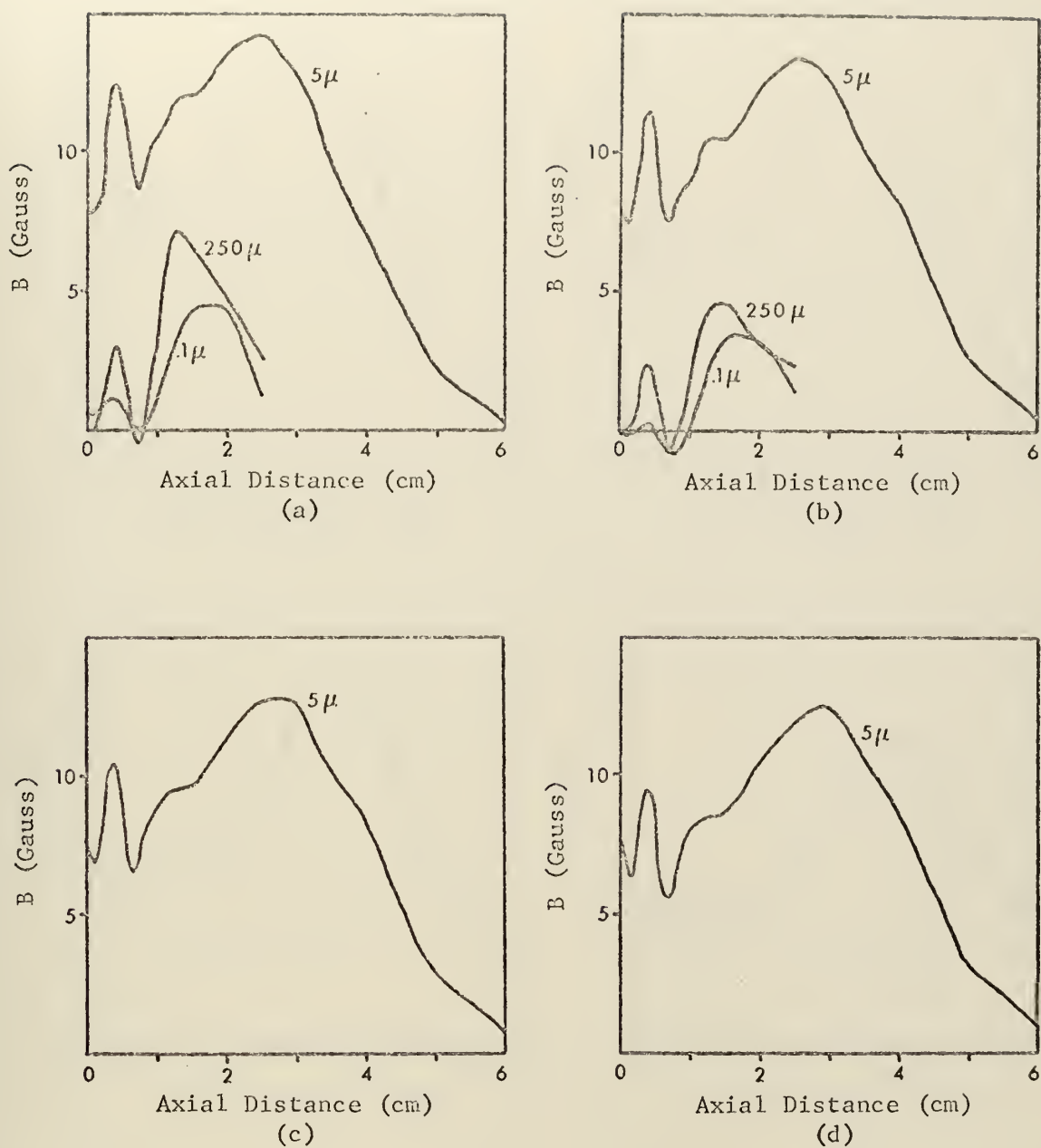


Figure 54. Axial variation of B_θ along $r=4$ mm, $\theta=0^\circ$ at (a) 320 nsec, (b) 340 nsec, (c) 360 nsec, (d) 380 nsec, for different pressures of nitrogen background gas.

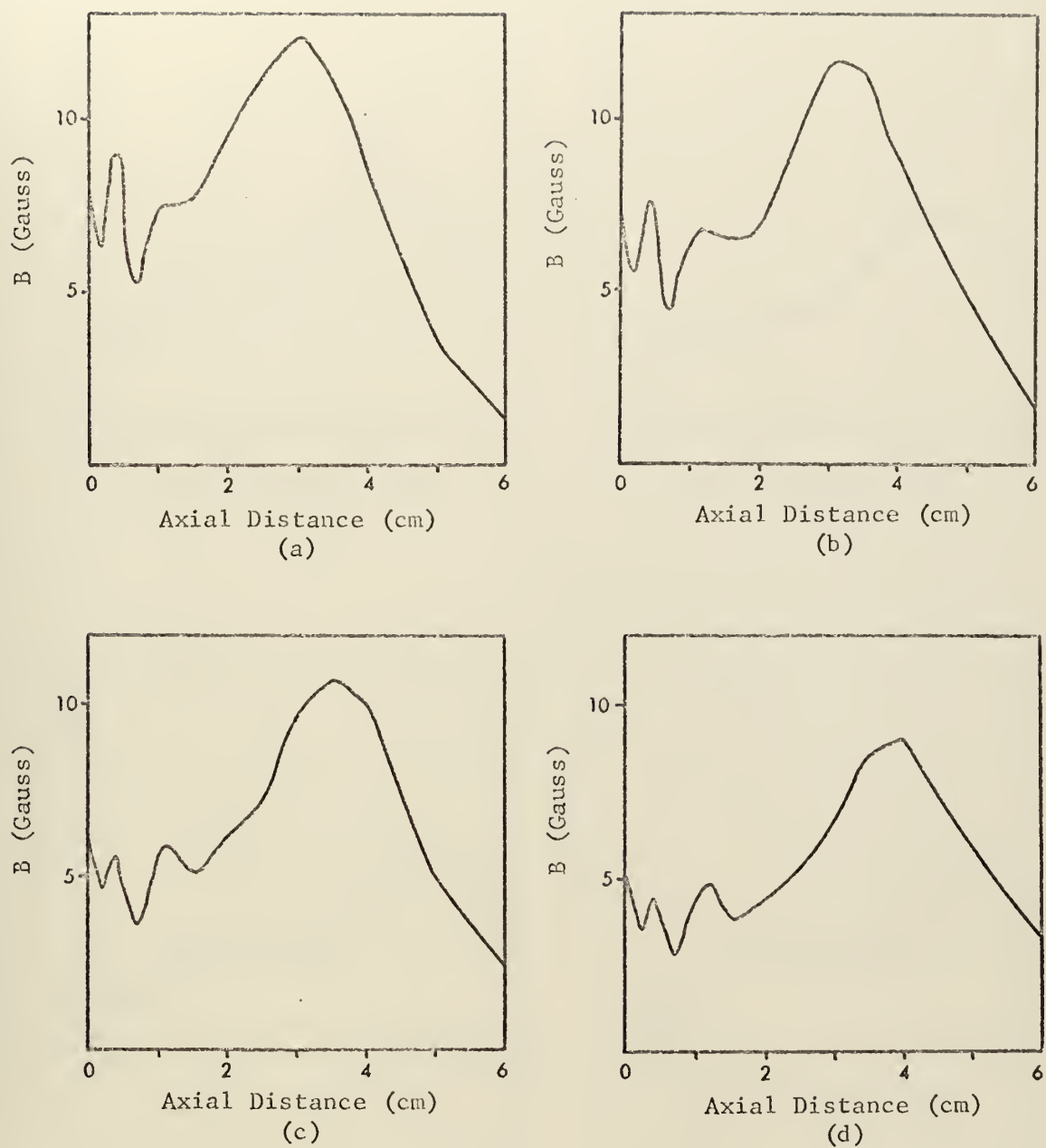


Figure 55. Axial variation of B_0 along $r=4$ mm, $\theta=0^\circ$ at (a) 400 nsec, (b) 440 nsec, (c) 500 nsec, (d) 600 nsec, for 5 mTorr of nitrogen background gas.

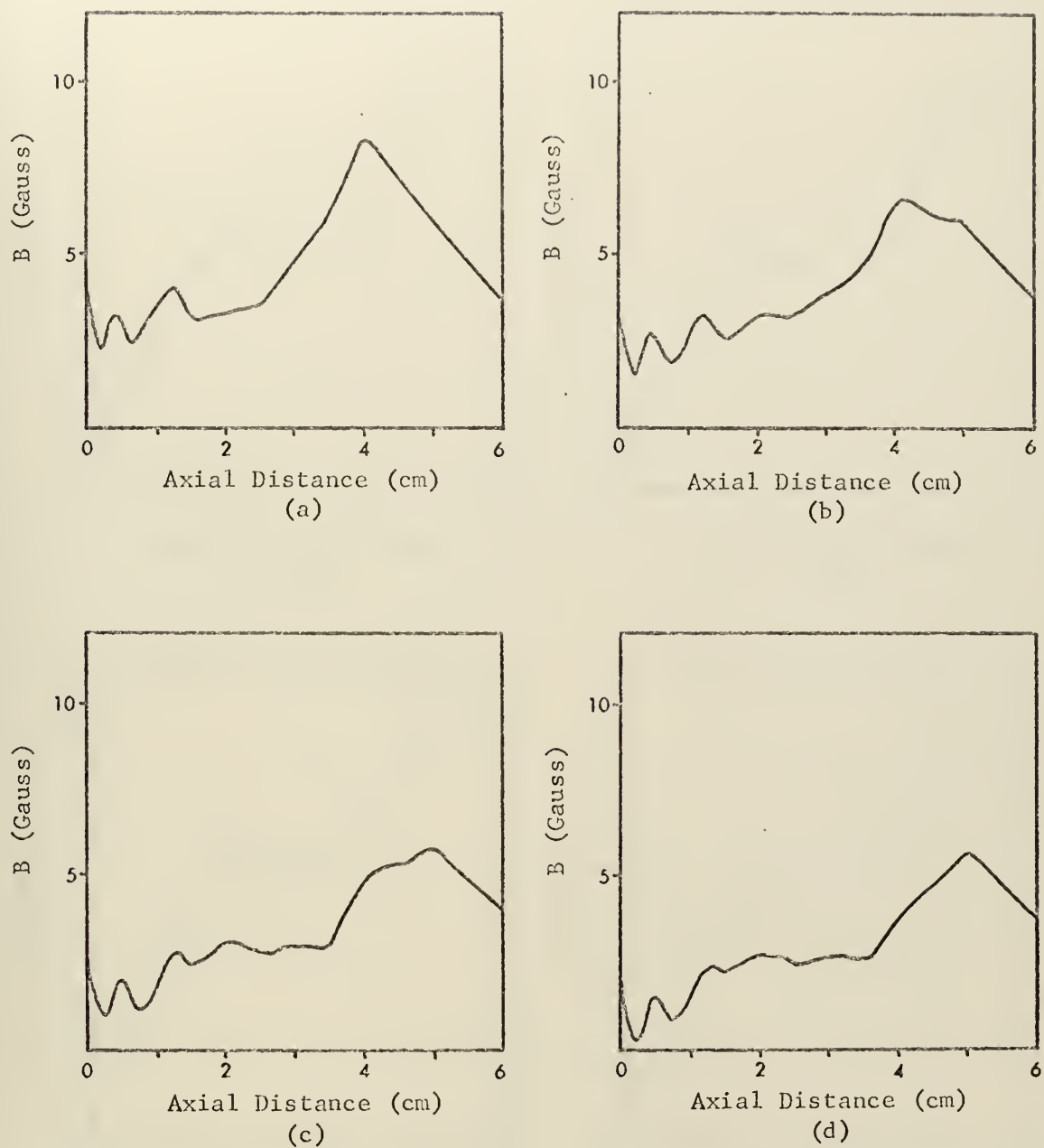


Figure 56. Axial variation of B_θ along $r=4$ mm, $\theta=0^\circ$ at (a) 700 nsec, (b) 800 nsec, (c) 900 nsec, (d) 1000 nsec, for 5 mTorr of nitrogen background gas.

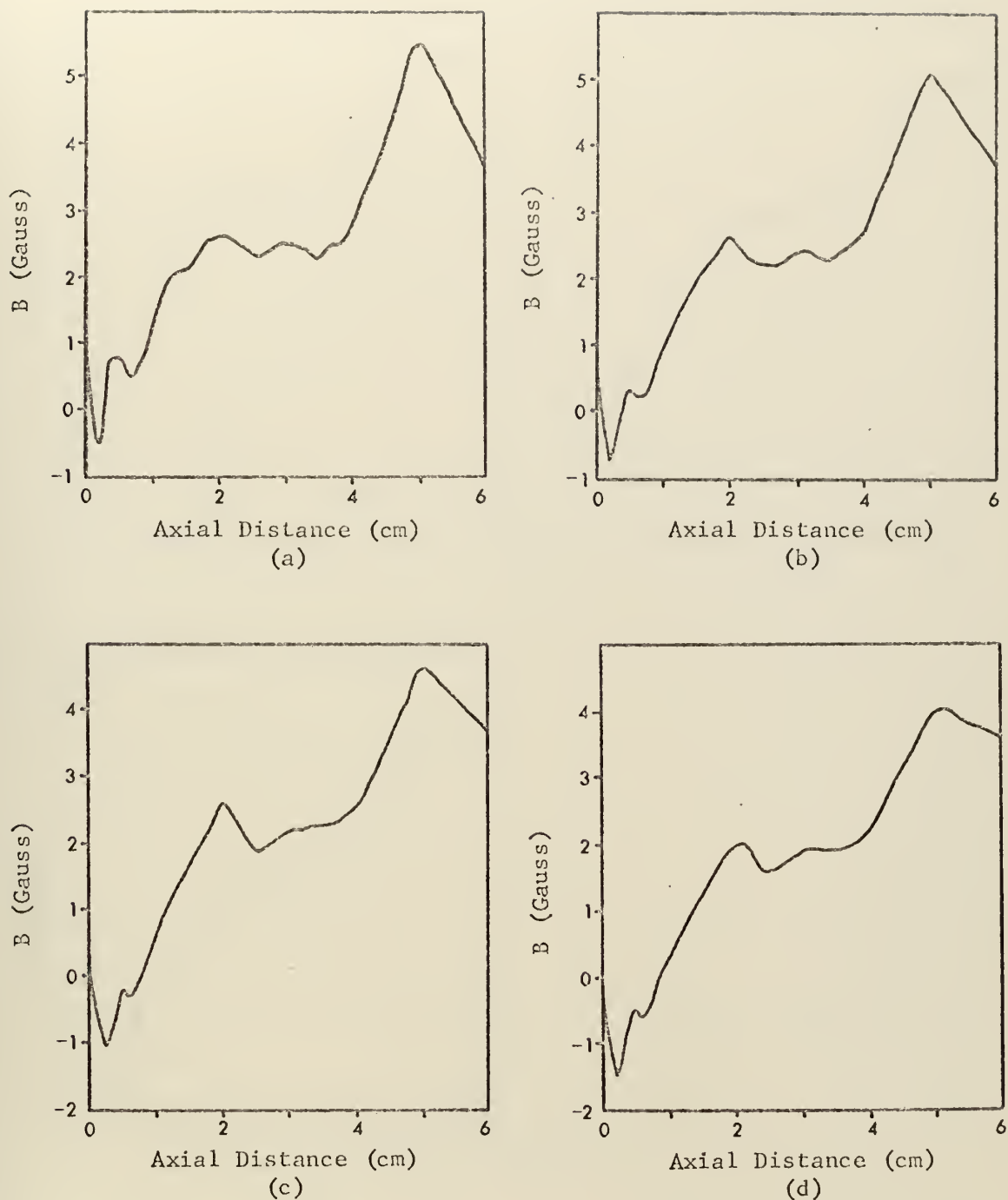


Figure 57.

Axial variation of B_θ along $r=4$ mm, $\theta=0^\circ$ at
 (a) 1100 nsec, (b) 1200 nsec, (c) 1300 nsec,
 (d) 1400 nsec, for 5 mTorr of nitrogen
 background gas.

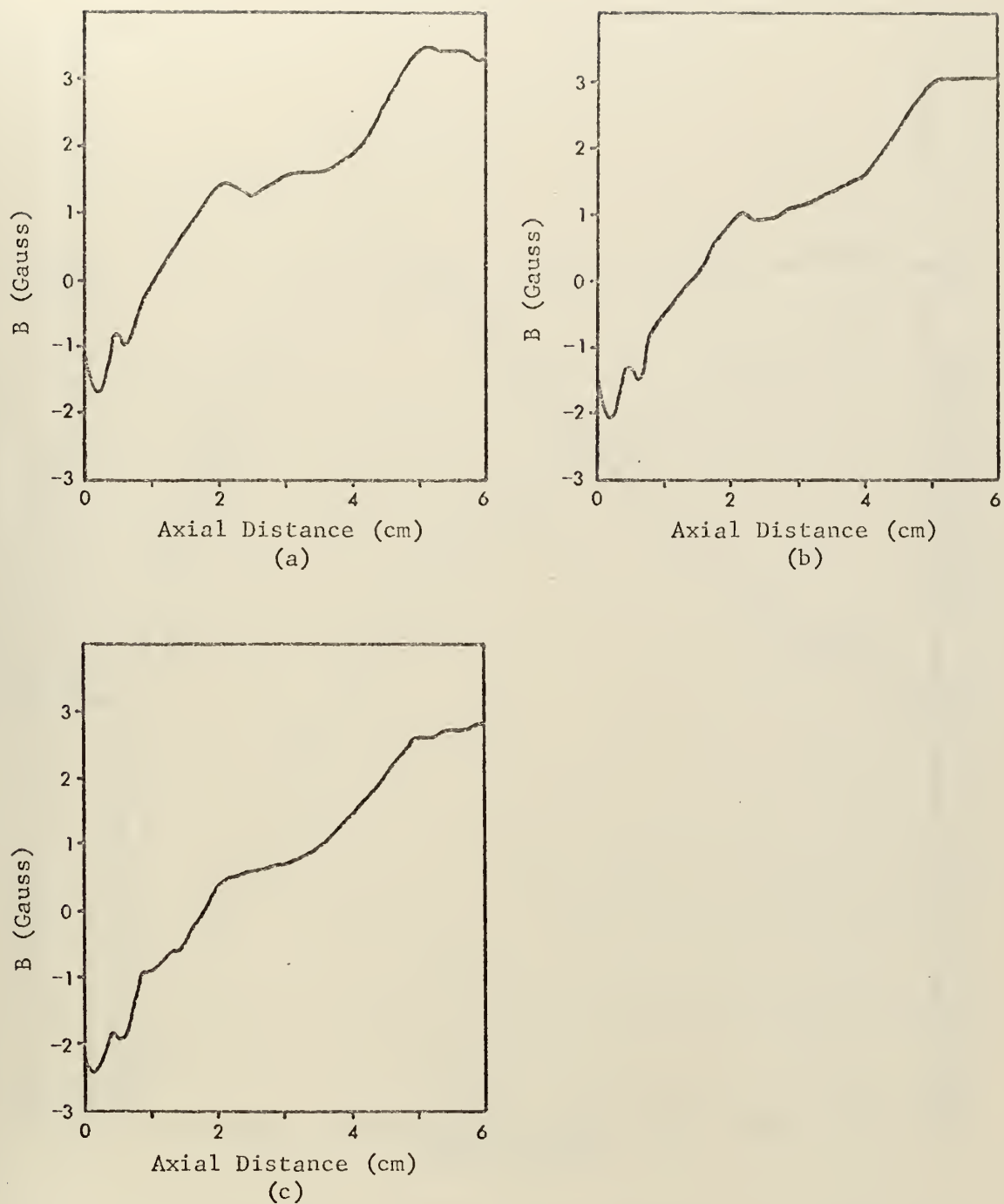


Figure 58. Axial variation of B_θ along $r=4$ mm, $\theta=0^\circ$ at (a) 1500 nsec, (b) 1600 nsec, (c) 1700 nsec, for 5 mTorr of nitrogen background gas.

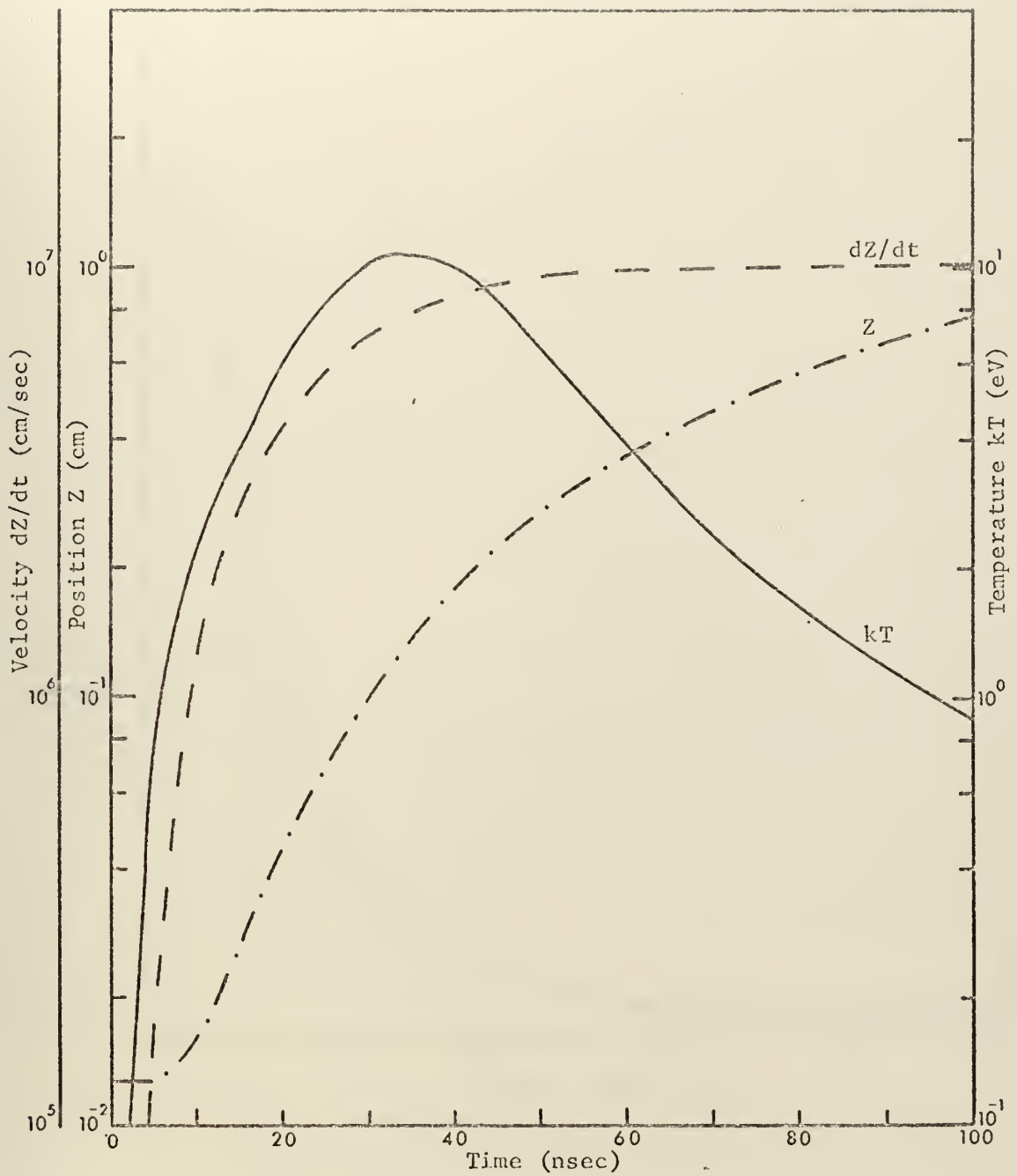


Figure 59. Calculated plasma time history, giving plasma front position, expansion velocity, and temperature as functions of time for a 300 MW Nd laser pulse incident on a .005 in. Mylar foil.

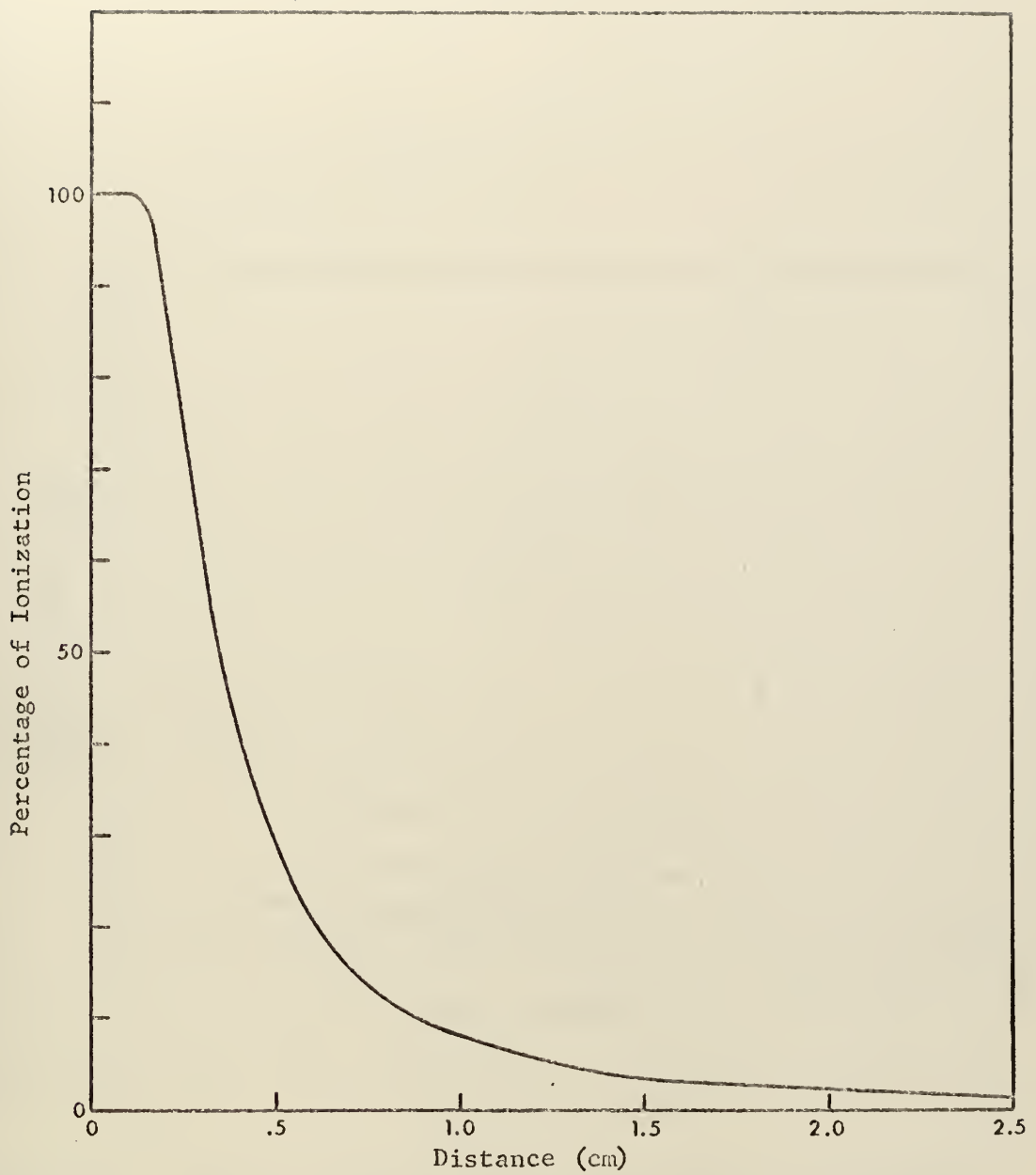


Figure 60. Percentage of single ionization caused by the photoionization of the ambient gas by the Bremsstrahlung radiation of the laser plasma as a function of distance from the laser plasma.

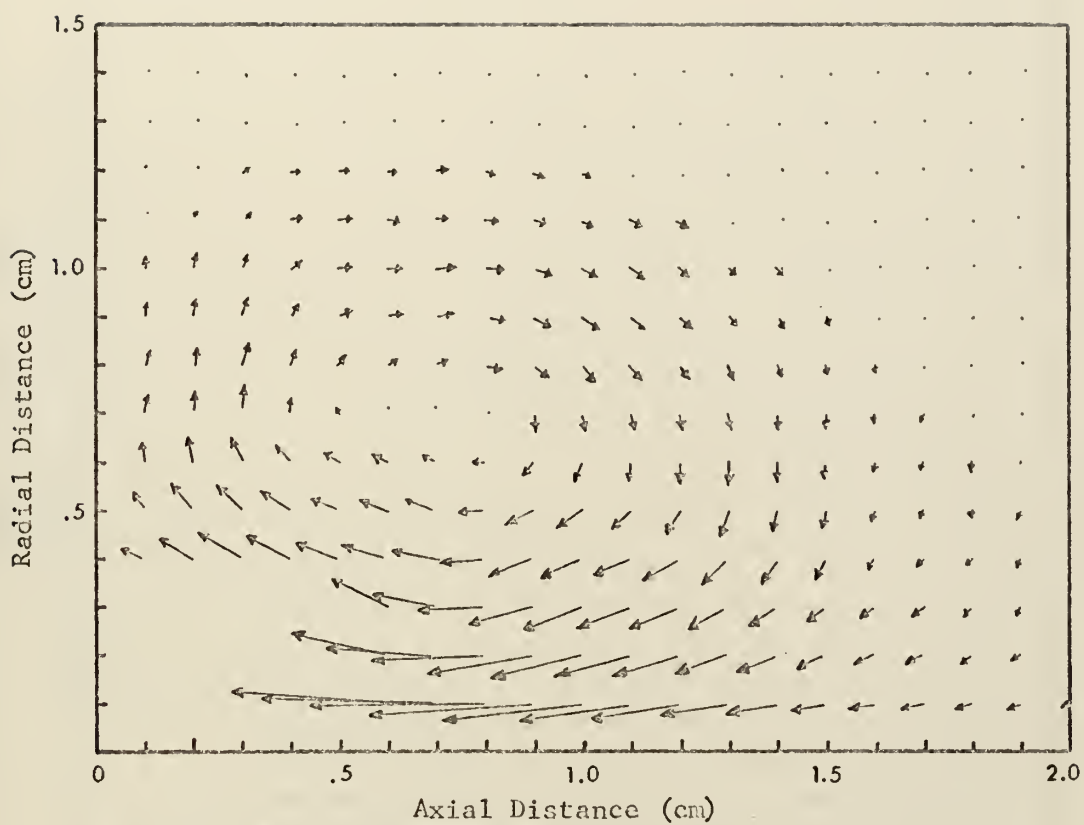


Figure 61. Current density at 120 nsec for 250 mTorr of nitrogen background gas. The magnitude of the largest current density at this time is 612 amp/cm^2 .

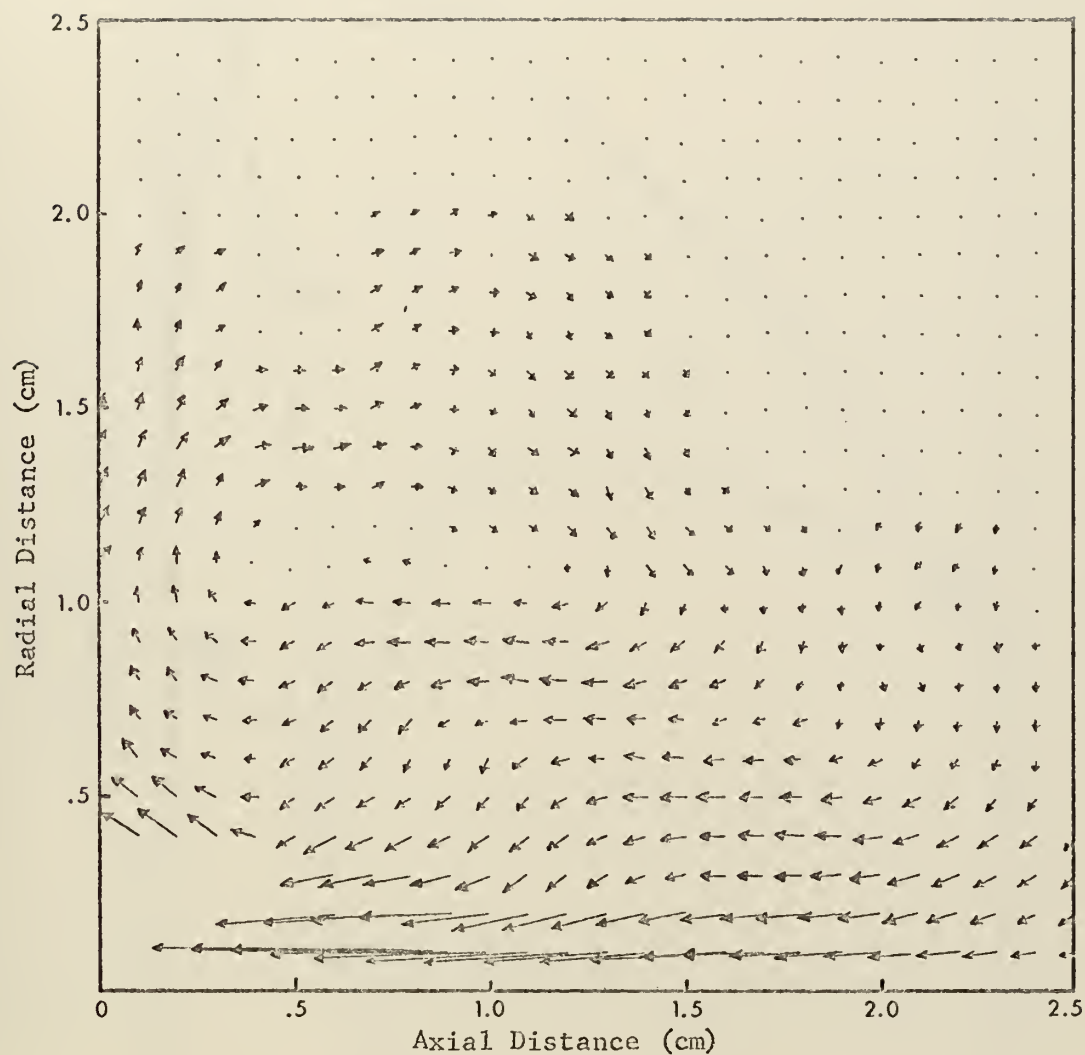


Figure 62. Current density at 120 nsec for 5 mTorr of nitrogen background gas. The magnitude of the largest current density at this time is 369 amp/cm^2 .

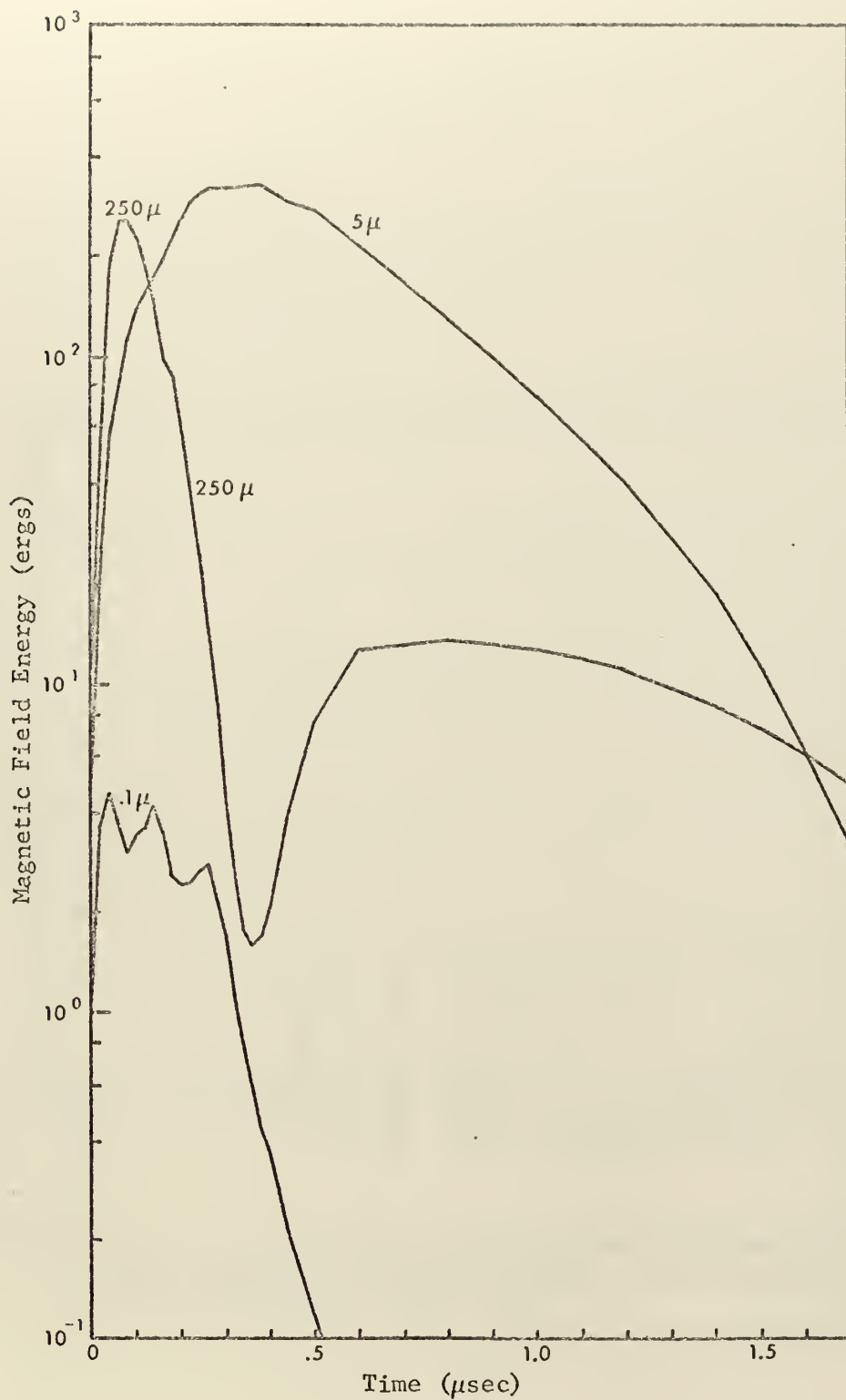


Figure 63. Total energy in the self-generated magnetic field versus time for various pressures of nitrogen background gas.

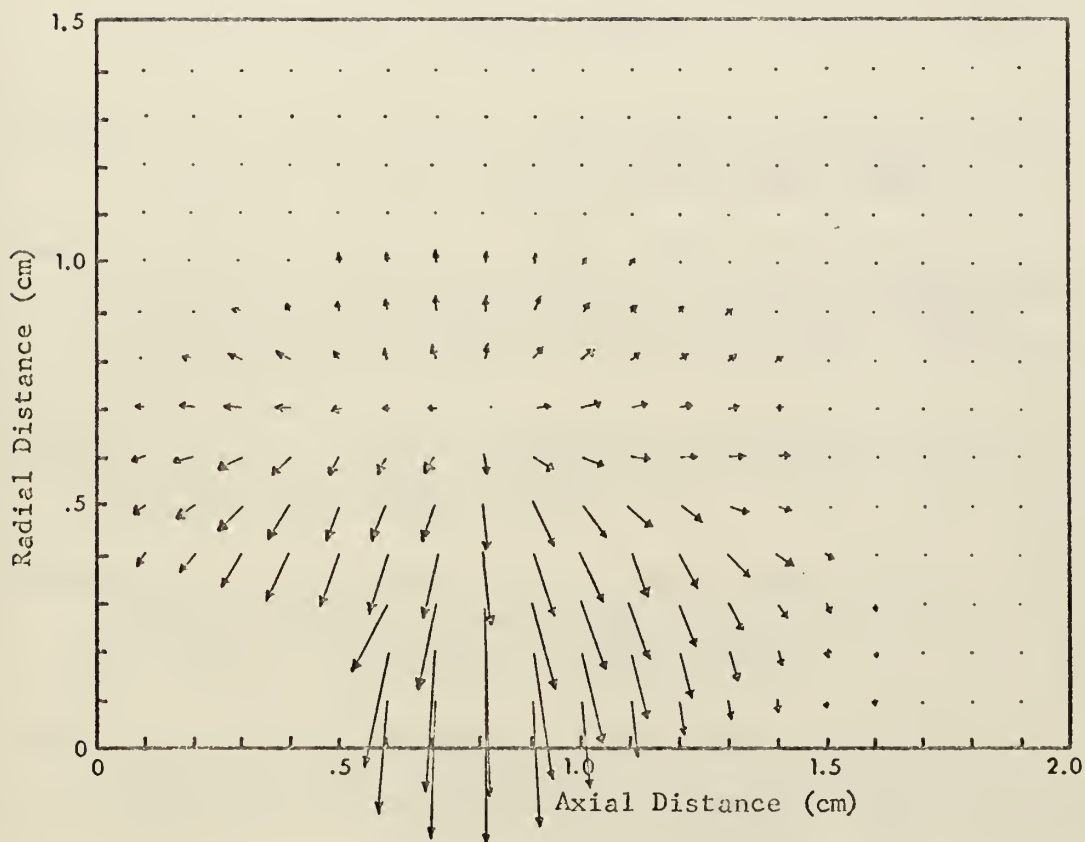


Figure 64. $\vec{J} \times \vec{B}$ force density at 120 nsec for 250 mTorr of nitrogen background gas. The magnitude of the largest force at this time is 1.40×10^4 nt/m³.

BIBLIOGRAPHY

1. DeMichelis, C., "Laser-Interaction with Solids--A Bibliographical Review," IEEE Journal of Quantum Electronics, v. 6, no. 10, pp. 630-641, October 1970.
- ✓ 2. Korobkin, V. V. and Serov, R. V., "Investigation of the Magnetic Field of a Spark Produced by Focusing Laser Radiation," JETP Letters, v. 4, no. 3, pp. 103-106, 1 August 1966.
- ✓ 3. Stamper, J.A. and others, "Spontaneous Magnetic Fields in Laser-Produced Plasmas," Phys. Rev. Letters, v. 26, no. 17, pp. 1012-1015, 26 April 1971.
4. Basov, N.G. and Krokhin, O. N., "The Condition of Plasma Heating by the Optical Generator Radiation," in Quantum Electronics, vol. 3, Grivet, P. and Bloembergen, N., Eds., p. 1373, Columbia University Press, 1964.
5. Dawson, J. M., "On the Production of Plasma by Giant Pulse Laser," Phys. Fluids, vol. 7, no. 7, pp. 981-987, July 1964.
6. Haught, A. F. and Polk, D. H., "High-Temperature Plasmas Produced by Laser Beam Irradiation of Single Solid Particles," Phys. Fluids, vol. 9, no. 10, pp. 2047-2056, October 1966.
7. Dawson, J. M. and Oberman, C. R., "High-Frequency Conductivity and the Emission and Absorption Coefficients of a Fully Ionized Plasma," Phys. Fluids, vol. 5, no. 5, pp. 517-524, May 1962.
8. Spitzer, L., Jr., Physics of Fully Ionized Gases, 2d Edition, pp. 127, 40-41, and 148, Interscience Publishers, Inc., 1962.
9. Ready, J. F., Effects of High-Power Laser Radiation, pp. 165 and 196-201, Academic Press, 1971.
10. Papadopoulos, K. and others, "Heating of Counter-streaming Ion Beams in an External Magnetic Field," Phys. Fluids, v. 14, no. 4, pp. 849-857, April 1971.

11. Naval Research Laboratory Report 7301, Demonstration of Collisionless Interactions Between Counterstreaming Ions in a Laser-Produced Plasma Experiment, by S. O. Dean, 17 September 1971.
12. Friedman, H. W. and Patrick, R. M., "Momentum Transfer in Plasmas at High Alfvén Mach Numbers," Phys. Fluids, v. 14, no. 9, pp. 1889-1904, September 1971.
13. Davis, L. J., Self-Generated Magnetic Fields Produced by Laser Bombardment of a Solid Target, MS Thesis, Naval Postgraduate School, 1971.
14. Kunihiro, D. M., The Absorption of Laser Radiation by a Laser Produced Plasma, MS Thesis, Naval Postgraduate School, 1972.
15. McLaughlin, T.A., Inductive Magnetic Probe Diagnostics in a Plasma, MS Thesis, Naval Postgraduate School, 1970.
16. Lovberg, R. H., "Magnetic Probes," in Plasma Diagnostic Techniques, Huddleston, R. H. and Leonard, S. L., Eds., p. 75, Academic Press, 1965.
17. Boland, B. C. and others, "A Spectroscopic Study of the Plasma Generated by a Laser from Polyethylene," J. Phys. B. (Proc. Phys. Soc., Ser. 2), vol. 1, pp. 1180-1191, 1968.
18. Tanenbaum, B. S., Plasma Physics, p. 348, McGraw-Hill, 1967.
19. Keilhacker, M. and others, "Preionization for Collisionless Shock Wave Experiments by Means of Photoionization," Phys. Fluids, vol. 13, no. 9, pp. 2253-2261, September 1970.
20. Rumsby, P. T. and Beaulieu, J., "The Expansion of a Laser Produced Plasma," Proceedings of the Fifth European Conference on Controlled Fusion and Plasma Physics, Grenoble, France, p. 61, 21-25 August 1972.
21. Seka, W. and others, "Spectroscopic Measurements on Laser-Produced LiH Plasmas," J. Appl. Phys., vol. 41, no. 8, pp. 3440-3441, July 1970.

INITIAL DISTRIBUTION LIST

	No. Copies
1. Defense Documentation Center Cameron Station Alexandria, Virginia 22314	2
2. Library, Code 0212 Naval Postgraduate School Monterey, California 93940	2
3. Professor Fred Schwirzke, Code 61Sw Department of Physics and Chemistry Naval Postgraduate School Monterey, California 93940	10
4. Captain Leslie L. McKee, III, USAF AFWL/DYS Kirtland AFB, New Mexico 87117	1
5. Dr. John Stamper, Code 7727 Naval Research Laboratory Washington, D.C. 20390	1
6. Captain Roger S. Case, Jr., USAF AFWL/DYS Kirtland AFB, New Mexico 87117	1
7. Melvin Widner Sandia Lab P.O. Box 5800 Division 5231 Albuquerque, New Mexico 87115	1
8. Lt. Ronald S. Bird, USN Box 1301 Naval Postgraduate School Monterey, California 93940	1
9. Professor Alfred Copper, Code 61Cr Department of Physics and Chemistry Naval Postgraduate School Monterey, California 93940	1

DOCUMENT CONTROL DATA - R & D

(Security classification of title, body of abstract and indexing annotation must be entered when the overall report is classified)

ORIGINATING ACTIVITY (Corporate author)

Naval Postgraduate School
Monterey, California 93940

2a. REPORT SECURITY CLASSIFICATION

Unclassified

2b. GROUP

REPORT TITLE

An Investigation of the Self-Generated Magnetic Fields Associated with
Laser-Produced Plasma.

DESCRIPTIVE NOTES (Type of report and inclusive dates)

Doctor of Philosophy, December 1972

AUTHOR(S) (First name, middle initial, last name)

Leslie Lawrence McKee, III

REPORT DATE

December 1972

7a. TOTAL NO. OF PAGES

175

7b. NO. OF REFS

21

CONTRACT OR GRANT NO.

9a. ORIGINATOR'S REPORT NUMBER(S)

PROJECT NO.

9b. OTHER REPORT NO(S) (Any other numbers that may be assigned
this report)

DISTRIBUTION STATEMENT

Approved for public release; distribution unlimited.

SUPPLEMENTARY NOTES

12. SPONSORING MILITARY ACTIVITY

Naval Postgraduate School,
Monterey, California 93940

ABSTRACT

A plasma was produced by irradiating a 5 mil thick Mylar ($C_{10}H_8O_4$) foil with a 300 MW, 25 nsec Nd laser pulse. Magnetic fields were observed to spontaneously arise when the laser-produced plasma was formed.

The dependence of the self-generated magnetic fields on position, time, incident laser power, and ambient background pressure was investigated. The strength of the magnetic field, as well as its spatial and temporal dependences, was found to depend quite strongly on the background pressure of nitrogen. Most significantly, the strength of the field increased by a factor of six when the pressure of the nitrogen background was increased from 1 mTorr to 200 mTorr.

The results are analyzed by use of a theory in which the presence of a background gas influences the generating mechanism of the fields.

KEY WORDS	LINK A		LINK B		LINK C	
	ROLE	WT	ROLE	WT	ROLE	WT
Self-Generated Magnetic Fields						
Laser-Produced Plasma						
Magnetic Probe Signal						
Ambient Background Gas						
Photoionization						
Counterstreaming Plasmas						
Diffusion Time						
Computer Program						

Thesis

141387

M215 McKee

c.1

An investigation of
the self-generated
magnetic fields as-
sociated with a laser-
produced plasma.

10000000

22140

10000000

22140

10 AUG 75

23973

10000000

23235

Thesis

141387

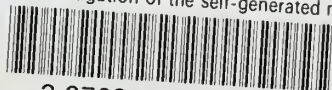
M215 McKee

c.1

An investigation of
the self-generated
magnetic fields as-
sociated with a laser-
produced plasma.

thesM215

An investigation of the self-generated m



3 2768 001 88208 7

DUDLEY KNOX LIBRARY